


Doctoral Dissertation
Doctoral Program in Electrical, Electronics and Communications Engineering
(33rd cycle)

Fast and Efficient Formulations for Electroencephalography-Based Neuroimaging Strategies

Maxime Y. Monin
* * * * * *

Supervisor
Francesco P. Andriulli

Doctoral Examination Committee:
Prof. Simon B. Adrian, University of Rostock (Referee)
Prof. Rajendra Mitharwal, Malaviya National Institute of Technology (Referee)
Prof. Roberto D. Graglia, Politecnico di Torino
Prof. Paola Pirinoli, Politecnico di Torino
Prof. Adrien Merlini, IMT Atlantique
Prof. Francesco P. Andriulli, Politecnico di Torino

Politecnico di Torino
May 24, 2021

Summary

The Boundary Element Method (BEM) is widely used as a key computational technique to infer knowledge about the human cerebral activity, and in particular, to solve the forward problem of electroencephalography. Despite the many advantages that explain the popularity of the BEM, several challenges impede its application. Notably, the composite head medium has an electrically inhomogeneous and anisotropic conductivity profile, which, in the absence of specific treatment, can only be coarsely approximated by the standard BEM. Furthermore, the time and memory costs for a standard, non-accelerated numerical method become prohibitively large for dense meshes, which hamper the use of the BEM in high-resolution imaging applications.

This thesis presents a new inhomogeneity and anisotropy-handling formulation which addresses the modeling deficiencies of the BEM in bioelectromagnetic brain modeling. This is achieved by complementing the classical surface integral equations of the BEM with volume and wire integral equations that leverage the specific structure of the different head tissues. Then, a new algebraic fast solver method based on the adaptive cross approximation algorithm is developed to improve the computational complexity of the formulation. This acceleration method introduces and leverages a spanning tree of the set of quadrature points, allowing the single compression of several block matrices together and improving the overall computational cost of the proposed formulation. Finally, we investigate the application of the proposed techniques to an inverse problem of conductivity estimation in the context of electrical impedance tomography. We show in particular that they enable a higher flexibility in the modeling of the problem unknowns while retaining the advantages of BEM formulations.

Acknowledgments

First and foremost, I would like to thank my PhD advisor Prof. Francesco Andriulli, without whom this thesis would have never happened. His guidance, insightful ideas and thorough advising at all times played a defining role in the completion of this scientific journey.

My thanks to past and present colleagues in the lab: Lyes, Alexandre, and Adrien, who helped me develop both theoretical knowledge and practical skills, and also John Erick, Andrea, Simon, Tiffany, Clément, as well as the newer lab members, Davide, Alessandro and Damiano. We shared great memories together and I hope I was as good a buddy as they were to me.

Finally, I would like to express again my gratitude to my long-time partner Tiffany, as well as my family and friends for their unconditional support over all these years.

Contents

List of Tables

List of Figures

Chapter 1

Introduction and Outline

The Boundary Element Method (BEM) is a powerful and popular computational technique used to solve a wide range of electromagnetic problems, including the modeling of the electric neural activity in the brain. Unfortunately, the imperfectly conducting and multi-layered head volume poses several challenges for classical BEM formulations, which curb their practical applicability. The work presented in this thesis aims at addressing these issues and proposes advances in the computational techniques that solve the biophysical head modeling problem to improve the BEM accuracy and computational complexity. The thesis is divided into several chapters, as follows.

Chapter 2 introduces the necessary background and notations used in the rest of the document. A brief overview of brain imaging is presented, followed by the role of the Maxwell's equations of electromagnetism in the biophysical modeling of brain functions. This leads to the forward problem of electroencephalography (EEG) for which standard analytical, semi-analytical and numerical electromagnetic solvers are described.

Chapter 3 presents an integral formulation to solve the inhomogeneous and anisotropic EEG forward problem. The general anisotropic Poisson's equation is described in the context of the multi-compartment head modeling. We then derive new coupling volume and wire integral equations adapted to the anisotropic skull and white matter conductivities, respectively. This is followed by the discretization of the hybrid integral equations to solve the system numerically. Finally, the wire conductivity model is validated with a homogenization procedure.

We develop in Chapter 4 a new fast solver to accelerate the computation and reduce the memory storage of integral equation methods. We first describe the concept of matrix compression via low-rank approximation. Then, we explain how the compression of the discrete system of equations can be achieved with a hierarchical octree decomposition and a block cluster tree partitioning of the matrix element interactions. Next, we derive a compression technique obtained by applying the adaptive cross approximation algorithm to the sampled kernel function

and factoring quadrature integrals into sparse matrices. Furthermore, we introduce a spanning tree decomposition of the quadrature points, which allows the factorization of several operators matrices with different kernels but evaluated on the same points into a unique compression scheme. This results in a convenient material-independent representation which is particularly suitable for hybrid integral equation formulations.

Chapter 5 presents an inverse solver for the problem of inhomogeneous tissue conductivity imaging. The forward and associated inverse problems of electrical impedance tomography are described. Then, we present an iterative solution to estimate the inhomogeneous head conductivity. We further explain how to accelerate the inverse procedure with the compression technique to obtain fast conductivity updates.

Finally, Chapter 6 concludes the manuscript and presents some avenues for future research.

Chapter 2

Background Theory

This chapter introduces some background on the research axes investigated in this thesis. We briefly outline the main technologies used for brain imaging, as well as the biophysical framework under which the brain activity is modeled and studied. In particular, we describe electroencephalography (EEG) and, starting from Maxwell's equations of electromagnetism, we derive the associated forward problem of EEG, which is used in a wide range of applications. We then recount several state-of-the-art methods employed to solve this forward problem, with a focus on the Boundary Element Method (BEM), a classical numerical technique that solves electromagnetic problems with integral equation formulations.

2.1 Introduction

2.1.1 Brain Imaging

The brain is one of the most fascinating biophysical structure studied in natural science. Responsible for the processing of the senses, emotions, and cognitive functions including memory, thinking and commands to the rest of the body, it is the central piece of the human organism. While the importance of the brain was recognized quite early in human history, neuroscience, the study of nervous systems, was mostly inferred from dissection experiments and remained quantitatively limited until the 20^{th} century. Then, technological and scientific progress in biology, electrophysiology [56] and computational science considerably expanded knowledge about the complex anatomy and physiology of the brain. The past half century has seen the development and maturation of new invasive and non-invasive technologies for the quantitative mapping of recorded brain-induced signals, further deepening our modern understanding of the still elusive brain structure and functions.

X-ray based Computed Tomography (CT) [25] and the advent of Magnetic Resonance Imaging (MRI) [71] have enabled high resolution imaging of the different head tissues (brain layers, skull, skin, fluids, etc.), so that the precise geometry

of individual (healthy or pathological) subjects can be recovered non-invasively at the millimeter scale. On the other hand, other technologies such as functional Magnetic Resonance Imaging (fMRI) [61], Positron Emission Tomography (PET) [6], Single Photon Emission Computed Tomography (SPECT) [126], Near-Infrared Spectroscopy (NIRS) [110], Electroencephalography (EEG) [86] and Magnetoencephalography (MEG) [55] have formed functional neuroimaging, a field that focuses on understanding the brain physiology via the recording of its activity [45]. While the techniques mentioned first are based on the detection of changes in blood flow (hemodynamics), and as such, are an indirect recording of the brain dynamics, EEG and MEG are directly sensitive to neuronal activity. In practice, hemodynamics-based methods have a high spatial resolution (a few millimeters) but low temporal resolution due to the fact that they are secondary measures of the brain metabolism [65]. This makes them limited for tracing brain dynamics that occur rapidly. These include both spontaneous oscillatory activity and evoked neural responses such as epileptic seizure or external stimuli [68, 23, 109]. In contrast, MEG and (especially non-invasive) EEG have lower spatial resolution than indirect methods but achieve a much higher temporal resolution (around the millisecond) which allows them to pick up even short transient signals [11, 8, 105] and enables low-latency, and possibly real-time brain reading, as seen notably in Brain Computer Interface (BCI) paradigms [129, 3].

2.1.2 EEG Brain Signals

At the microscopic level, the brain is principally composed of billions of glial cells and neurons (nerve cells). Neurons have a cell body called the soma, and fibrous extensions: the axon, through which electric signals are transmitted toward other neurons, and the dendrites, which pick up signals from the axons of other neurons at an interface called synapse [88]. The dynamics involved in this intricate assembly form a complex network in which electro-chemical signals are processed and transmitted. An active nerve cell synthesizes neurotransmitters, a chemical compound that locally perturbs the intracellular ionic concentration [24]. This creates an Excitatory Postsynaptic Potential (EPSP) or Inhibitory Postsynaptic Potential (IPSP) that depolarizes the membrane of the cell from its resting state and generates transmembrane currents between the intracellular and extracellular environments [86, 39]. In general, a postsynaptic potential on a single neuron will be drowned (averaged or canceled out) among the other signals from neighbor cells, and will not create a field strong enough to be picked up by EEG [24]. However, the spatial organization of pyramidal neurons in the grey matter is such that they are aligned parallel to each other and orthogonal to the brain surface, as illustrated in Figure 2.1. Therefore, on top of being relatively close to the scalp, synchronous signals in these neuron populations stack up additively instead of destructively, giving rise to a measurable electric field [96, 24].

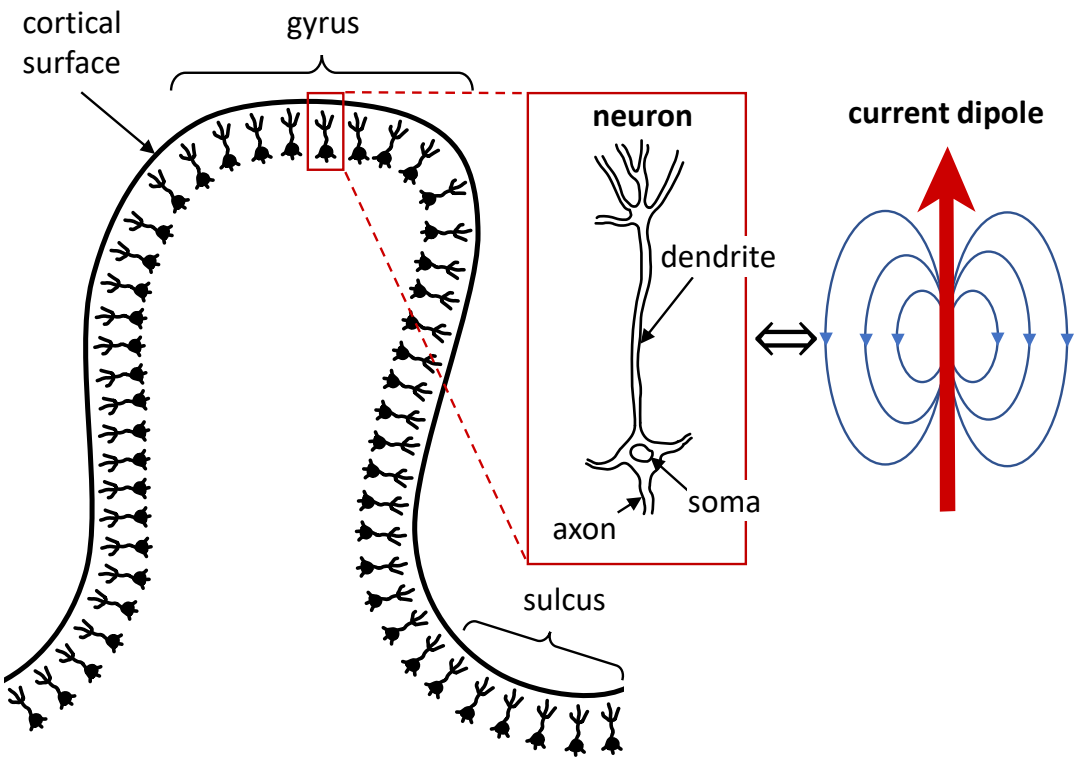

Figure 2.1: Cortical fold on the brain surface. The electric field generated by aligned neuron populations is similar to that from a dipole with a normal orientation to the cortex.

This electric field can be directly measured with electrodes that are either placed invasively inside the skull and close to the brain surface (Electrocorticography (ECoG) or intracranial Electroencephalography (iEEG)) or non-invasively on the scalp surface [63, 94]. While the former pick up high quality information of the nearby neuronal activity in the cortex (the surface of the brain, where the concentration of neurons is highest), they require a delicate surgical operation and cannot monitor the overall brain activity. In comparison, non-invasive EEG is much easier to set up, portable and affordable, which explains its wide adoption over the past few decades. However, due to the fact that the highly resistive skull produces a bio-shielding effect that blurs local field potentials together, scalp EEG suffers from a relatively low spatial resolution and requires considerable processing effort to detangle the recorded voltages into interpretable signals [88, 9].

The attempt at determining the underlying brain current origin from the observation of their trace as electric potential recordings constitutes the inverse source imaging problem of EEG [95, 7, 77]. This problem is fundamentally ill-posed since boundary voltage readings are far from sufficient information to uniquely constrain

its solution: there are infinitely many current source configurations in the brain volume that give rise to the same potential on the sampled scalp surface. Inverse source imaging is highly sensible to modeling errors and noise in the data, in the sense that small variations in the noisy measurements may lead to uncontrolled changes in the solution [51]. A plethora of regularization techniques has emerged in the past twenty years to stabilize this effect, but the validity of the prior constraints they enforce remains a challenge [88, 51]. A key component of most inverse algorithms is the solution of the associated EEG forward problem, in which the primary source is known and the electric potential is to be determined [53]. The EEG forward problem depends on the geometry of the head volume and on the conductivity of each tissue making up the overall inhomogeneous head medium. Since the solution of the inverse problem often requires multiple solutions of the forward problem, the assumptions made in forward modeling have a strong impact on the accuracy of brain source imaging [83, 52, 34].

Summarizing, the solution of the forward problem is an essential factor in our ability to get insight of the brain activity from EEG. On the main contributions of this thesis is dedicated to the improvement of forward solver methods. In the following, starting from Maxwell's equations, we describe standard analytical and numerical formulations used to solve the EEG forward problem.

2.2 Biophysical Model of Brain Signals

2.2.1 From Maxwell's equations to Poisson's equation

The EEG forward problem consists in the computation of the unknown electric potential from a known primary current source. These physical quantities obey the Maxwell's equations of electromagnetism [64]

$$\nabla \cdot \boldsymbol{D} = \rho \,, \tag{2.1}$$

$$\nabla \cdot \boldsymbol{B} = 0 \,, \tag{2.2}$$

$$\nabla \times \boldsymbol{E} = -\frac{\partial \boldsymbol{B}}{\partial t} \,, \tag{2.3}$$

$$\nabla \times \boldsymbol{H} = \boldsymbol{J} + \frac{\partial \boldsymbol{D}}{\partial t} \,, \tag{2.4}$$

where $\boldsymbol{D}$ is the electric flux density, $\boldsymbol{B}$ is the magnetic flux density, $\boldsymbol{E}$ is the electric field, $\boldsymbol{H}$ is the magnetic field, ρ is the electric charge density and $\boldsymbol{J}$ is the electric current density. For linear and non-dispersive media, the constitutive relations read

$$\boldsymbol{D} = \epsilon \boldsymbol{E} \,, \tag{2.5}$$

$$\boldsymbol{B} = \mu \boldsymbol{H} \,, \tag{2.6}$$

where ϵ and μ are the permittivity and permeability of the medium, respectively. The head tissues have approximately the same permeability μ_0 as the vacuum, so that μ can be considered constant and scalar. On the contrary, the permittivity ϵ varies significantly between the different head compartments, and is therefore a function of the position $\boldsymbol{r}$.

Charge and current densities are related by the continuity equation as

$$\nabla \cdot \boldsymbol{J} = -\frac{\partial \rho}{\partial t}\,. \tag{2.7}$$

From the neurophysiological considerations discussed in Section 2.1.2, the measured EEG signals mainly stem from space and time coherent active neuron populations, whose aggregation can be represented macroscopically as a current dipole oriented perpendicular to the cortex surface. This leads to a primary current density $\boldsymbol{J}_p$, expressed as

$$\boldsymbol{J}_p(\boldsymbol{r}) = \delta(\boldsymbol{r} - \boldsymbol{r}_0)\,\boldsymbol{q}\,, \tag{2.8}$$

where $\boldsymbol{r}_0$ and $\boldsymbol{q}$ are the dipole position and moment, respectively. Then, the total current density $\boldsymbol{J}$ satisfies Ohm's law

$$\boldsymbol{J} = \sigma \boldsymbol{E} + \frac{\partial \boldsymbol{P}}{\partial t} + \boldsymbol{J}_p\,, \tag{2.9}$$

where σ is the conductivity of the medium and $\boldsymbol{P} = (\epsilon - \epsilon_0)\boldsymbol{E}$ is the polarization density. Since measurable brain signals are low-frequency (the frequency spectrum decreases sharply in frequency according to a $1/f$ or $1/f^2$ power law [99]), for all practical purposes we can apply the quasi-static approximation of Maxwell's equations in which inductive and capacitive effects are considered negligible [106]. It then follows from (2.3) and (2.4) that

$$\nabla \times \boldsymbol{E} = \boldsymbol{0}\,, \tag{2.10}$$

$$\nabla \times \boldsymbol{H} = \boldsymbol{J}\,. \tag{2.11}$$

Since the curl of the gradient is null, we can define the scalar potential ϕ from the electric field as

$$\boldsymbol{E} = -\nabla \phi\,. \tag{2.12}$$

Replacing this expression in (2.9) then yields

$$\boldsymbol{J} = -\sigma \nabla \phi + \boldsymbol{J}_p\,. \tag{2.13}$$

Finally, using the fact that the divergence of the curl is also null, inserting (2.13) in (2.11) and applying the divergence operator gives Poisson's equation

$$\nabla \cdot (\sigma \nabla \phi) = \nabla \cdot \boldsymbol{J}_p\,. \tag{2.14}$$

The above equation relates the electric potential ϕ which can be measured on EEG electrodes and the primary brain source activity $\boldsymbol{J}_p$.

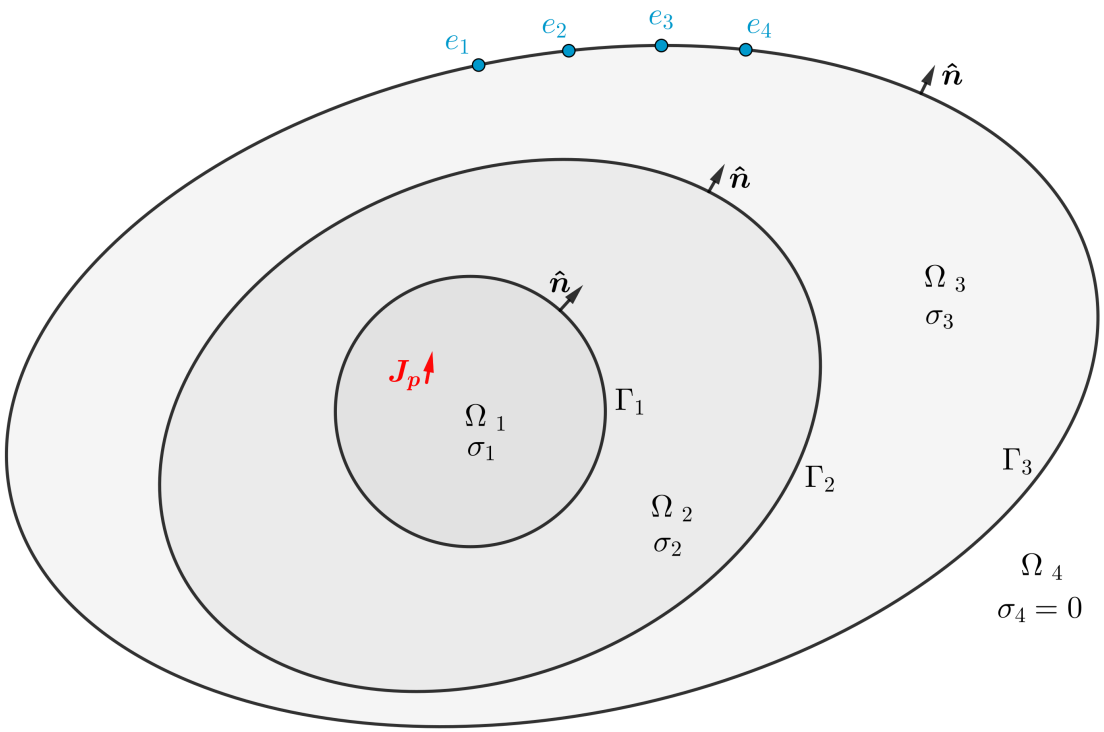

Figure 2.2: Standard three-layer nested head topology. The potential on surface electrodes (blue) results from the electric field generated by the impressed dipolar current source (red) in the brain compartment.

2.2.2 Boundary Conditions

In the following, the head domain is denoted Ω and is surrounded by the fully insulating air. To simplify the notation, it is assumed that there are N nested compartments Ω_i with conductivities σ_i such that

$$\Omega = \bigcup_{i=1}^{N} \Omega_i \,. \tag{2.15}$$

Such domains typically represent the brain, skull and scalp and the geometry is illustrated in Figure 2.2. The more general case with non-nested compartments is treated in Chapter 3. In this setting, (2.14) becomes a piecewise-homogeneous Poisson's equation

$$\sigma_i \Delta\phi(\boldsymbol{r}) = \nabla \cdot \boldsymbol{J}_p(\boldsymbol{r}) \,, \qquad \boldsymbol{r} \in \Omega_i \,. \tag{2.16}$$

This equation admits a unique solution when Neumann and/or Dirichlet boundary conditions are specified. Across any interface $\Gamma_i = \Omega_i \bigcap \Omega_{i+1}$ between tissues of different conductivities, the potential and the current density must be continuous,

i.e.

$$[\phi]_{\Gamma_i} = 0\,, \tag{2.17a}$$
$$[\hat{\boldsymbol{n}} \cdot \sigma \nabla \phi]_{\Gamma_i} = 0\,, \tag{2.17b}$$

where $\hat{\boldsymbol{n}}$ is the unit normal vector on Γ_i (oriented outward from Ω_i to Ω_{i+1}), $[f]_\Gamma = f|_\Gamma^- - f|_\Gamma^+$ denotes the jump of f across the surface, and $f|_\Gamma^+$ and $f|_\Gamma^-$ denote respectively the exterior and interior limits of a function f on surface Γ,

$$f(\boldsymbol{r})|_\Gamma^\pm = \lim_{\varepsilon \to 0} f(\boldsymbol{r} \pm \varepsilon \hat{\boldsymbol{n}})\,, \quad \boldsymbol{r} \in \Gamma\,. \tag{2.18}$$

In particular, since the air is insulating, no current flows outside of the head, so that on the head surface $\partial\Omega$ (in contact with the air), we have

$$\hat{\boldsymbol{n}} \cdot \sigma \nabla \phi|_{\Gamma_N}^- = 0\,. \tag{2.19}$$

Additionally, we also require that the potential satisfies the Sommerfeld radiation conditions

$$\lim_{\|\boldsymbol{r}\| \to \infty} \|\boldsymbol{r}\|\, |\phi(\boldsymbol{r})| < \infty\,, \tag{2.20a}$$
$$\lim_{\|\boldsymbol{r}\| \to \infty} \|\boldsymbol{r}\|\, \frac{\partial \phi(\boldsymbol{r})}{\partial \|\boldsymbol{r}\|} = 0\,, \tag{2.20b}$$

where $|\cdot|$ denotes the absolute value and $\|\cdot\|$ the Euclidian norm. These conditions are necessary to enforce the fact that only sources inside the head domain are considered.

2.2.3 Analytical Formulation

The first formulations used to solve the EEG forward problem were derived analytically and semi-analytically for spherical geometries. In the very coarse assumption that the shape of the head can be modeled with a single homogeneous sphere of radius a, a closed-form solution reads [133]

$$\phi(\boldsymbol{r}) = \frac{2}{\sigma_1} v_{dip}(\boldsymbol{r}) + \frac{\boldsymbol{q}}{4\pi\sigma_1 a^2 \|\boldsymbol{r} - \boldsymbol{r}_0\|} \cdot \left(\boldsymbol{r} + \frac{r_0 \cos\gamma\, \boldsymbol{r} - a\boldsymbol{r}_0}{a + \|\boldsymbol{r} - \boldsymbol{r}_0\| - r_0 \cos\gamma} \right)\,, \tag{2.21}$$

where v_{dip} is the potential of the dipole located at $\boldsymbol{r}_0$ with moment $\boldsymbol{q}$ in an infinite domain of unitary conductivity (and will be explicitly defined later), r_0 is the norm of $\boldsymbol{r}_0$, and γ is the angle between $\boldsymbol{r}$ and $\boldsymbol{r}_0$.

While this formula is relatively simple, it does not take into account the high conductivity contrast between the different head tissues. An improvement then consists in modeling the head as a nested geometry of N concentric spheres, each one

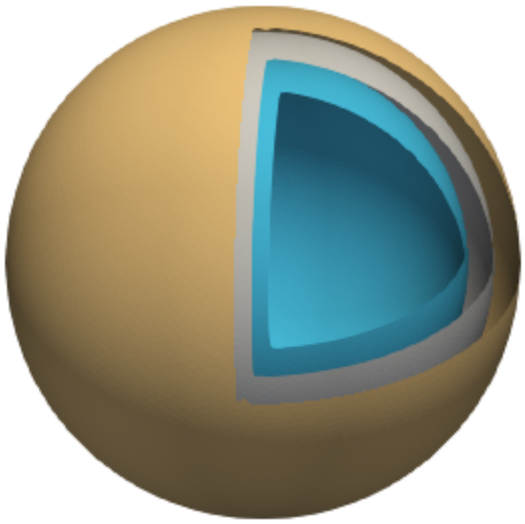

Figure 2.3: An approximation of the head with concentric spheres. The volume inside each sphere has a different homogeneous conductivity.

delimiting two head tissues with different conductivities, as illustrated in Figure 2.3. In this case, the potential can be expressed as the infinite series [16, 135]

$$\phi(\boldsymbol{r}) = \frac{q}{4\pi\sigma_N r^2} \sum_{n=1}^{\infty} \frac{2n+1}{n} \left(\frac{r_0}{r}\right)^{n-1} f_n \left(n \cos\alpha P_n(\cos\gamma) + \cos\beta \sin\alpha P_n^1(\cos\gamma)\right) , \tag{2.22}$$

where P_n and P_n^1 are the Legendre and associated Legendre polynomials, respectively, α is the angle between $\boldsymbol{q}$ and $\boldsymbol{r}_0$, and β is the angle between two planes: one that contains $\boldsymbol{r}$ and $\boldsymbol{r}_0$ and the other defined by $\boldsymbol{q}$ and $\boldsymbol{r}_0$. Finally, f_n is given by

$$f_n = \frac{n}{n m_{22} + (1+n)\, m_{21}} , \tag{2.23}$$

and the coefficients m_{ij} are given by the recursive formula

$$\begin{bmatrix} m_{11} & m_{12} \\ m_{21} & m_{22} \end{bmatrix} = \frac{1}{(2N+1)^{N-1}} \times \prod_{k=1}^{N-1} \begin{bmatrix} n + (n+1)\dfrac{\sigma_k}{\sigma_{k+1}} & (n+1)\left(\dfrac{\sigma_k}{\sigma_{k+1}} - 1\right)\left(\dfrac{r}{a_k}\right)^{2n+1} \\ n\left(\dfrac{\sigma_k}{\sigma_{k+1}} - 1\right)\left(\dfrac{a_k}{r}\right)^{2n+1} & n + 1 + n\dfrac{\sigma_k}{\sigma_{k+1}} \end{bmatrix} \tag{2.24}$$

Note that the above product of matrices is non-commuting and must be applied from highest to lowest indices (left to right). By truncating the series, the error in the solution ϕ is controlled and depends on the eccentricity of the dipole source.

Extensions of these formulas also provide a semi-analytical solution for spherical anisotropy, i.e. each layer k is described by a constant radial conductivity σ_k^r and a tangential conductivity σ_k^t [135].

Although these formulations provide a relatively fast way to compute the electrode potential, their geometrical restrictions lead to unavoidable modeling errors since in real-case scenarios, no head compartment has a smooth spherical shape. Nonetheless, they provide a robust reference for validating the accuracy of numerical formulations in canonical test cases.

2.2.4 Integral Equation Formulations

A more flexible framework to solve the EEG forward problem in the case of non-canonical geometries is provided by numerical methods [18, 64]. In short, a numerical method divides the geometry under consideration into small mesh elements and allows one to approximate the physical solution of the continuous world by solving a discrete system built from integral or differential equations and applied to the small elements. To handle physical problems with an arbitrary geometry, for which no closed-form solution is available, one can solve a discrete system of equations in matrix form

$$\mathbf{A}\boldsymbol{x} = \boldsymbol{b}\,, \tag{2.25}$$

where $\mathbf{A}$ is an invertible matrix and the size of the unknown vector $\boldsymbol{x}$ grows as the mesh element size decreases. There are several families of numerical techniques employed in literature, the main ones being the Finite Difference Method (FDM), the Finite Element Method (FEM) and the Boundary Element Method (BEM) [53]. The FDM discretizes a cartesian grid of the head volume and approximates the partial derivatives of the quantities involved in the Maxwell's differential equations with their finite differences between neighbor nodes. The FEM is also based on a full volume discretization of the head, but with arbitrary volume elements (hexahedral or tetrahedral) which makes it more suitable than the FDM for respecting the geometry and curvature of the domain boundaries. Conceptually, the FEM is also based on differential equations, but represents the unknown potential with a set of sufficiently smooth basis functions (the finite elements), each defined on a few volume elements.

By contrast, the BEM [18] is based on an integral equation reformulation of the Maxwell's equations, and importantly, by leveraging the Green's identities, requires the discretization of only the surface boundaries between the different head tissues. Examples of surface and volume discretizations are illustrated in Figure 2.4. Asymptotically, the number of unknowns in a BEM system increases quadratically when the mesh is refined while it grows cubically for volumetric methods. Therefore, at a given mesh size, the BEM systems to solve are typically much smaller than the FEM and FDM systems. Additionally, depending on the formulation, increasing

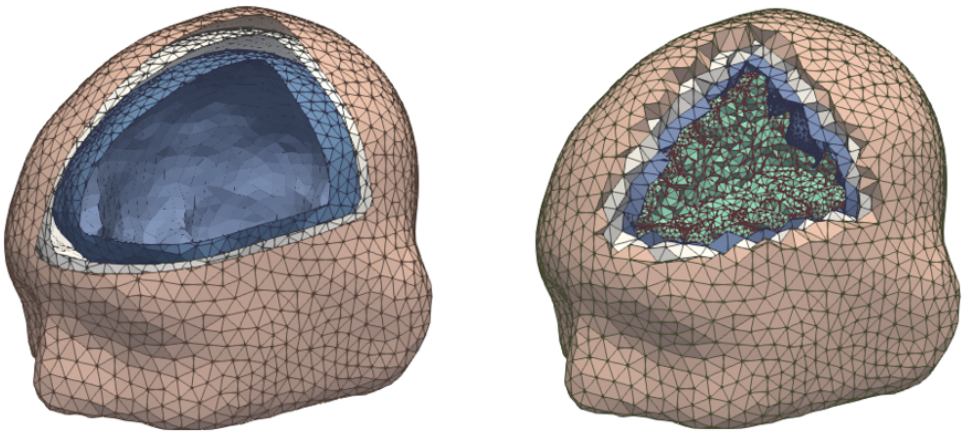

Figure 2.4: Surface (left) and volume (right) discretizations of the head geometry.

the mesh refinement may deteriorate the condition number of the system matrix that is to be inverted, which is defined as the ratio between its largest and smallest singular values. A high condition number is undesirable as it is linked to a lower convergence rate for iterative solvers [28]. Furthermore, the BEM does not suffer from singularity issues related to having the dipolar source excitation lie within a mesh element as in the case of volume methods. The main drawback of the BEM is that standard formulations cannot handle anisotropic and inhomogeneous tissues like the skull bones and the brain white matter [131]. These modeling deficiencies of the BEM can lead to important errors. Additionally, in the absence of fast solver acceleration techniques [29], the computational advantage of the BEM is somewhat offset by the non-local nature of the operators involved, which results in dense matrix systems compared to the large but sparse FEM or FDM matrices. Proposing a cure for such drawbacks is the focus of the research presented in this thesis.

Boundary Integral Operators

The fundamental solution of Poisson's equation which satisfies the radiation conditions (2.20a) and (2.20b) is the static Green's function

$$G(\boldsymbol{r}, \boldsymbol{r}') = \frac{1}{4\pi \|\boldsymbol{r} - \boldsymbol{r}'\|}\,, \tag{2.26}$$

which verifies

$$\Delta G(\boldsymbol{r}, \boldsymbol{r}') = -\delta(\boldsymbol{r} - \boldsymbol{r}')\,. \tag{2.27}$$

We can then define the single-layer and double-layer potentials on any smooth surface Γ, which map a scalar function f defined on Γ to a scalar function defined

on $\mathbb{R}^3 \setminus \Gamma$ [84, 31],

$$(\mathcal{S}f)(\boldsymbol{r}) = \int_\Gamma G(\boldsymbol{r}, \boldsymbol{r}') f(\boldsymbol{r}') \, \mathrm{d}S' \,, \tag{2.28}$$

$$(\mathcal{D}f)(\boldsymbol{r}) = \int_\Gamma \partial_{n'} G(\boldsymbol{r}, \boldsymbol{r}') f(\boldsymbol{r}') \, \mathrm{d}S' \,, \tag{2.29}$$

where $\partial_{n'} = \hat{\boldsymbol{n}}' \cdot \nabla'$. The single and double-layer potentials can be extended to Γ although they have different continuity properties [31]:

- The single-layer potential $\mathcal{S}$ is only weakly singular when $\boldsymbol{r} \to \boldsymbol{r}'$ and is continuous across Γ, that is

$$\mathcal{S}f|_\Gamma^+ = \mathcal{S}f|_\Gamma^- \,. \tag{2.30}$$

- The double-layer potential $\mathcal{D}$ is discontinuous across Γ and reads

$$\mathcal{D}f|_\Gamma^\pm = \pm\frac{1}{2} f(\boldsymbol{r}) + \int_\Gamma \partial_{n'} G(\boldsymbol{r}, \boldsymbol{r}') f(\boldsymbol{r}') \, \mathrm{d}S' \,, \tag{2.31}$$

  where the last term is the Cauchy principal value of the improper integral.

Given an arbitrary smooth vector field $\hat{\boldsymbol{n}}(\boldsymbol{r})$ in $\mathbb{R}^3$ that matches the normal on the surface when $\boldsymbol{r} \in \Gamma$, we now consider the normal derivatives of the previous potentials, giving rise to the adjoint double-layer potential $\mathcal{D}^*$ and the hypersingular potential $\mathcal{N}$, respectively:

$$(\mathcal{D}^* f)(\boldsymbol{r}) = \int_\Gamma \partial_n G(\boldsymbol{r}, \boldsymbol{r}') f(\boldsymbol{r}') \, \mathrm{d}S' \,, \tag{2.32}$$

$$(\mathcal{N}f)(\boldsymbol{r}) = \int_\Gamma \partial_n (\partial_{n'} G(\boldsymbol{r}, \boldsymbol{r}')) f(\boldsymbol{r}') \, \mathrm{d}S' \,. \tag{2.33}$$

Both potentials also have different continuity properties when crossing the surface [84]:

- The normal derivative of $\mathcal{S}$ is discontinuous across Γ and reads

$$\mathcal{D}^* f|_\Gamma^\pm = \mp\frac{1}{2} f(\boldsymbol{r}) + \int_\Gamma \partial_n G(\boldsymbol{r}, \boldsymbol{r}') f(\boldsymbol{r}') \, \mathrm{d}S' \,, \tag{2.34}$$

  where the last term is the Cauchy principal value of the improper integral.

- The normal derivative of $\mathcal{D}$ exists as an improper integral and remains continuous across Γ so that

$$\mathcal{N}f|_\Gamma^+ = \mathcal{N}f|_\Gamma^- \,. \tag{2.35}$$

In the following developments regarding boundary element formulations, we consider the single-layer, double-layer, adjoint double-layer and hypersingular operators, which also act on a scalar function f defined on Γ but map to another function defined on Γ. With a slight abuse of notation, they are also denoted $\mathcal{S}$, $\mathcal{D}$, $\mathcal{D}^*$ and $\mathcal{N}$, respectively, and are well-defined as improper integrals [84].

The derivatives of G read

$$\nabla' G(\boldsymbol{r}, \boldsymbol{r}') = -\nabla G(\boldsymbol{r}, \boldsymbol{r}') = \frac{\boldsymbol{r} - \boldsymbol{r}'}{4\pi \|\boldsymbol{r} - \boldsymbol{r}'\|^3}\,, \tag{2.36}$$

and

$$\hat{\boldsymbol{n}} \cdot \nabla(\hat{\boldsymbol{n}}' \cdot \nabla' G(\boldsymbol{r}, \boldsymbol{r}')) = \frac{\hat{\boldsymbol{n}} \cdot \hat{\boldsymbol{n}}'}{4\pi \|\boldsymbol{r} - \boldsymbol{r}'\|^5} - 3\,\frac{\hat{\boldsymbol{n}} \cdot (\boldsymbol{r} - \boldsymbol{r}')\,\hat{\boldsymbol{n}}' \cdot (\boldsymbol{r} - \boldsymbol{r}')}{4\pi \|\boldsymbol{r} - \boldsymbol{r}'\|^3}\,. \tag{2.37}$$

We note in particular that the solution of Poisson's equation in an infinite medium with normalized conductivity ($\sigma = 1$) is obtained by convolving G and the divergence of $\boldsymbol{J}_p$ (or more generally, the right-hand side of Poisson's equation) as

$$\begin{aligned} v_{dip}(\boldsymbol{r}) &= -G * (\nabla \cdot \boldsymbol{J}_p) \\ &= -\int G(\boldsymbol{r}, \boldsymbol{r}') \nabla' \cdot \boldsymbol{J}_p(\boldsymbol{r}')\, \mathrm{d}S' \\ &= \frac{\boldsymbol{q} \cdot (\boldsymbol{r} - \boldsymbol{r}_0)}{4\pi \|\boldsymbol{r} - \boldsymbol{r}_0\|^3}\,. \end{aligned} \tag{2.38}$$

The previously defined potentials appear in specific applications of the Green's identities. From the divergence theorem,

$$\int_V \nabla \cdot \boldsymbol{f}(\boldsymbol{r})\, \mathrm{d}V = \int_{\partial V} \boldsymbol{f}(\boldsymbol{r}) \cdot \hat{\boldsymbol{n}}\, \mathrm{d}S\,, \tag{2.39}$$

where V is a compact volume bounded by the closed surface ∂V. For two smooth scalar functions u and v, applying (2.39) to $u\nabla v$ and $v\nabla u$ and subtracting the two equations, we obtain the Green's identity

$$\int_V u\Delta v - v\Delta u\, \mathrm{d}V = \int_{\partial V} u\partial_n v - v\partial_n u\, \mathrm{d}S\,. \tag{2.40}$$

Setting $v = G$ and $u = \phi$, we obtain in each compartment, for $\boldsymbol{r} \in \Omega_i \backslash \partial\Omega_i$,

$$\begin{aligned} & \int_{\Omega_i} \phi\Delta G - G\Delta\phi\, \mathrm{d}V = \int_{\partial\Omega_i} \phi\partial_n G - G\partial_n\phi\, \mathrm{d}S \\ \Leftrightarrow \quad & -\phi - \frac{1}{\sigma_i}\int_{\Omega_i} G\sigma_i\Delta\phi\, \mathrm{d}V = \mathcal{D}\phi|_{\partial\Omega_i} - \mathcal{S}\partial_n\phi|^-_{\partial\Omega_i} \\ \Leftrightarrow \quad & \phi = \frac{1}{\sigma_i}\mathcal{S}\nabla\cdot\boldsymbol{J}_p|_{\Omega_i} - \mathcal{D}\phi|_{\partial\Omega_i} + \mathcal{S}\partial_n\phi|^-_{\partial\Omega_i}\,. \end{aligned} \tag{2.41}$$

Finally, making $\boldsymbol{r}$ tend toward $\partial\Omega_i$ and given the continuity properties of the $\mathcal{D}$ and $\mathcal{S}$ operators, we obtain the integral equation

$$\frac{1}{2}\phi = \frac{1}{\sigma_i} v_{\Omega_i} - \mathcal{D}\phi|_{\partial\Omega_i} + \mathcal{S}\partial_n\phi|^-_{\partial\Omega_i}\,, \qquad \boldsymbol{r} \in \partial\Omega_i\,, \tag{2.42}$$

where v_{Ω_i} is defined as

$$v_{\Omega_i}(\boldsymbol{r}) = \begin{cases} v_{dip}(\boldsymbol{r}) & \text{if } \boldsymbol{r}_0 \in \Omega_i \\ 0 & \text{otherwise}\,. \end{cases} \tag{2.43}$$

The inner limit superscript $^-$ has been removed from $\mathcal{D}\phi|_{\partial\Omega_i}$ in (2.42) since ϕ is continuous according to (2.17a) and the discontinuity of the double-layer potential is included in the left-hand side term. The last equations (2.41) and (2.42) are quite meaningful. Indeed, they show how the unknown potential ϕ can be expressed in terms of a homogeneous domain solution v_{Ω_i} which has a simple closed-form expression, and two auxiliary surface contributions: the potential and its normal derivative on the conductivity discontinuity interfaces. Thus, the determination of the surface quantities is sufficient to obtain the solution of the forward problem anywhere in the head volume Ω. Therefore, when solving the problem numerically with the BEM, only the 2D boundaries of the geometry need to be discretized, thereby reducing the dimensionality of the unknown domain by one compared to 3D volume methods.

Double-Layer Formulation

The first standard BEM formulation is obtained by removing one of the two surface unknowns ($\partial_n\phi$) and deriving a surface integral equation which involves only ϕ. This is done by leveraging the current continuity boundary condition (2.17b). Consider the interface Γ_i separating the volumes Ω_i and Ω_{i+1}, i.e. $\Gamma_i = \partial\Omega_i^- = \partial\Omega_{i+1}^+$. Applying (2.42) to each compartment and multiplying by the local conductivity yields for $\boldsymbol{r} \in \Gamma_i$,

$$\begin{aligned} \frac{\sigma_i}{2}\phi = v_{\Omega_i} &- \sigma_i\mathcal{D}\phi|_{\Gamma_i} + \sigma_i\mathcal{S}\partial_n\phi|^-_{\Gamma_i} \\ &- \sigma_i\mathcal{D}\phi|_{\partial\Omega_i\setminus\Gamma_i} + \sigma_i\mathcal{S}\partial_n\phi|^-_{\partial\Omega_i\setminus\Gamma_i}\,, \end{aligned} \tag{2.44}$$

$$\begin{aligned} \frac{\sigma_{i+1}}{2}\phi = v_{\Omega_{i+1}} &+ \sigma_{i+1}\mathcal{D}\phi|_{\Gamma_i} - \sigma_{i+1}\mathcal{S}\partial_n\phi|^+_{\Gamma_i} \\ &- \sigma_{i+1}\mathcal{D}\phi|_{\partial\Omega_{i+1}\setminus\Gamma_i} + \sigma_{i+1}\mathcal{S}\partial_n\phi|^-_{\partial\Omega_{i+1}\setminus\Gamma_i}\,, \end{aligned} \tag{2.45}$$

and for the other domains, when $j \notin \{i, i+1\}$,

$$0 = v_{\Omega_j} - \sigma_j\mathcal{D}\phi|_{\partial\Omega_j} + \sigma_j\mathcal{S}\partial_n\phi|^-_{\partial\Omega_j}\,. \tag{2.46}$$

Summing all equations, the $\mathcal{S}\partial_n\phi$ contributions all disappear according to (2.17b) since

$$\sigma_i \mathcal{S}\partial_n\phi|_{\Gamma_i}^- - \sigma_{i+1}\mathcal{S}\partial_n\phi|_{\Gamma_i}^+ = \mathcal{S}[\sigma\partial_n\phi]_{\Gamma_i} = 0\,, \tag{2.47}$$

and we finally obtain the double-layer surface integral equation

$$\frac{\sigma_i + \sigma_{i+1}}{2}\,\phi(\boldsymbol{r}) - \sum_{j=1}^{N}(\sigma_{j+1} - \sigma_j)\mathcal{D}\phi|_{\Gamma_j}(\boldsymbol{r}) = v_{dip}(\boldsymbol{r})\,, \qquad \boldsymbol{r} \in \Gamma_i\,. \tag{2.48}$$

Adjoint Double-Layer Formulation

Another BEM formulation can be obtained by retaining the other surface contribution in (2.42). For this purpose, going back to (2.41) and differentiating it with respect to $\boldsymbol{r}$ along $\hat{\boldsymbol{n}}$, we get an equation involving the other two operators

$$\partial_n\phi = \frac{1}{\sigma_i}\partial_n v_{\Omega_i} - \mathcal{N}\phi|_{\partial\Omega_i} + \mathcal{D}^*\partial_n\phi|_{\partial\Omega_i}\,, \qquad \boldsymbol{r} \in \Omega_i\,. \tag{2.49}$$

Taking the limit $\boldsymbol{r} \to \partial\Omega_i$ then reads

$$\frac{1}{2}\partial_n\phi|_{\partial\Omega_i}^- = \frac{1}{\sigma_i}\partial_n v_{\Omega_i} - \mathcal{N}\phi|_{\partial\Omega_i} + \mathcal{D}^*\partial_n\phi|_{\partial\Omega_i}^-\,, \qquad \boldsymbol{r} \in \partial\Omega_i\,. \tag{2.50}$$

Applying (2.50) to the neighbor compartments on either side of Γ_i, we get

$$\begin{aligned}\frac{1}{2}\partial_n\phi|_{\Gamma_i}^- &= \frac{1}{\sigma_i}\partial_n v_{\Omega_i} - \mathcal{N}\phi|_{\Gamma_i} + \mathcal{D}^*\partial_n\phi|_{\Gamma_i}^- \\ &\quad - \mathcal{N}\phi|_{\partial\Omega_i\setminus\Gamma_i} + \mathcal{D}^*\partial_n\phi|_{\partial\Omega_i\setminus\Gamma_i}^-\,, \end{aligned}\tag{2.51}$$

$$\begin{aligned}\frac{1}{2}\partial_n\phi|_{\Gamma_i}^+ &= \frac{1}{\sigma_{i+1}}\partial_n v_{\Omega_{i+1}} + \mathcal{N}\phi|_{\Gamma_i} - \mathcal{D}^*\partial_n\phi|_{\Gamma_i}^+ \\ &\quad - \mathcal{N}\phi|_{\partial\Omega_{i+1}\setminus\Gamma_i} + \mathcal{D}^*\partial_n\phi|_{\partial\Omega_{i+1}\setminus\Gamma_i}^-\,, \end{aligned}\tag{2.52}$$

and on the remaining compartments, for $j \notin \{i, i+1\}$,

$$0 = \frac{1}{\sigma_j}\partial_n v_{\Omega_j} - \mathcal{N}\phi|_{\partial\Omega_j} + \mathcal{D}^*\partial_n\phi|_{\partial\Omega_j}^-\,. \tag{2.53}$$

This time, summing over all compartments, the continuous $\mathcal{N}\phi$ contributions cancel by approaching from each side and we obtain

$$\frac{1}{2}(\partial_n\phi|_{\Gamma_i}^- + \partial_n\phi|_{\Gamma_i}^+) - \sum_{j=1}^{N}\mathcal{D}^*(\partial_n\phi|_{\Gamma_j}^- - \partial_n\phi|_{\Gamma_j}^+) = \sum_{j=1}^{N}\frac{1}{\sigma_j}\partial_n v_{\Omega_j}\,. \tag{2.54}$$

Introducing the auxiliary surface unknown

$$\xi_i = [\partial_n\phi]_{\Gamma_i} = \partial_n\phi|_{\Gamma_i}^- - \partial_n\phi|_{\Gamma_i}^+\,, \tag{2.55}$$

we can express the left side of (2.54) in terms of ξ_i by enforcing the boundary condition (2.17b),

$$\begin{aligned} & \sigma_i \partial_n \phi|_{\Gamma_i}^- = \sigma_{i+1} \partial_n \phi|_{\Gamma_i}^+ \\ \Leftrightarrow \quad & \partial_n \phi|_{\Gamma_i}^- + \partial_n \phi|_{\Gamma_i}^+ = \frac{\sigma_{i+1} + \sigma_i}{\sigma_{i+1} - \sigma_i} \xi_i \,. \end{aligned} \tag{2.56}$$

Inserting (2.56) into (2.54) leads to the adjoint double layer surface integral equation

$$\frac{\sigma_{i+1} + \sigma_i}{2} \xi_i - (\sigma_{i+1} - \sigma_i) \sum_{j=1}^{N} \mathcal{D}^* \xi_i = \sum_{j=1}^{N} \frac{1}{\sigma_j} \partial_n v_{\Omega_j} \,. \tag{2.57}$$

Compared to the double-layer formulation, one more step is needed to get the potential. We use (2.42) in each compartment and sum over all of them to get ϕ from ξ_i as

$$\phi = \sum_{i=1}^{N} \frac{1}{\sigma_i} v_{\Omega_i} + \sum_{i=1}^{N} \mathcal{S} \xi_i \,. \tag{2.58}$$

Symmetric Formulation

In contrast to the two previous formulations, the symmetric formulation [66] includes two types of surface contributions. Dividing (2.44) and (2.45) by the local conductivity and subtracting one from the other, we get

$$\begin{aligned} 2\mathcal{D}\phi|_{\Gamma_i} - \mathcal{S}(\partial_n \phi|_{\Gamma_i}^- + \partial_n \phi|_{\Gamma_i}^+) - \mathcal{D}\phi|_{\Gamma_{i+1}} - \mathcal{D}\phi|_{\Gamma_{i-1}} + \mathcal{S}\partial_n \phi|_{\Gamma_{i+1}}^- + \mathcal{S}\partial_n \phi|_{\Gamma_{i-1}}^+ \\ = \frac{1}{\sigma_i} v_{\Omega_i} - \frac{1}{\sigma_{i+1}} v_{\Omega_{i+1}} \,. \end{aligned} \tag{2.59}$$

In the above equation, we used the fact that in the present nested geometry, $\partial\Omega_i = \Gamma_{i-1} \bigcup \Gamma_i$ (assuming that $\Gamma_0 = \Gamma_{N+1} = \emptyset$). Importantly, we did not add contributions from other domains. We can now introduce yet another auxiliary surface unknown

$$p_i = \sigma_i \partial_n \phi|_{\Gamma_i}^- \,. \tag{2.60}$$

From (2.17b), p_i also satisfies

$$p_i = \sigma_{i+1} \partial_n \phi|_{\Gamma_i}^+ \,, \tag{2.61}$$

so that (2.59) can be rewritten

$$\begin{aligned} 2\mathcal{D}\phi|_{\Gamma_i} - \left(\frac{1}{\sigma_{i+1}} + \frac{1}{\sigma_i} \right) \mathcal{S} p_i - \mathcal{D}\phi|_{\Gamma_{i+1}} - \mathcal{D}\phi|_{\Gamma_{i-1}} + \frac{1}{\sigma_{i+1}} \mathcal{S} p_{i+1} + \frac{1}{\sigma_i} \mathcal{S} p_{i-1} \\ = \frac{1}{\sigma_i} v_{\Omega_i} - \frac{1}{\sigma_{i+1}} v_{\Omega_{i+1}} \,. \end{aligned} \tag{2.62}$$

Since we have two surface unknowns $\phi|_{\Gamma_i}$ and p_i, a second equation is needed to make the system solvable. In a dual fashion to the previous derivation, we multiply (2.51) and (2.52) by the local conductivity and subtract one from the other to get

$$(\sigma_i + \sigma_{i+1})\mathcal{N}\phi|_{\Gamma_i} - \sigma_i\mathcal{D}^*\partial_n\phi|^-_{\Gamma_i} - \sigma_{i+1}\mathcal{D}^*\partial_n\phi|^+_{\Gamma_i} - \sigma_{i+1}\mathcal{N}\phi|_{\Gamma_{i+1}} - \sigma_i\mathcal{N}\phi|_{\Gamma_{i-1}} + \sigma_{i+1}\mathcal{D}^*\partial_n\phi|^-_{\Gamma_{i+1}} + \sigma_{i-1}\mathcal{D}^*\partial_n\phi|^-_{\Gamma_{i-1}} = \partial_n v_{\Omega_i} - \partial_n v_{\Omega_{i+1}}\,, \quad (2.63)$$

or, equivalently in terms of p_i,

$$(\sigma_i + \sigma_{i+1})\mathcal{N}\phi|_{\Gamma_i} - 2\mathcal{D}^*p_i - \sigma_{i+1}\mathcal{N}\phi|_{\Gamma_{i+1}} - \sigma_i\mathcal{N}\phi|_{\Gamma_{i-1}} + \mathcal{D}^*p_{i+1} + \mathcal{D}^*p_{i-1} = \partial_n v_{\Omega_i} - \partial_n v_{\Omega_{i+1}}\,. \quad (2.64)$$

The combination of (2.62) and (2.64) provides a symmetric system of equations for the unknowns $\phi|_{\Gamma_i}$ and p_i. While there are more unknowns than the other two formulations, it must be noted that in the symmetric formulation, they interact only when they share a common compartment, so that the resulting system is block diagonal.

2.2.5 Discretization

Discretization is the process through which the BEM (or any other numerical method) moves from the continuous world to an approximate discrete one, making the physical problem solvable with matrix equations of finite dimensions [64, 115]. In the BEM, the boundary surfaces separating the piecewise-homogeneous domains are tessellated into a set of vertices and triangles. This process is illustrated in Figure 2.5 for a spherical geometry at different mesh sizes. For realistic, patient-specific geometries, this is typically obtained from anatomical images (e.g. structural MRI) of the subject. Grayscale volumetric data delineate different tissue compartments, whose boundaries can then be extracted and used in BEM modeling [40].

A set of mesh-specific basis functions is then defined. For scalar-valued unknowns, the classical basis functions are the piecewise constant functions, defined on the i^{th} triangle t_i of the mesh as

$$\psi_i(\boldsymbol{r}) = \begin{cases} 1 & \text{if } \boldsymbol{r} \in t_i \\ 0 & \text{otherwise,} \end{cases} \quad (2.65)$$

and the piecewise linear functions, which are indexed by the vertices of the mesh instead of the cells, and are equal to 1 on their defining vertex v_i and decrease linearly to 0 on the other vertices of the triangles that contain v_i. After choosing a suitable set of basis functions f_i, the unknowns of each formulation, i.e.

- $\phi|_{\Gamma_i}$ in the double-layer formulation,

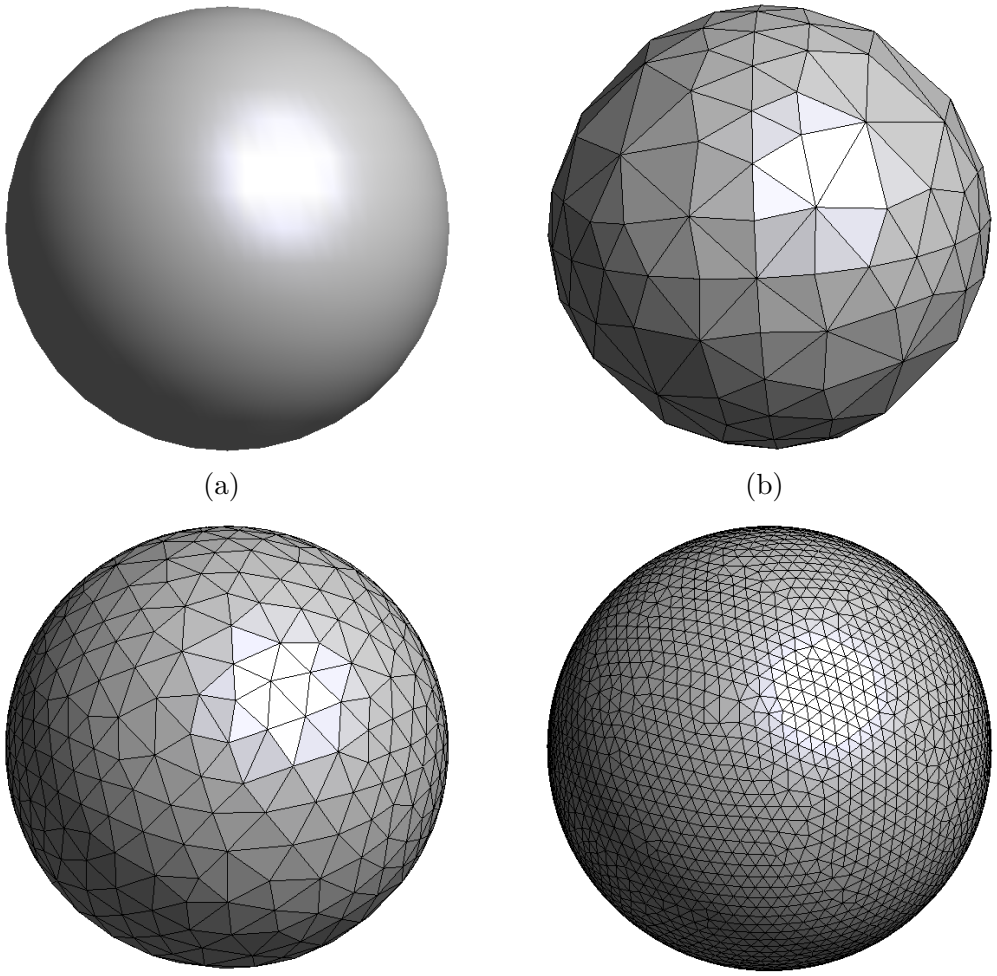

Figure 2.5: A sphere of unit radius and its discretization into triangle meshes with different edge lengths. With increasing mesh refinement, the mesh elements are more regular and the geometry is more faithfully approximated.

- ξ_i in the adjoint double-layer formulation, or
- $\phi|_{\Gamma_i}$ and p_i in the symmetric formulation,

are approximated by a linear combination of the basis functions, e.g.

$$\phi|_{\Gamma}(\boldsymbol{r}) \approx \sum_{k=1}^{N_f} x_k f_k(\boldsymbol{r})\,, \tag{2.66}$$

where $x_k \in \mathbb{R}$ are the basis function coefficients. By doing this, the unknown is no longer the continuous function ϕ but a vector $\boldsymbol{x} \in \mathbb{R}^{N_f}$ of finite size, N_f being

equal to the number of triangles for a piecewise constant expansion or the number of vertices for a piecewise linear expansion.

A set of as many (N_f) independent equations is then needed to make the system square and solvable, i.e. in the form (2.25). The dependency in the variable $\boldsymbol{r}$ is removed by testing the integral equations with a set of N_f weighting or testing functions, i.e. by performing a second integration on the support of each testing function. These functions must be carefully chosen according to the mapping properties of the discretized operators [115, 101]. Although not necessarily conforming, a commonly adopted strategy is to choose them to be the same as the source basis function, which, in the double-layer formulation, leads to the discrete system

$$\begin{bmatrix} (\mathbf{G}-\mathbf{D})_{11} & (\mathbf{G}-\mathbf{D})_{12} & \dots & (\mathbf{G}-\mathbf{D})_{1N_f} \\ (\mathbf{G}-\mathbf{D})_{21} & (\mathbf{G}-\mathbf{D})_{22} & \dots & (\mathbf{G}-\mathbf{D})_{2N_f} \\ \vdots & \vdots & \ddots & \vdots \\ (\mathbf{G}-\mathbf{D})_{N_f1} & (\mathbf{G}-\mathbf{D})_{N_f2} & \dots & (\mathbf{G}-\mathbf{D})_{N_fN_f} \end{bmatrix} \begin{bmatrix} x_1 \\ x_2 \\ \vdots \\ x_{N_f} \end{bmatrix} = \begin{bmatrix} b_1 \\ b_2 \\ \vdots \\ b_{N_f} \end{bmatrix}, \tag{2.67}$$

where, for the i^{th} basis function belonging to the interface that separates the outer volume denoted i^+ and the inner volume i^-, the matrices and vectors are defined as

$$(\mathbf{G})_{ij} = \frac{\sigma_{i^+} + \sigma_{i^-}}{2} \langle f_i, f_j \rangle_\Gamma = \frac{\sigma_{i^+} + \sigma_{i^-}}{2} \int_\Gamma f_i(\boldsymbol{r}) f_j(\boldsymbol{r}) \, \mathrm{d}S \,, \tag{2.68}$$

$$(\mathbf{D})_{ij} = (\sigma_{j^+} - \sigma_{j^-}) \langle f_i, \mathcal{D} f_j \rangle_\Gamma = (\sigma_{j^+} - \sigma_{j^-}) \int_\Gamma f_i(\boldsymbol{r}) \int_\Gamma \partial_{n'} G(\boldsymbol{r}, \boldsymbol{r'}) f_j(\boldsymbol{r'}) \, \mathrm{d}S' \, \mathrm{d}S \,, \tag{2.69}$$

$$(\boldsymbol{b})_i = \langle f_i, v_{dip} \rangle_\Gamma = \int_\Gamma f_i(\boldsymbol{r}) v_{dip}(\boldsymbol{r}) \, \mathrm{d}S \,. \tag{2.70}$$

We note in particular that the Gram operator matrix $\mathbf{G}$ is sparse: for each testing function f_i there are only a few source basis functions f_j (those in the neighborhood of f_i) which share a non-empty intersecting support. Therefore, while it is of size $N_f \times N_f$, $\mathbf{G}$ contains only $\mathcal{O}(N_f)$ non-zero entries. This is to be contrasted with the operator matrix $\mathbf{D}$, whose entries are in general not null because of the non-local kernel G (or rather its normal derivative in this case). One may note in particular the singularity of the entries for self terms, i.e. when the testing and source integral supports intersect. Weak or strong singularities are typically handled with singularity extraction [49, 62] or singularity cancellation [38, 122] methods, which make the kernel integrable via analytical reformulations and/or coordinate transforms. After filling the operator matrices, the system can be solved for example by direct inversion as

$$\boldsymbol{x} = \mathbf{A}^{-1} \boldsymbol{b} \,. \tag{2.71}$$

The solution of the EEG forward problem is then given either directly from the coefficients of $\boldsymbol{x}$ if ϕ is a discretized unknown or in one additional step by (2.58) for the adjoint double-layer formulation.

The procedure described in this section highlights the trade-off between accuracy and computational/memory cost. Refining the mesh leads to a more faithful geometry, and variations of the solution are better represented with an increased resolution, but this comes at the cost of having to build, store and solve a bigger matrix system. Furthermore, conductivity variations are only allowed between different compartments. This condition poses severe limitations in the ability of the BEM to model inhomogeneous compartments with local conductivity variations and/or anisotropy. In the next chapter, we present a new formulation that extends the applicability of the BEM to such scenarios.

Chapter 3

A Hybrid Solution to the EEG Forward Problem

Solving the electroencephalography (EEG) forward problem is a fundamental step in a wide range of applications including biomedical imaging techniques based on inverse source localization. State-of-the-art electromagnetic solvers resort to a computationally expensive volumetric discretization of the full head to account for its complex and heterogeneous electric profile. The more efficient, popular in biomedical imaging circles, but unfortunately oversimplifying Boundary Element Method (BEM) relies instead on a piecewise-uniform approximation that severely curbs its application in high resolution EEG. This contribution lifts the standard BEM constraints by treating the local anisotropies with adequate fiber and thin volume integral equations that are tailored to the specific structures of the fibrous white matter and the inhomogeneous skull. The proposed hybrid integral equation formulation thereby avoids the full volumetric discretization of the head medium and allows for a realistic and efficient BEM-like solution of the anisotropic EEG forward problem. The accuracy and flexibility of the proposed formulation is demonstrated through numerical experiments involving both canonical and realistic Magnetic Resonance Imaging (MRI)-based head models.

3.1 Introduction

EEG is one of the most popular technique for recording human brain signals. Its high temporal resolution means that the intricate brain activity can be observed on scalp electrodes at the millisecond scale. Such traces are of high scientific interest since they offer the unparalleled possibility to infer brain functions in real time. A central challenge for EEG brain imaging is then to characterize the relationship between brain sources and the electric potential measured by the surface electrodes [83]. Such mapping constitutes the forward problem of EEG and it has been an

important field of research for the past few decades.

The EEG forward problem poses several challenges which complicate the practical implementation of a solution that is both accurate and computationally efficient. Indeed, the human head has a complex morphology. It is composed of several biological tissues through which electric currents propagate non-uniformly due to their different conductivities. In particular, the high conductivity contrast between the skull and the surrounding cerebrospinal fluid on one side, and skin on the other side creates a shielding effect which ultimately degrades the quality of non-invasive EEG since the strong spatial mixing of brain signals blurs the electrode readings [88]. Another challenge is that the conductivity values of the different tissues are not well-defined in literature, and instead vary depending on the subjects and experimental conditions (temperature, recording frequency, methodology, pathology, in vivo compared to ex vivo, etc.) [76].

Furthermore, each tissue is not completely homogeneous and their microscopic structure can result in macroscopic inhomogeneity and/or anisotropy. This means that the conductivity of a single tissue may not be well approximated by a constant scalar value. This is notably the case for the skull: it is made of several hard (highly resistive) and soft (less resistive) bone layers which result in different effective radial and tangential conductivities [130]. Another strongly inhomogeneous and anisotropic head tissue is the brain white matter. The brain volume is principally made of axon bundles with a fiber-like structure, along which the conductivity is higher than in transversal directions [36]. Overall, the inter- and intra-tissue conductivity variations make the EEG forward problem inhomogeneous and anisotropic at its millimeter resolution scale.

In realistic applications, the forward problem is solved using numerical techniques [53] derived from differential or integral formulations of Maxwell's equations [21, 82, 70, 54, 66]. State-of-the-art differential methods such as the Finite Element Method (FEM) can easily incorporate the local variations of tissue conductivity, but rely on a computationally expensive volumetric discretization of the entire head. The BEM [86, 20] is a popular alternative which reformulates the forward problem with surface integrals on the boundaries of the head compartments, meaning that the linear systems to solve are considerably smaller. The BEM is numerically stable and can be further augmented using acceleration techniques such as the Fast Multipole Method (FMM) to reach great computational efficiency [72, 59]. Unfortunately, the standard BEM requires the head medium to be piecewise-uniform, and is consequently unable to model the anisotropies and inhomogeneities of the skull and of the white matter. Therefore, this intrinsic assumption drastically reduces its applicability.

A BEM formulation that accounts for the skull anisotropy was recently proposed in [100] but relies on a volumetric discretization of the whole head. On the other hand, the white matter fibers can be quantitatively reconstructed from

tractography algorithms applied on diffusion MRI (dMRI) data [132, 125]. This representation is promising in that it describes white matter in a much more effective and precise way than via a complete volume discretization, which is independent of the fiber structure. The thin fiber geometry is a common structure in high frequency electromagnetic problems [127] and has been studied in a few contributions for bioelectromagnetic problems [89, 98, 75, 102]. Tractography has also been used in transcranial brain stimulation studies [87, 92], although the fiber structure was neglected in the forward model construction.

In summary, no contribution has been proposed to solve the anisotropic forward problem without resorting to a full volumetric discretization of the head. In this chapter, we address this issue by modifying and complementing the standard BEM 2D equations with adequate anisotropy-handling fiber 1D equations for the white matter and volume 3D equations for the skull. The resulting new hybrid integral formulation is effectively tailored to the EEG forward problem as every head tissue is suitably discretized according to its electrical properties. The integration of tractography algorithms for white matter conductivity profiling is obtained with an electrically coherent derivation of the fiber parameters, enabling the computation of a multimodal and MRI consistent solution of the anisotropic EEG forward problem. The validity of the proposed scheme is confirmed by numerical experiments which demonstrate its practical relevance. Preliminary results described in this chapter were presented in [79], [80] and the main work was published in [81].

3.2 Anisotropic EEG Forward Problem

3.2.1 Problem Statement

The multi-layered head medium Ω is the aggregation of several compact and bounded domains,

$$\Omega = \bigcup_{i=1}^{N} \Omega_i \,, \tag{3.1}$$

which are not necessarily nested. Each one represents a different tissue type with an approximately homogeneous conductivity $\sigma_i \in \mathbb{R}$ such that

$$\overline{\overline{\sigma}}(\boldsymbol{r} \in \Omega_i) = \sigma_i \mathbf{I} \,, \tag{3.2}$$

where $\mathbf{I}$ is the identity matrix, and $\overline{\overline{\cdot}}$ denotes a tensorial quantity. Each compartment Ω_i has a closed surface boundary $\partial\Omega_i$ which is the union of the (not necessarily continuous) interfaces between Ω_i and the neighbor domains

$$\partial\Omega_i = \left(\bigcup_{k=1}^{i-1} \Gamma_{ki} \right) \cup \left(\bigcup_{k=i+1}^{N+1} \Gamma_{ik} \right) \,, \tag{3.3}$$

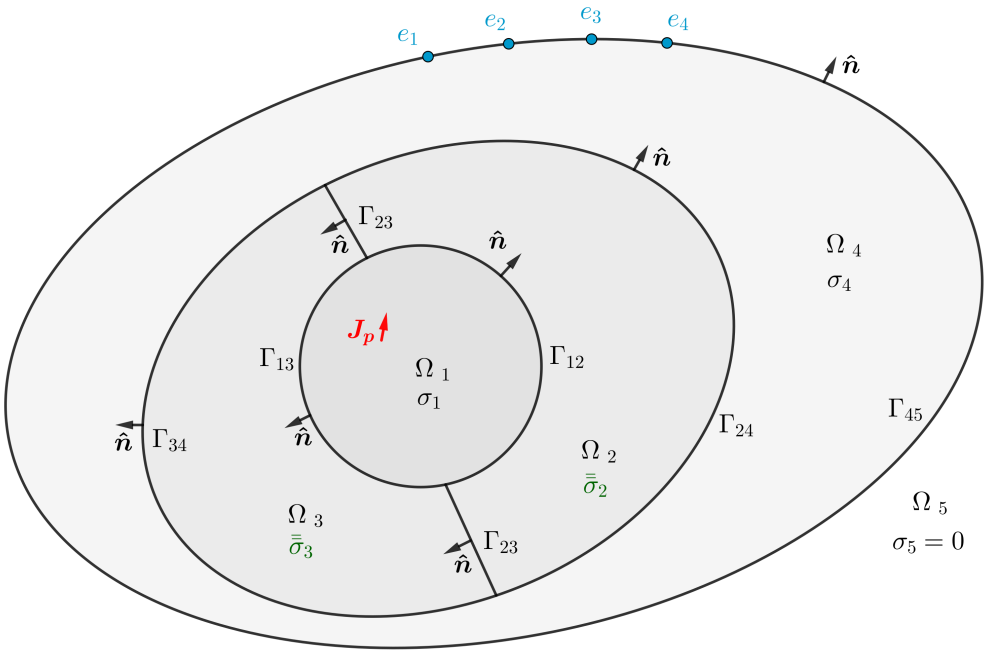

Figure 3.1: Non-nested head topology. Note that compartments Ω_2 and Ω_3 have inhomogeneous and anisotropic conductivities, highlighted in green.

where the interfaces Γ_{kl} $(1 \leq k < l \leq N+1)$ are arbitrarily oriented from the smaller to the higher indexed region. The local normal $\hat{\boldsymbol{n}}$ on Γ_{kl} points from Ω_k to Ω_l. In particular, if Ω_k and Ω_l are not neighbors, then $\Gamma_{kl} = \varnothing$. The head volume is surrounded by the non-conducting air domain Ω_{N+1} such that $\sigma_{N+1} = 0$.

Although neglected in standard BEM, we allow inhomogeneity and anisotropy within any head region. This is explicitly modeled using the conductivity contrast

$$\bar{\bar{\chi}}_i(\boldsymbol{r}) = (\sigma_i \mathbf{I} - \bar{\bar{\sigma}}(\boldsymbol{r}))\, \bar{\bar{\sigma}}^{-1}(\boldsymbol{r})\,, \quad \boldsymbol{r} \in \Omega_i\,. \tag{3.4}$$

With this piecewise definition, we see that the contrast measures how much the actual local conductivity differs from the background (i.e. the homogeneous domain it belongs to), and in particular, it is null in uniform regions such as Ω_{N+1}. It is often assumed in literature that the head has a nested geometry: for instance, in a typical 3-layer setting, the brain region is inside the skull region which itself is inside the scalp region. This is not actually true, e.g. the skull contains holes which connects the inner and outer compartments. However, this simplification makes the notation easier, but is technically not required for the validity of BEM formulations, as demonstrated in the following. Such a non-nested geometry is illustrated in Figure 3.1.

The observable brain activity is very low-frequency (typically below 100 Hz with EEG), which justifies the use of the quasi-static approximation of Maxwell's

equations. In this regime, the electric field is the gradient of an electric potential,

$$\boldsymbol{E}(\boldsymbol{r}) = -\nabla\phi(\boldsymbol{r})\,, \tag{3.5}$$

which obeys the Poisson's equation

$$\nabla\cdot(\overline{\overline{\sigma}}(\boldsymbol{r})\nabla\phi(\boldsymbol{r})) = \nabla\cdot\boldsymbol{J}_p(\boldsymbol{r})\,, \quad \boldsymbol{r}\in\Omega\,, \tag{3.6}$$

where $\boldsymbol{J}_p$ is a primary current originating from the brain. This equation is complemented by the Neumann and Dirichlet boundary conditions

$$\phi(\boldsymbol{r})|^{-}_{\Gamma_{ij}} = \phi(\boldsymbol{r})|^{+}_{\Gamma_{ij}}\,, \tag{3.7a}$$

$$\hat{\boldsymbol{n}}(\boldsymbol{r})\cdot\overline{\overline{\sigma}}(\boldsymbol{r})\nabla\phi(\boldsymbol{r})|^{-}_{\Gamma_{ij}} = \hat{\boldsymbol{n}}(\boldsymbol{r})\cdot\overline{\overline{\sigma}}(\boldsymbol{r})\nabla\phi(\boldsymbol{r})|^{+}_{\Gamma_{ij}}\,, \tag{3.7b}$$

as well as the radiation conditions (2.20a) and (2.20b) introduced in the previous chapter. The physical interpretation of the boundary conditions is that they enforce the continuity of the electric potential and its normal derivative in the medium across the interfaces of conductivity discontinuity.

3.2.2 Anisotropy Characterization of the Head Tissues

The forward problem can be solved with surface integral equations only, but on the condition that the conductivity tensor $\overline{\overline{\sigma}}$ is well-approximated with a constant (homogeneity) scalar (isotropy) value for each domain, which was introduced earlier as the background conductivity σ_i. In all generality, the conductivity is expressed as a symmetric positive semi-definite spatial tensor

$$\overline{\overline{\sigma}}(\boldsymbol{r}) = U(\boldsymbol{r})\begin{bmatrix}\sigma_{v_1}(\boldsymbol{r}) & 0 & 0\\ 0 & \sigma_{v_2}(\boldsymbol{r}) & 0\\ 0 & 0 & \sigma_{v_3}(\boldsymbol{r})\end{bmatrix}U^T(\boldsymbol{r})\,, \tag{3.8}$$

where the unitary matrix U contains the eigenvectors along which the conductivity corresponds to the associated eigenvalues σ_{v_k}. In the isotropic case, all three eigenvalues are equal and the tensor reduces to a scalar value. Instead, the skull anisotropy appears as a series (resp. parallel) combination of resistances in the radial (resp. tangential) direction due to its layered structure. We define in the skull compartment the thickness fraction of soft bone t_s, and given the hard and soft bone conductivities σ_{hard} and σ_{soft} [2], the skull conductivity is modeled as [130, 34]

$$\sigma_{v_1}(\boldsymbol{r}) = \frac{1}{\dfrac{t_s(\boldsymbol{r})}{\sigma_{soft}} + \dfrac{1-t_s(\boldsymbol{r})}{\sigma_{hard}}}\,, \tag{3.9}$$

$$\sigma_{v_2}(\boldsymbol{r}) = \sigma_{v_3}(\boldsymbol{r}) = t_s(\boldsymbol{r})\,\sigma_{soft} + (1-t_s(\boldsymbol{r}))\,\sigma_{hard}\,, \tag{3.10}$$

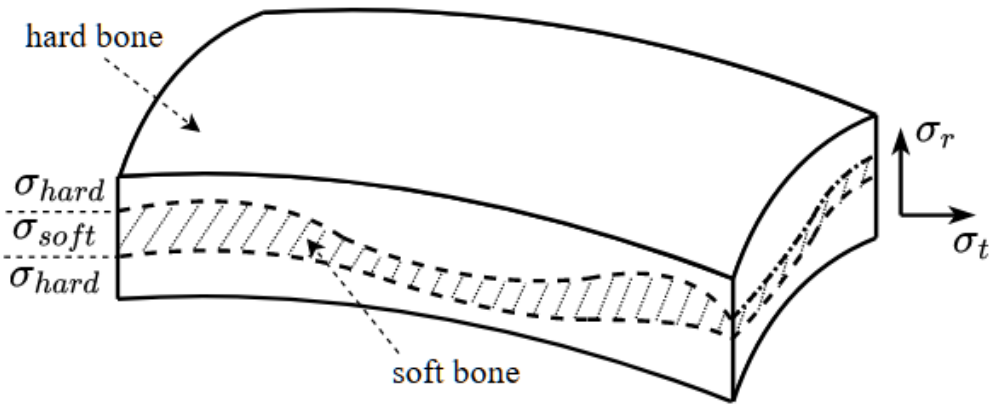

Figure 3.2: Inhomogeneous and anisotropic conductivity in the skull. The presence of soft bone perturbs the effective conductivity in radial and tangential directions.

which is illustrated in Figure 3.2.

The other main anisotropic tissue is the white matter in the brain volume. Let us denote $i_w \in [1, N]$ the index of the domain that contains the white matter. The inner brain is principally composed of axon bundles [134, 125]. Their prolate ellipsoidal geometry results in a dense macroscopic network structure of coherently oriented fibers that transmit information between different brain regions. This implies that in the white matter, the displacement of water molecules (measurable with dMRI [69]) and ions is much stronger along the fibers than across them, as illustrated in Figure 3.3. As a consequence, and similar to [131], the conductivity at position $\boldsymbol{r} \in \Omega_{i_w}$ within a fiber with orientation $\hat{\boldsymbol{l}}$ is described by the rotational symmetric tensor

$$\overline{\overline{\sigma}}(\boldsymbol{r}) = \sigma_{i_w}\mathbf{I} + (\sigma_l - \sigma_{i_w})\,\hat{\boldsymbol{l}}\hat{\boldsymbol{l}}^T\,, \tag{3.11}$$

where the longitudinal conductivity σ_l is approximately ten times higher than the background conductivity σ_{i_w} [85, 73].

3.3 General Anisotropy-Handling Formulation

The standard BEM formulations presented in Section 2.2.4 cannot be applied directly unless the presence of anisotropy is neglected. Instead, we rewrite (3.6) in

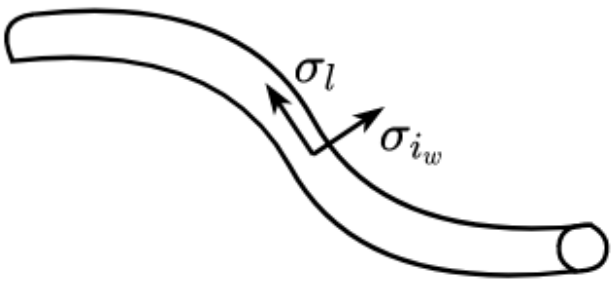

Figure 3.3: Inhomogeneous and anisotropic white matter conductivity model. The conductivity is higher along the axonal direction.

any region Ω_i as

$$\begin{aligned}
& \nabla \cdot (\overline{\overline{\sigma}} \nabla \phi) = \nabla \cdot \boldsymbol{J}_p \\
\Leftrightarrow \quad & \nabla \cdot ((\overline{\overline{\sigma}} + \sigma_i \mathbf{I} - \sigma_i \mathbf{I}) \nabla \phi) = \nabla \cdot \boldsymbol{J}_p \\
\Leftrightarrow \quad & \nabla \cdot (\sigma_i \nabla \phi) = \nabla \cdot (\boldsymbol{J}_p + (\sigma_i \mathbf{I} - \overline{\overline{\sigma}}) \nabla \phi) \\
\Leftrightarrow \quad & \sigma_i \Delta \phi = \nabla \cdot (\boldsymbol{J}_p + \overline{\overline{\chi}}_i \overline{\overline{\sigma}} \nabla \phi) \\
\Leftrightarrow \quad & \sigma_i \Delta \phi = \nabla \cdot (\boldsymbol{J}_p + \boldsymbol{J}_{eq_i}) \,,
\end{aligned} \tag{3.12}$$

where $\boldsymbol{J}_{eq_i} = \overline{\overline{\chi}}_i \overline{\overline{\sigma}} \nabla \phi$ denotes an equivalent return current in the inhomogeneous domain. This last expression explicitly shows that the general anisotropic Poisson's equation can be recast as a piecewise-homogeneous problem, i.e. a problem in which every region has a constant scalar conductivity σ_i, with an additional equivalent current on the source term (right side), as illustrated in Figure 3.4. Therefore, we can now apply a BEM approach to solve the Poisson problem.

3.3.1 Surface Integral Equation

To reformulate the Poisson problem with integral equations, we recall the static Green's function

$$G(\boldsymbol{r}, \boldsymbol{r}') = \frac{1}{4\pi \|\boldsymbol{r} - \boldsymbol{r}'\|} \,. \tag{3.13}$$

This particular function satisfies

$$\Delta G(\boldsymbol{r}, \boldsymbol{r}') = -\delta(\boldsymbol{r}, \boldsymbol{r}') \,, \tag{3.14}$$

and is the fundamental solution to the Poisson problem that vanishes at infinity (when $R = \|\boldsymbol{r} - \boldsymbol{r}'\| \to \infty$). For any $\boldsymbol{r} \in \Omega_k$, the second Green's identity applied

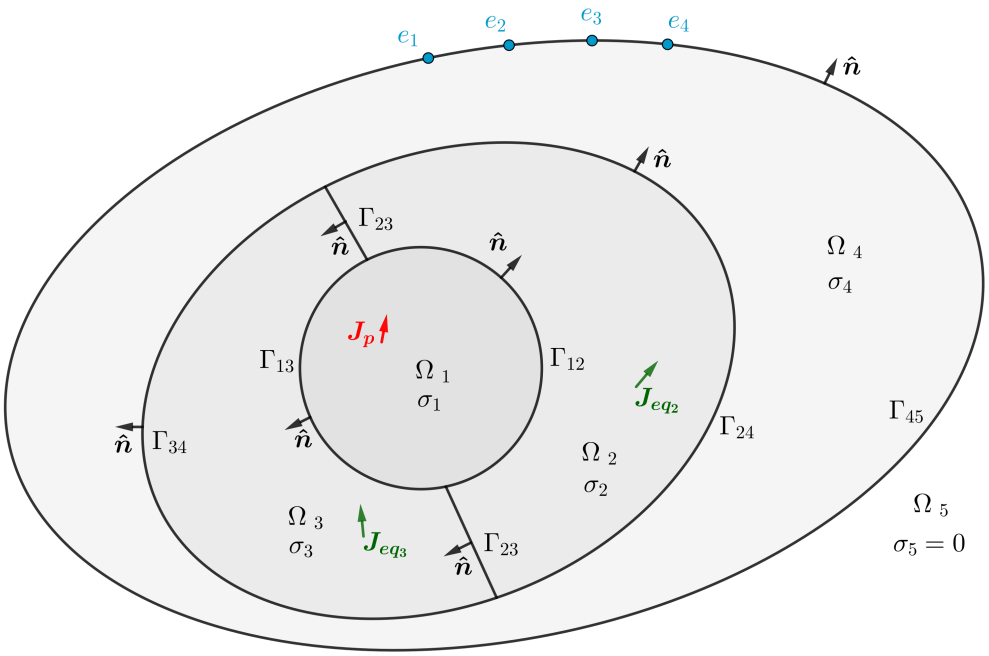

Figure 3.4: Equivalent piecewise homogeneous and isotropic head model with anisotropy-handling equivalent currents.

to G and ϕ in any closed domain Ω_j gives

$$\begin{aligned}
&\int_{\Omega_j} G\Delta\phi - \phi\Delta G \,\mathrm{d}V' = \int_{\partial\Omega_j} G\partial_{n'}\phi - \phi\partial_{n'}G \,\mathrm{d}S' \\
\Leftrightarrow \quad &\frac{1}{\sigma_j}\int_{\Omega_j} G\nabla'\cdot(\boldsymbol{J}_p + \boldsymbol{J}_{eq_j})\,\mathrm{d}V' + \delta_{j,k}\phi = \int_{\partial\Omega_j} G\partial_{n'_o}\phi \,\mathrm{d}S' - \int_{\partial\Omega_j}\partial_{n'_o}G\phi \,\mathrm{d}S' \\
\Leftrightarrow \quad &\delta_{j,k}\phi + \frac{1}{\sigma_j}\mathcal{S}_v(\boldsymbol{J}_p|_{\Omega_j} + \boldsymbol{J}_{eq_j}) = \mathcal{S}\partial_{n'_o}\phi|^-_{\partial\Omega_j} - \mathcal{D}\phi|_{\partial\Omega_j}\,. \qquad (3.15)
\end{aligned}$$

where the single-layer and double-layer operators $\mathcal{S}$ and $\mathcal{D}$ have been defined in (2.28) and (2.29), the normal $\hat{\boldsymbol{n}}'_o$ on $\boldsymbol{r}' \in \partial\Omega_j$ points outward (out of Ω_j) and $\delta_{j,k}$ denotes the Kronecker delta, defined as

$$\delta_{j,k} = \begin{cases} 1 & \text{if } j = k \\ 0 & \text{otherwise}\,. \end{cases} \qquad (3.16)$$

Given (3.3), the right side can be written more explicitly with $\hat{\boldsymbol{n}}' = \hat{\boldsymbol{n}}(\boldsymbol{r}')$ as

$$\mathcal{S}\partial_{n'_o}\phi|^-_{\partial\Omega_j} = -\sum_{i=1}^{j-1}\mathcal{S}\partial_{n'}\phi|^+_{\Gamma_{ij}} + \sum_{i=j+1}^{N+1}\mathcal{S}\partial_{n'}\phi|^-_{\Gamma_{ji}}\,, \qquad (3.17)$$

$$\mathcal{D}\phi|_{\partial\Omega_j} = -\sum_{i=1}^{j-1}\mathcal{D}\phi|_{\Gamma_{ij}} + \sum_{i=j+1}^{N+1}\mathcal{D}\phi|_{\Gamma_{ji}}\,. \qquad (3.18)$$

Furthermore, (3.15) can also be applied in the case $j = N + 1$ by considering a dummy spherical surface enclosing Ω_{N+1} with a radius that tends to infinity. Assuming that ϕ vanishes at infinity, which is a necessary condition for the uniqueness of the solution, all terms are equal to zero on this virtual surface and the right side of the resulting equation involves only the external boundary (i.e. the head surface $\bigcup_{k=1}^{N} \Gamma_{kN+1}$). When making the inner limit $\boldsymbol{r} \to \Gamma_{kl}$ on the boundary $\partial\Omega_k$, with Ω_l being a neighbor of Ω_k such that $k < l$, the discontinuity of the double-layer operator $\mathcal{D}$ gives rise to the expression

$$\lim_{\boldsymbol{r}\to\Gamma_{kl}} \mathcal{D}\phi|_{\Gamma_{kl}^{\pm}} = \pm\frac{1}{2}\phi(\boldsymbol{r}) + \int_{\Gamma_{kl}} \partial_{n'} G(\boldsymbol{r},\boldsymbol{r}')\phi(\boldsymbol{r}')\,\mathrm{d}S' \,. \tag{3.19}$$

Applying the inner limit to (3.15), we thus obtain

$$\delta_{j,k}\frac{\phi}{2} + \delta_{j,l}\frac{\phi}{2} + \mathcal{D}\phi|_{\partial\Omega_j} - \mathcal{S}\partial_{n'_o}\phi|^{-}_{\partial\Omega_j} + \frac{1}{\sigma_j}\mathcal{S}_v\boldsymbol{J}_{eq_j} = -\frac{1}{\sigma_j}\mathcal{S}_v\boldsymbol{J}_p|_{\Omega_j} \,, \tag{3.20}$$

where the operator $\mathcal{S}_v$ is the analogue of $\mathcal{S}$ that maps a vectorial function $\boldsymbol{f}$ in the volume to a scalar surface function as

$$(\mathcal{S}_v\boldsymbol{f})(\boldsymbol{r}) = \int_{\Omega} G(\boldsymbol{r},\boldsymbol{r}')\nabla'\cdot\boldsymbol{f}(\boldsymbol{r}')\,\mathrm{d}V' \,. \tag{3.21}$$

The next step is to differentiate (3.20) with respect to $\boldsymbol{r}$ along $\hat{\boldsymbol{n}}$. We thus get the operator $\mathcal{D}^*$, which is defined for surface functions as

$$(\mathcal{D}^* f)(\boldsymbol{r}) = \int_{\Gamma} \partial_n G(\boldsymbol{r},\boldsymbol{r}') f(\boldsymbol{r}')\,\mathrm{d}S' \,. \tag{3.22}$$

Analogously, we also introduce the volume double-layer operator $\mathcal{D}_v^*$ which is the equivalent of $\mathcal{D}^*$ that maps vectorial functions in the volume to a surface function

$$(\mathcal{D}_v^*\boldsymbol{f})(\boldsymbol{r}) = \int_{\Omega} \partial_n G(\boldsymbol{r},\boldsymbol{r}')\nabla'\cdot\boldsymbol{f}(\boldsymbol{r}')\,\mathrm{d}V' \,. \tag{3.23}$$

Both $\mathcal{D}^*$ and $\mathcal{D}_v^*$ have the following discontinuities

$$\lim_{\boldsymbol{r}\to\Gamma_{kl}^{\pm}} \mathcal{D}^*\partial_{n'}\phi|^{-}_{\Gamma_{kl}} = \pm\frac{1}{2}\partial_n\phi|^{-}_{\Gamma_{kl}}(\boldsymbol{r}) + \int_{\Gamma_{kl}} \partial_n G(\boldsymbol{r},\boldsymbol{r}')\partial'_n\phi|^{-}_{\Gamma_{kl}}(\boldsymbol{r}')\,\mathrm{d}S' \,, \tag{3.24}$$

$$\lim_{\boldsymbol{r}\to\Gamma_{kl}^{\pm}} \mathcal{D}^*\partial_{n'}\phi|^{+}_{\Gamma_{kl}} = \mp\frac{1}{2}\partial_n\phi|^{+}_{\Gamma_{kl}}(\boldsymbol{r}) + \int_{\Gamma_{kl}} \partial_n G(\boldsymbol{r},\boldsymbol{r}')\partial'_n\phi|^{+}_{\Gamma_{kl}}(\boldsymbol{r}')\,\mathrm{d}S' \,, \tag{3.25}$$

and

$$\lim_{\boldsymbol{r}\to\Gamma_{kl}^{\pm}} \mathcal{D}_v^*\boldsymbol{J}_{eq_k} = \pm\frac{1}{2}\,\hat{\boldsymbol{n}}\cdot\boldsymbol{J}_{eq_k}(\boldsymbol{r}) + \int_{\Omega_k} \partial_n G(\boldsymbol{r},\boldsymbol{r}')\nabla'\cdot\boldsymbol{J}_{eq_k}(\boldsymbol{r}')\,\mathrm{d}V' \,, \tag{3.26}$$

$$\lim_{\boldsymbol{r}\to\Gamma_{kl}^{\pm}} \mathcal{D}_v^*\boldsymbol{J}_{eq_l} = \mp\frac{1}{2}\,\hat{\boldsymbol{n}}\cdot\boldsymbol{J}_{eq_l}(\boldsymbol{r}) + \int_{\Omega_l} \partial_n G(\boldsymbol{r},\boldsymbol{r}')\nabla'\cdot\boldsymbol{J}_{eq_l}(\boldsymbol{r}')\,\mathrm{d}V' \,. \tag{3.27}$$

We therefore get for $\boldsymbol{r} \in \Gamma_{kl}$,

$$\delta_{j,k}\frac{\partial_n\phi|^-_{\Gamma_{kl}}}{2} + \delta_{j,l}\frac{\partial_n\phi|^-_{\Gamma_{kl}}}{2} + \mathcal{N}\phi|_{\partial\Omega_j} - \delta_{j,k}\frac{\partial_n\phi|^-_{\Gamma_{kl}}}{2} + \delta_{j,l}\frac{\partial_n\phi|^+_{\Gamma_{kl}}}{2} - \mathcal{D}^*\partial_{n'}\phi|^-_{\partial\Omega_j} - \delta_{j,k}\frac{\hat{\boldsymbol{n}}\cdot\boldsymbol{J}_{eq_k}}{2\sigma_k} + \delta_{j,l}\frac{\hat{\boldsymbol{n}}\cdot\boldsymbol{J}_{eq_l}}{2\sigma_l} + \frac{1}{\sigma_j}\mathcal{D}_v^*\boldsymbol{J}_{eq_j} = -\frac{1}{\sigma_j}\mathcal{D}_v^*\boldsymbol{J}_p|_{\Omega_j}\,. \quad (3.28)$$

For clarity, the terms are ordered such that the $\mathcal{D}^*$ and $\mathcal{D}_v^*$ operators are preceded by the two singular terms stemming from their discontinuity when $j = k$ and $j = l$.

Let us now introduce the normal jump of the electric field on each interface, defined for $\boldsymbol{r} \in \Gamma_{kl}$ as

$$\xi(\boldsymbol{r}) = \nabla_n\phi|^-_{\Gamma}(\boldsymbol{r}) - \nabla_n\phi|^+_{\Gamma}(\boldsymbol{r})\,. \quad (3.29)$$

Summing (3.28) over all regions Ω_j, the term $\mathcal{N}\phi$ disappears by continuity of ϕ (c.f. (3.7a)) and we get a surface integral equation for each interface Γ_{kl} ($1 \le k < l \le N$) separating the domains Ω_k and Ω_l,

$$\partial_n\phi|^-_{\Gamma_{kl}} - \frac{\xi_{kl}}{2} + \hat{\boldsymbol{n}}\cdot\left(\frac{\boldsymbol{J}_{eq_l}}{2\sigma_l} - \frac{\boldsymbol{J}_{eq_k}}{2\sigma_k}\right) - \sum_{m,n=1}^{N+1}\mathcal{D}^*\xi_{mn} + \sum_{j=1}^{N}\frac{1}{\sigma_j}\mathcal{D}_v^*\boldsymbol{J}_{eq_j} = -\sum_{j=1}^{N}\frac{1}{\sigma_j}\mathcal{D}_v^*\boldsymbol{J}_p|_{\Omega_j}\,. \quad (3.30)$$

Approaching Γ_{kl} from the other side, i.e. for $\boldsymbol{r} \in \Omega_l$, we derive from (3.15),

$$\delta_{j,l}\phi + \frac{1}{\sigma_j}\mathcal{S}_v(\boldsymbol{J}_p|_{\Omega_j} + \boldsymbol{J}_{eq_j}) = \mathcal{S}\partial_{n'_o}\phi|^-_{\partial\Omega_j} - \mathcal{D}\phi|_{\partial\Omega_j}\,. \quad (3.31)$$

Using (3.19), (3.24) and (3.26), the outer limit $\boldsymbol{r} \to \Gamma_{kl}$ followed by a normal derivative reads

$$\delta_{j,k}\frac{\partial_n\phi|^+_{\Gamma_{kl}}}{2} + \delta_{j,l}\frac{\partial_n\phi|^+_{\Gamma_{kl}}}{2} + \mathcal{N}\phi|_{\partial\Omega_j} + \delta_{j,k}\frac{\partial_n\phi|^-_{\Gamma_{kl}}}{2} - \delta_{j,l}\frac{\partial_n\phi|^+_{\Gamma_{kl}}}{2} - \mathcal{D}^*\partial_{n'}\phi|^-_{\partial\Omega_j} + \delta_{j,k}\frac{\hat{\boldsymbol{n}}\cdot\boldsymbol{J}_{eq_k}}{2\sigma_k} - \delta_{j,l}\frac{\hat{\boldsymbol{n}}\cdot\boldsymbol{J}_{eq_l}}{2\sigma_l} + \frac{1}{\sigma_j}\mathcal{D}_v^*\boldsymbol{J}_{eq_j} = -\frac{1}{\sigma_j}\mathcal{D}_v^*\boldsymbol{J}_p|_{\Omega_j}\,. \quad (3.32)$$

Finally, summing (3.32) over all regions Ω_j gives us another equation on Γ_{kl},

$$\partial_n\phi|^+_{\Gamma_{kl}} + \frac{\xi_{kl}}{2} - \hat{\boldsymbol{n}}\cdot\left(\frac{\boldsymbol{J}_{eq_l}}{2\sigma_l} - \frac{\boldsymbol{J}_{eq_k}}{2\sigma_k}\right) - \sum_{m,n=1}^{N+1}\mathcal{D}^*\xi_{mn} + \sum_{j=1}^{N}\frac{1}{\sigma_j}\mathcal{D}_v^*\boldsymbol{J}_{eq_j} = -\sum_{j=1}^{N}\frac{1}{\sigma_j}\mathcal{D}_v^*\boldsymbol{J}_p|_{\Omega_j}\,. \quad (3.33)$$

The boundary conditions (3.7b) enforce

$$\begin{aligned} & \hat{\boldsymbol{n}} \cdot \overline{\overline{\sigma}} \nabla \phi|_{\Gamma_{kl}}^{-} = \hat{\boldsymbol{n}} \cdot \overline{\overline{\sigma}} \nabla \phi|_{\Gamma_{kl}}^{+} \\ \Leftrightarrow \quad & \hat{\boldsymbol{n}} \cdot (\overline{\overline{\sigma}} + \sigma_k \mathbf{I} - \sigma_k \mathbf{I}) \nabla \phi|_{\Gamma_{kl}}^{-} = \hat{\boldsymbol{n}} \cdot (\overline{\overline{\sigma}} + \sigma_l \mathbf{I} - \sigma_l \mathbf{I}) \nabla \phi|_{\Gamma_{kl}}^{+} \\ \Leftrightarrow \quad & \sigma_k \partial_n \phi|_{\Gamma_{kl}}^{-} - \hat{\boldsymbol{n}} \cdot \boldsymbol{J}_{eq_k} = \sigma_l \partial_n \phi|_{\Gamma_{kl}}^{+} - \hat{\boldsymbol{n}} \cdot \boldsymbol{J}_{eq_l} \\ \Leftrightarrow \quad & \sigma_l \partial_n \phi|_{\Gamma_{kl}}^{+} - \sigma_k \partial_n \phi|_{\Gamma_{kl}}^{-} = \hat{\boldsymbol{n}} \cdot (\boldsymbol{J}_{eq_l} - \boldsymbol{J}_{eq_k}) \,. \end{aligned} \tag{3.34}$$

We then multiply (3.33) by σ_l and (3.30) by σ_k and subtract the two equations to obtain

$$\begin{aligned} & \sigma_l \partial_n \phi|_{\Gamma_{kl}}^{+} - \sigma_k \partial_n \phi|_{\Gamma_{kl}}^{-} + \frac{\sigma_l + \sigma_k}{2} \xi_{kl} - (\sigma_l + \sigma_k)\, \hat{\boldsymbol{n}} \cdot \left(\frac{\boldsymbol{J}_{eq_l}}{2\sigma_l} - \frac{\boldsymbol{J}_{eq_k}}{2\sigma_k} \right) \\ & - (\sigma_l - \sigma_k) \sum_{m,n=1}^{N+1} \mathcal{D}^* \xi_{mn} + (\sigma_l - \sigma_k) \sum_{j=1}^{N} \frac{1}{\sigma_j} \mathcal{D}_v^* \boldsymbol{J}_{eq_j} = -(\sigma_l - \sigma_k) \sum_{j=1}^{N} \frac{1}{\sigma_j} \mathcal{D}_v^* \boldsymbol{J}_p|_{\Omega_j} \,. \end{aligned} \tag{3.35}$$

Finally, inserting (3.34) into (3.35) and dividing by $(\sigma_l - \sigma_k)$ reads

$$\begin{aligned} & \frac{\sigma_l + \sigma_k}{2\,(\sigma_l - \sigma_k)} \xi_{kl} + \hat{\boldsymbol{n}} \cdot \left(\frac{\boldsymbol{J}_{eq_l}}{2\sigma_l} + \frac{\boldsymbol{J}_{eq_k}}{2\sigma_k} \right) - \sum_{m,n=1}^{N+1} \mathcal{D}^* \xi_{mn} + \sum_{j=1}^{N} \frac{1}{\sigma_j} \mathcal{D}_v^* \boldsymbol{J}_{eq_j} \\ & \qquad = - \sum_{j=1}^{N} \frac{1}{\sigma_j} \mathcal{D}_v^* \boldsymbol{J}_p|_{\Omega_j} \,. \end{aligned} \tag{3.36}$$

Note that no assumption about the nesting of the different regions was made to derive this equation. It is easily verified that in the piecewise homogeneous and isotropic case, the contrast $\overline{\overline{\chi}}$, and therefore $\boldsymbol{J}_{eq}$ vanish, so that (3.36) reduces to the standard adjoint double-layer BEM formulation presented in Section 2.2.4.

3.3.2 Volume Integral Equation

In the more general inhomogeneous and anisotropic case, the presence of an additional unknown $\boldsymbol{J}_{eq}$ on top of the standard surface unknown ξ means that we need another equation to make the system square and solvable. To this end, we start from equation (3.15) in any volume with anisotropy and inhomogeneity. For $\boldsymbol{r} \in \Omega_i, \overline{\overline{\chi}}_i \neq 0$, summing over all regions Ω_j, we obtain

$$\begin{aligned} & \phi + \sum_{j=1}^{N} \frac{1}{\sigma_j} \mathcal{S}_v (\boldsymbol{J}_p|_{\Omega_j} + \boldsymbol{J}_{eq_j}) = \sum_{j=1}^{N} \left(\mathcal{S} \partial_{n'} \phi|_{\partial\Omega_j}^{-} - \mathcal{D} \phi|_{\partial\Omega_j} \right) \\ \Leftrightarrow \quad & \phi - \sum_{k,l} \mathcal{S} \xi_{kl} + \sum_{j=1}^{N} \frac{1}{\sigma_j} \mathcal{S}_v \boldsymbol{J}_{eq_j} = - \sum_{j=1}^{N} \frac{1}{\sigma_j} \mathcal{S}_v \boldsymbol{J}_p|_{\Omega_j} \,. \end{aligned} \tag{3.37}$$

Indeed, the $\mathcal{D}\phi|_{\partial\Omega_j}$ contributions (c.f. (3.17)) cancel by continuity of ϕ, according to (3.7a). Taking the gradient of this last equation results in the volume integral equation

$$(\sigma_i \mathbf{I} - \overline{\overline{\sigma}})^{-1} \boldsymbol{J}_{eq_i} - \sum_{k,l} \nabla \mathcal{S} \xi_{kl} + \sum_{j=1}^{N} \frac{1}{\sigma_j} \nabla \mathcal{S}_v \boldsymbol{J}_{eq_j} = -\sum_{j=1}^{N} \frac{1}{\sigma_j} \nabla \mathcal{S}_v \boldsymbol{J}_p|_{\Omega_j} \,. \tag{3.38}$$

Note the slight abuse of notation in the special case when $\sigma_i \mathbf{I} - \overline{\overline{\sigma}}$ is not full rank, and thus not invertible. Equation (3.38) is an n-dimensional equation, where $n \in \{1,2,3\}$ is the number of orthogonal directions along which the contrast is not null. If there is no contrast in a given direction, then there is no equivalent current in that direction and therefore no need for a volume equation.

3.3.3 Wire Integral Equation

With the two previously derived equations (3.36) and (3.38), we already have an integral equation formulation that can solve the anisotropic forward problem with non-uniform conductivity in any part of the head. If we consider the two dominant anisotropic regions mentioned before, this means that we would get a volume integral equation in both brain and skull compartments. The skull is quite thin, so that a volume discretization would not significantly increase the number of unknowns with respect to a pure surface discretization of its boundary. However, the same cannot be said of the white matter, which takes up the majority of the total head volume. This appears quite burdensome because the formulation becomes dominantly volumetric and we would therefore lose the main advantage of the BEM.

Another disadvantage of a volume representation of the white matter anisotropy is the derivation of the conductivity tensor itself. Since the direct, in vivo measure of human white matter conductivity is unfeasible, the most common practice in literature consists in measuring instead the anisotropic diffusion of water particles from dMRI data [12, 131, 103]. The data is then locally fit for each white matter voxel (also called Diffusion Tensor Imaging (DTI) fitting) and further interpolated for each volume element of the mesh. Finally, the electrical conductivity is related to the water diffusivity via a linear relationship [118], i.e. for any $\boldsymbol{r}$ in a volume element with the water diffusivity tensor

$$\overline{\overline{d}}(\boldsymbol{r}) = U(\boldsymbol{r}) \begin{bmatrix} d_1(\boldsymbol{r}) & 0 & 0 \\ 0 & d_2(\boldsymbol{r}) & 0 \\ 0 & 0 & d_3(\boldsymbol{r}) \end{bmatrix} U^T(\boldsymbol{r}) \,, \tag{3.39}$$

the conductivity tensor shares the same eigenvectors (because the anisotropy originates from the same fiber structure) and there is a constant $k \in \mathbb{R}_+$ such that

$$\overline{\overline{\sigma}}(\boldsymbol{r}) = U(\boldsymbol{r}) \begin{bmatrix} kd_1(\boldsymbol{r}) & 0 & 0 \\ 0 & kd_2(\boldsymbol{r}) & 0 \\ 0 & 0 & kd_3(\boldsymbol{r}) \end{bmatrix} U^T(\boldsymbol{r})\,. \tag{3.40}$$

The DTI model approximation has a relatively coarse resolution and is challenged when resolving crossing fiber regions [91, 41]. Indeed, a tensor fit is inherently only able to model a single principal axon direction (the eigenvector associated to the highest eigenvalue). Therefore several fibers of different and not necessarily orthogonal orientations crossing through a millimeter-scale voxel cannot be accurately represented with DTI. Secondly, the conversion from water diffusion to electrical conductivity is a further model approximation which requires other priors and remains challenging to validate in the absence of ground truth. For these reasons, a consensus on this conversion has yet to be established [108, 60].

We circumvent all these problems with a completely different approach, based on a wire representation of the white matter anisotropy. Recent advances in tractography have led to the quantitative streamline reconstruction of the human connectome, in other words, they provide a mapping of the white matter fibers [125]. This alternative and arguably more direct representation is leveraged in the following to build a tailored model of the brain anisotropy. The anisotropic white matter domain is the wire bundle obtained by tractography and denoted as

$$\Lambda = \bigcup_{n=1}^{N_w} \Lambda_n\,, \tag{3.41}$$

where Λ_n is an individual wire. The white matter anisotropy described in (3.11) shows that by choosing a background white matter conductivity σ_{i_w} equal to the transversal conductivity of the white matter fibers, the conductivity contrast exists only along the fiber direction, i.e.

$$\overline{\overline{\chi}}(\boldsymbol{r} \in \Omega_{i_w}) = \left(\frac{\sigma_{i_w}}{\sigma_l} - 1\right) \hat{\boldsymbol{l}}\hat{\boldsymbol{l}}^T\,. \tag{3.42}$$

Therefore, in the fiber region, the volume unknown

$$\boldsymbol{J}_{eq_{i_w}} = \left(\frac{\sigma_{i_w}}{\sigma_l} - 1\right) \frac{\partial \phi}{\partial l}\, \hat{\boldsymbol{l}} = J_{eq_{i_w}}(l)\, \hat{\boldsymbol{l}} \tag{3.43}$$

is a scalar function along the fiber direction. Hence, by taking the derivative of (3.37) along $\hat{\boldsymbol{l}}$, we obtain the 1-dimensional wire integral equation

$$\frac{1}{\sigma_{i_w} - \sigma_l} J_{eq_{i_w}} - \sum_{k,l} \nabla_l \mathcal{S} \xi_{kl} + \sum_{j=0}^{N+1} \frac{1}{\sigma_j} \nabla_l \mathcal{S}_v \boldsymbol{J}_{eq_j} = - \sum_{j=0}^{N+1} \frac{1}{\sigma_j} \nabla_l \mathcal{S}_v \boldsymbol{J}_p|_{\Omega_j}\,. \tag{3.44}$$

Note that each wire is approximated as the concatenation of several thin cylinders. Denoting as N_c the total number of cylinders, the $\mathcal{S}_v$ operator in the white matter can be written as

$$\begin{aligned}(\mathcal{S}_v \boldsymbol{J}_{eq_{i_w}})(\boldsymbol{r}) &= \int_\Lambda G(\boldsymbol{r},\boldsymbol{r}')\nabla'\cdot\boldsymbol{J}_{eq_{i_w}}(\boldsymbol{r}')\,\mathrm{d}V' \\ &= \sum_{c=1}^{N_c}\int_{l'=0}^{L_c}\int_{\theta'=0}^{2\pi}\int_{\rho'=0}^{a_c} G(\boldsymbol{r},\boldsymbol{r}')\nabla'\cdot\boldsymbol{J}_{eq_{i_w}}(\boldsymbol{r}')\rho'\mathrm{d}\rho'\mathrm{d}\theta'\mathrm{d}l' \\ &= \sum_{c=1}^{N_c}\int_{l'=0}^{L_c} G_w(\boldsymbol{r},\boldsymbol{r}')J_{eq_{i_w}}(l')\,\mathrm{d}l'\,, \end{aligned} \tag{3.45}$$

where L_c and a_c are respectively the length and radius of the c^{th} cylinder and

$$G_w(\boldsymbol{r},\boldsymbol{r}') = \int_{\theta'=0}^{2\pi}\int_{\rho'=0}^{a} G(\boldsymbol{r},\boldsymbol{r}')\rho'\mathrm{d}\rho'\mathrm{d}\theta' \tag{3.46}$$

is the resulting wire kernel. It is also assumed that the wires are not intersecting with volumes or surfaces, i.e. they all lie inside the closed brain domain Ω_{i_w} which contains only wire anisotropy. This assumption appears reasonable considering the head geometry, and implies in particular that there is no singularity or junction between the wires and the other types of unknowns (surface or volume).

3.4 Discretization of the Integral Equations

3.4.1 Choice of Basis Functions

Given the wire (3.44), surface (3.36) and volume (3.38) integral equations, each type of unknown is expanded with a set of basis functions that approximate their value on small mesh elements and the integral equations are tested with the same set of functions to obtain a square system of discrete equations. The geometry is discretized as follows: surfaces are tesselated into triangular elements, volumes into tetrahedra and wires into segments.

2D Surface Basis Functions

The 2D surface unknowns ξ are discretized with pyramid basis functions following

$$\xi(\boldsymbol{r}) = \sum_{i=1}^{N_s}\alpha_i s_i(\boldsymbol{r})\,, \tag{3.47}$$

where N_s is the number of vertices in the surface mesh and the functions are defined as

$$s_i(\boldsymbol{r}) = \begin{cases} \dfrac{\|(\boldsymbol{r}-\boldsymbol{r}_k)\times(\boldsymbol{r}_j-\boldsymbol{r}_k)\|}{\|(\boldsymbol{r}_i-\boldsymbol{r}_k)\times(\boldsymbol{r}_j-\boldsymbol{r}_k)\|} & \boldsymbol{r}\in t_{ijk} \\ 0 & \text{otherwise}\,. \end{cases} \tag{3.48}$$

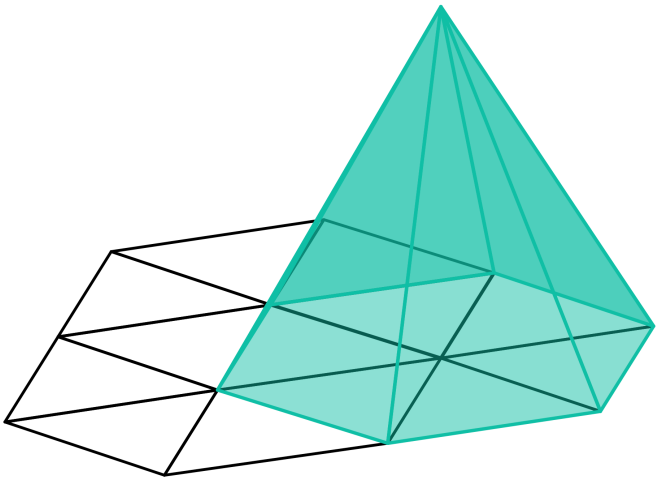

Figure 3.5: Pyramid basis function.

The support of the i^{th} pyramid function consists of each triangle t_{ijk} that includes the i^{th} vertex. The shape of a pyramid function is illustrated in Figure 3.5.

3D Volume Basis Functions

The volume current unknowns are expanded with Schaubert-Wilton-Glisson (SWG) basis functions [107]. The volume equivalent currents become

$$\boldsymbol{J}_{eq}(\boldsymbol{r}) = \overline{\overline{\chi}}\,\overline{\overline{\sigma}}\nabla\phi(\boldsymbol{r}) = \sum_{i=1}^{N_v} \overline{\overline{\chi}}\beta_i \boldsymbol{v}_i(\boldsymbol{r})\,, \tag{3.49}$$

where N_v is the number of faces in the volume mesh. An SWG function $\boldsymbol{v}_i$ is indexed by the i^{th} face separating any pair of tetrahedra denoted T_i^+ and T_i^-, and is defined as

$$\boldsymbol{v}_i(\boldsymbol{r}) = \begin{cases} \dfrac{a_i}{3V_i^+}(\boldsymbol{r} - \boldsymbol{r}_i^+) & \boldsymbol{r} \in T_i^+ \\ -\dfrac{a_i}{3V_i^-}(\boldsymbol{r} - \boldsymbol{r}_i^-) & \boldsymbol{r} \in T_i^- \\ \boldsymbol{0} & \text{otherwise}\,, \end{cases} \tag{3.50}$$

where a_i is the face area, and $V_i^\pm$ and $\boldsymbol{r}_i^\pm$ are the volume and free vertex of $T_i^\pm$. An example of SWG function is illustrated in Figure 3.6.

The SWG basis functions have two desirable properties: they are divergence conforming, i.e. they are smooth enough to apply the $\mathcal{S}_v$ and $\mathcal{D}_v^*$ operators, and they automatically enforce the continuity of the current $\overline{\overline{\sigma}}\nabla\phi$ across any pair of tetrahedra. They are therefore perfectly suitable for modeling local inhomogeneities within small volume elements (the tetrahedra). One may notice that half SWG

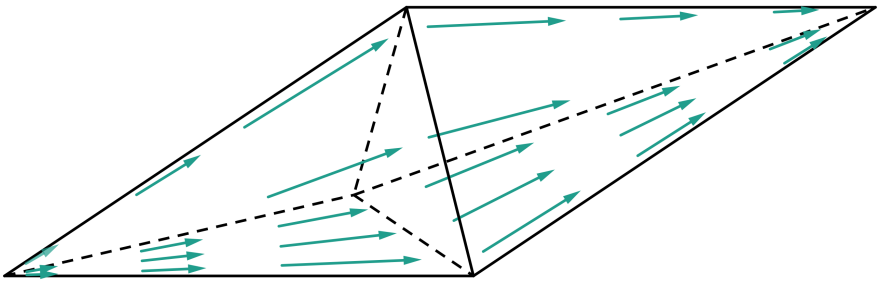

Figure 3.6: Schaubert-Wilton-Glisson basis function.

functions on the boundary of the tetrahedral mesh are an exception to this because they are defined on only one tetrahedron. However, the boundary triangles actually make up boundary surfaces Γ_{kl} on which the boundary conditions are explicitly handled by the surface equations (3.36).

1D Wire Basis Functions

Finally, equivalent currents along the wires are discretized with piecewise linear hat basis functions

$$\boldsymbol{J}_{eq_{i_w}}(\boldsymbol{r}) = \sum_{i=1}^{N_w} \overline{\overline{\chi}}\gamma_i w_i(l)\hat{\boldsymbol{l}}(\boldsymbol{r})\,, \tag{3.51}$$

where N_w is the number of wire vertices. A hat function w_i oriented along the wire direction $\hat{\boldsymbol{l}}$ is indexed by the i^{th} wire vertex and defined over segment pairs $s_i^- = [\boldsymbol{r}_{i-1}; \boldsymbol{r}_i]$ and $s_i^+ = [\boldsymbol{r}_i; \boldsymbol{r}_{i+1}]$, as

$$\boldsymbol{w}_i(\boldsymbol{r}) = \begin{cases} \dfrac{\boldsymbol{r} - \boldsymbol{r}_{i-1}}{\|\boldsymbol{r}_i - \boldsymbol{r}_{i-1}\|} & \boldsymbol{r} \in s_i^- \\ \dfrac{\boldsymbol{r}_{i+1} - \boldsymbol{r}}{\|\boldsymbol{r}_{i+1} - \boldsymbol{r}_i\|} & \boldsymbol{r} \in s_i^+ \\ \boldsymbol{0} & \text{otherwise}\,. \end{cases} \tag{3.52}$$

A hat function is illustrated in Figure 3.7. Similarly to the SWG functions, the hat functions are divergence conforming and enforce the continuity of the current across pairs of fiber segments. After discretization, the unknowns of the EEG forward problem are now the coefficients α_i, β_i and γ_i.

3.4.2 Solution of the Forward Problem

Given the discretization of the solution, we define the following discrete operator matrices, obtained by applying the continuous operators in the hybrid integral equations to the source basis functions and testing each equation with the corresponding testing basis functions. Denoting as s_i a pyramid function belonging to

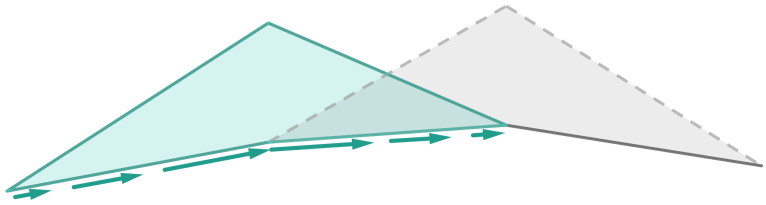

Figure 3.7: Hat basis function.

the interface Γ_{kl} separating the compartments Ω_k and Ω_l, $\boldsymbol{u}_i$ an SWG or hat basis function in the domain Ω_i, and

$$\langle a, b\rangle_\kappa = \int_\kappa a(\boldsymbol{r})b(\boldsymbol{r})\,\mathrm{d}\kappa\,, \tag{3.53}$$

$$\langle \boldsymbol{a}, \boldsymbol{b}\rangle_\kappa = \int_\kappa \boldsymbol{a}(\boldsymbol{r})\cdot\boldsymbol{b}(\boldsymbol{r})\,\mathrm{d}\kappa\,, \tag{3.54}$$

we have the block operator matrices

$$(\mathbf{G}_{\mathbf{ss}})_{ij} = \frac{\sigma_k+\sigma_l}{2}\langle s_i, s_j\rangle_{\Gamma_{kl}}\,, \tag{3.55}$$

$$(\mathbf{D}^*_{\mathbf{ss}})_{ij} = (\sigma_l-\sigma_k)\langle s_i, \mathcal{D}^* s_j\rangle_{\Gamma_{kl}}\,, \tag{3.56}$$

$$(\mathbf{D}^*_{\mathbf{su}})_{ij} = \frac{\sigma_l-\sigma_k}{\sigma_j}\langle s_i, \mathcal{D}^*_v\overline{\overline{\chi}}\boldsymbol{u}_j\rangle_{\Gamma_{kl}}\,, \tag{3.57}$$

$$(\mathbf{G}_{\mathbf{su}})_{ij} = \frac{\sigma_k+\sigma_l}{2\sigma_j}\langle s_i, \hat{\boldsymbol{n}}\cdot\overline{\overline{\chi}}\boldsymbol{u}_j\rangle_{\Gamma_{kl}}\,, \tag{3.58}$$

$$(\mathbf{S}_{\mathbf{us}})_{ij} = \langle \boldsymbol{u}_i, \nabla\mathcal{S}s_j\rangle_{\Omega_i}\,, \tag{3.59}$$

$$(\mathbf{G}_{\mathbf{uu}})_{ij} = \overline{\overline{\sigma}}^{-1}\langle \boldsymbol{u}_i, \boldsymbol{u}_j\rangle_{\Omega_i}\,, \tag{3.60}$$

$$(\mathbf{S}_{\mathbf{uu}})_{ij} = \frac{1}{\sigma_j}\langle \boldsymbol{u}_i, \nabla\mathcal{S}_v\overline{\overline{\chi}}\boldsymbol{u}_j\rangle_{\Omega_i}\,, \tag{3.61}$$

and the right-hand side vectors

$$(\boldsymbol{b}_{\boldsymbol{s}})_i = -(\sigma_k-\sigma_l)\langle s_i, \sum_j \frac{1}{\sigma_j}\mathcal{D}^*_v\boldsymbol{J}_p|_{\Omega_j}\rangle_{\Gamma_{kl}}\,, \tag{3.62}$$

$$(\boldsymbol{b}_{\boldsymbol{u}})_i = -\langle \boldsymbol{u}_i, \sum_j \frac{1}{\sigma_j}\nabla\mathcal{S}_v\boldsymbol{J}_p|_{\Omega_j}\rangle_{\Omega_i}\,. \tag{3.63}$$

Combining all discrete equations together, we finally obtain the hybrid system of the form $\mathbf{A}\boldsymbol{x} = \boldsymbol{b}$ as

$$\begin{bmatrix} \mathbf{G}_{\mathbf{ss}}-\mathbf{D}^*_{\mathbf{ss}} & \mathbf{G}_{\mathbf{sv}}-\mathbf{D}^*_{\mathbf{sv}} & -\mathbf{D}^*_{\mathbf{sw}} \\ -\mathbf{S}_{\mathbf{vs}} & \mathbf{G}_{\mathbf{vv}}+\mathbf{S}_{\mathbf{vv}} & \mathbf{S}_{\mathbf{vw}} \\ -\mathbf{S}_{\mathbf{ws}} & \mathbf{S}_{\mathbf{wv}} & \mathbf{G}_{\mathbf{ww}}+\mathbf{S}_{\mathbf{ww}} \end{bmatrix} \begin{bmatrix} \boldsymbol{\alpha} \\ \boldsymbol{\beta} \\ \boldsymbol{\gamma} \end{bmatrix} = \begin{bmatrix} \boldsymbol{b}_{\boldsymbol{s}} \\ \boldsymbol{b}_{\boldsymbol{v}} \\ \boldsymbol{b}_{\boldsymbol{w}} \end{bmatrix}\,. \tag{3.64}$$

This system is ill-conditioned in the top left block $\mathbf{A}_{\mathbf{ss}} = \mathbf{G}_{\mathbf{ss}} - \mathbf{D}^*_{\mathbf{ss}}$, corresponding to the surface-surface operator matrix. Indeed, it has a well-known singularity stemming from the fact that the potential is defined up to a constant. It is removed by deflation [26], i.e. replacing $\mathbf{A}_{\mathbf{ss}}$ by $\tilde{\mathbf{A}}_{\mathbf{ss}}$ with

$$\tilde{\mathbf{A}}_{\mathbf{ss}} = \mathbf{A}_{\mathbf{ss}} + \lambda \mathbf{1}\,, \tag{3.65}$$

where λ is a small positive constant and $\mathbf{1}$ is the matrix containing only ones. After solving the system matrix for the $N_{DoF} = N_s + N_v + N_w$ unknowns $\boldsymbol{\alpha}$, $\boldsymbol{\beta}$ and $\boldsymbol{\gamma}$, the solution of the EEG forward problem is obtained by inserting (3.47), (3.49) and (3.51) in (3.37) as

$$\phi(\boldsymbol{r}) = \sum_{k=1}^{N_s} \alpha_k \mathcal{S} s_k(\boldsymbol{r}) - \sum_{i=1}^{N} \frac{1}{\sigma_i} \left(\sum_{k=1}^{N_v} \beta_k \mathcal{S}_v^* \overline{\overline{\chi}}_i \boldsymbol{v}_k(\boldsymbol{r}) + \sum_{k=1}^{N_w} \gamma_k \mathcal{S}_v^* \overline{\overline{\chi}}_i \boldsymbol{w}_k(\boldsymbol{r}) + \mathcal{S}_v^* \boldsymbol{J}_p|_{\Omega_i}(\boldsymbol{r}) \right). \tag{3.66}$$

3.4.3 Implementation Details

The hybrid system matrix $\mathbf{A}$ in (3.64) is made of a number of block operators. Each entry in these blocks corresponds to the interaction between a testing and a source basis function. When their respective supports are spatially far from each other, the corresponding interaction (a far field interaction) is easily and accurately computed via a numerical quadrature scheme. Instead, in the near field, the kernels $G(\boldsymbol{r}, \boldsymbol{r}')$ and $\hat{\boldsymbol{n}} \cdot \nabla G(\boldsymbol{r}, \boldsymbol{r}')$ of the single- and double-layer operators are not smooth and even exhibit a singularity in the special case of self interactions (or more generally, when the testing and source domains intersect). In this case, it is necessary to compute the source integral analytically. We detail here the computation of self and near interactions of each block appearing in the system matrix.

Surface Source Integrals

The integral of a source pyramid basis function in the double-layer operator matrix $\mathbf{D}^*_{\mathbf{ss}}$ is the sum of the integrals of its restriction to each triangle t' of its support. On each such triangle, the pyramid is a linear function N that is equal to 1 on one of the triangle vertices and decreases to zero on the other two vertices. Following the singularity extraction technique described in [49], we compute analytically the integral

$$\begin{aligned} \boldsymbol{I}_{1|t'} &= \int_{\boldsymbol{r}' \in t'} N(\boldsymbol{r}') \nabla \frac{1}{R} \, \mathrm{d}S' \\ &= \int_{\boldsymbol{r}' \in t'} N(\boldsymbol{r}') \, \frac{\boldsymbol{r}' - \boldsymbol{r}}{R^3} \, \mathrm{d}S' \,, \end{aligned} \tag{3.67}$$

where $R = \|\boldsymbol{r} - \boldsymbol{r}'\|$. The entries of $\mathbf{D}^*_{\mathbf{ss}}$ are then obtained by taking the dot product of $\boldsymbol{I}_{1|t'}$ with the triangle normal and applying a Gaussian quadrature for the testing integral. For intersecting source and testing domains, the interaction is directly set to zero since $\boldsymbol{r}$ and $\boldsymbol{r}'$ both belong to t' so that $\hat{\boldsymbol{n}} \cdot (\boldsymbol{r} - \boldsymbol{r}') = 0$. As explained in Section 3.3, the singularity of the adjoint double-layer operator gives rise to the surface Gram operator $\mathbf{G}_{\mathbf{ss}}$.

Next, we use the divergence theorem to transfer the source gradient in the volume-surface operator $\mathbf{S}_{\mathbf{vs}}$ to the testing side as

$$\begin{aligned}(\mathbf{S}_{\mathbf{vs}})_{ij} &= \langle \boldsymbol{v}_i, \nabla \mathcal{S} s_j \rangle_{\Omega_i} \\ &= \langle \hat{\boldsymbol{n}}_o \cdot \boldsymbol{v}_i, \mathcal{S} s_j \rangle_{\partial\Omega_i} - \langle \nabla \cdot \boldsymbol{v}_i, \mathcal{S} s_j \rangle_{\Omega_i} \,, \end{aligned} \tag{3.68}$$

where $\hat{\boldsymbol{n}}_o$ is the outward normal on the boundary of the SWG support. Since the SWG functions are tangential on the boundary of the pair of tetrahedra, we have $\hat{\boldsymbol{n}}_o \cdot \boldsymbol{v}_i = 0$ and the first term of (3.68) disappears for full SWG functions. Instead, for half SWG functions, i.e. SWG functions that are defined on only one tetrahedron, the defining face t_i is part of the boundary, so that $\hat{\boldsymbol{n}}_o \cdot \boldsymbol{v}_i = \pm 1$ for $\boldsymbol{r} \in t_i$, where the sign depends on whether the unique tetrahedron of the half SWG corresponds to T_i^+ or T_i^-. For both terms of (3.68), we see that the source integral corresponds to a single-layer operator on a triangle, which can be computed via the singularity extraction of the integral (also presented in [49])

$$I_{2|t'} = \int_{\boldsymbol{r}' \in t'} N(\boldsymbol{r}') \frac{1}{R} \, \mathrm{d}S' \,. \tag{3.69}$$

The same reasoning can be applied for the $\mathbf{S}_{\mathbf{ws}}$ operator matrix, in which half hat basis functions appear on the wire extremities and give rise to an additional testing integral on a disk.

Volume Source Integrals

We leverage again the fact that the divergence operator can be used on the SWG functions to apply the divergence theorem for the $\mathbf{S}_{\mathbf{vv}}$ operator matrix

$$\begin{aligned}\sigma_j (\mathbf{S}_{\mathbf{vv}})_{ij} &= \langle \boldsymbol{v}_i, \nabla \mathcal{S}_v \overline{\overline{\chi}} \boldsymbol{v}_j \rangle_{\Omega_i} \\ &= \langle \hat{\boldsymbol{n}}_o \cdot \boldsymbol{v}_i, \mathcal{S}_v \overline{\overline{\chi}} \boldsymbol{v}_j \rangle_{\partial\Omega_i} - \langle \nabla \cdot \boldsymbol{v}_i, \mathcal{S}_v \overline{\overline{\chi}} \boldsymbol{v}_j \rangle_{\Omega_i} \,, \end{aligned} \tag{3.70}$$

where the first term disapppears for full SWG functions. The source integrals are decomposed into

$$\begin{aligned}\mathcal{S}_v\overline{\overline{\chi}}\boldsymbol{v}_j(\boldsymbol{r}) &= \int_{\boldsymbol{r}'\in\Omega_j} G(\boldsymbol{r},\boldsymbol{r}')\nabla'\cdot(\overline{\overline{\chi}}\boldsymbol{v}_j(\boldsymbol{r}'))\,\mathrm{d}V' \\ &= \frac{a_j}{3}\left(\int_{T_j^+} G(\boldsymbol{r},\boldsymbol{r}')\nabla'\cdot\left(\overline{\overline{\chi}}\,\frac{\boldsymbol{r}'-\boldsymbol{r}_j^+}{V_j^+}\right)\mathrm{d}V'\right. \\ &\quad \left. -\int_{T_j^-} G(\boldsymbol{r},\boldsymbol{r}')\nabla'\cdot\left(\overline{\overline{\chi}}\,\frac{\boldsymbol{r}'-\boldsymbol{r}_j^-}{V_j^-}\right)\mathrm{d}V'\right) \\ &= \frac{a_j}{12\pi V_j^+}I_{3|T_j^+} - \frac{a_j}{12\pi V_j^-}I_{3|T_j^-}\,. \end{aligned} \tag{3.71}$$

Therefore, the source integral boils down to the computation of

$$\begin{aligned} I_{3|T'} &= \int_{\boldsymbol{r}'\in T'}\frac{1}{R}\nabla'\cdot(\overline{\overline{\chi}}(\boldsymbol{r}'-\boldsymbol{r}_v))\,\mathrm{d}V' \\ &= \int_{\boldsymbol{r}'\in T'}\frac{tr(\overline{\overline{\chi}})}{3R}\,\mathrm{d}V' - \int_{\boldsymbol{r}'\in\partial T'}\frac{1}{R}\,\hat{\boldsymbol{n}}_o\cdot\overline{\overline{\chi}}(\boldsymbol{r}'-\boldsymbol{r}_v)\,\mathrm{d}S' \\ &= \frac{tr(\overline{\overline{\chi}})}{3}I_{4|T'} - \sum_{k=1}^{4}\left(\overline{\overline{\chi}}\hat{\boldsymbol{n}}_k\cdot\boldsymbol{I}_{5|\partial T_k'} + (\hat{\boldsymbol{n}}_k\cdot\overline{\overline{\chi}}\boldsymbol{r}_v)I_{6|\partial T_k'}\right)\,, \end{aligned} \tag{3.72}$$

where $tr(\cdot)$ is the trace operator and we used the fact that $\overline{\overline{\chi}}$ is symmetric. Thus we need to compute the three integrals:

- $I_{4|T'}$, the single-layer operator for a constant (pulse) source function integrated over a tetrahedron;
- $\boldsymbol{I}_{5|\partial T_k'}$, the single-layer operator for a linear source function in $\boldsymbol{r}'$ integrated over a triangular face $\partial T_k'$;
- $I_{6|\partial T_k'}$, the single-layer operator for a constant (pulse) source function integrated over the same triangle.

All three integrals are derived analytically from e.g. [49] and [128], by transforming tetrahedron integrals into triangle integrals, and triangle integrals into edge integrals via successive applications of the Gauss divergence theorem. The operator matrix $\mathbf{S_{wv}}$ has the same source integrals as $\mathbf{S_{vv}}$ and is therefore obtained in the same manner.

Lastly, the operator matrix $\mathbf{D^*_{sv}}$ contains the most intricate source integral since the normal derivative cannot be transferred to the testing side. For a full SWG

function, this corresponds to

$$\begin{aligned}\mathcal{D}_v^*\overline{\overline{\chi}}\boldsymbol{v}_j(\boldsymbol{r}) &= \int_{\boldsymbol{r}'\in\Omega_j} \hat{\boldsymbol{n}}\cdot\nabla G(\boldsymbol{r},\boldsymbol{r}')\nabla'\cdot(\overline{\overline{\chi}}\boldsymbol{v}_j(\boldsymbol{r}'))\,\mathrm{d}V' \\ &= \frac{a_j}{3}\left(\int_{T_j^+}\partial_n G(\boldsymbol{r},\boldsymbol{r}')\nabla'\cdot\left(\overline{\overline{\chi}}\,\frac{\boldsymbol{r}'-\boldsymbol{r}_j^+}{V_j^+}\right)\mathrm{d}V'\right. \\ &\quad \left. -\int_{T_j^-}\partial_n G(\boldsymbol{r},\boldsymbol{r}')\nabla'\cdot\left(\overline{\overline{\chi}}\,\frac{\boldsymbol{r}'-\boldsymbol{r}_j^-}{V_j^-}\right)\mathrm{d}V'\right) \\ &= \frac{a_j}{12\pi V_j^+}I_{7|T_j^+} - \frac{a_j}{12\pi V_j^-}I_{7|T_j^-}\,. \end{aligned} \tag{3.73}$$

We thus need to compute the integral

$$\begin{aligned} I_{7|T'} &= \int_{\boldsymbol{r}'\in T'}\partial_n\left(\frac{1}{R}\right)\nabla'\cdot(\overline{\overline{\chi}}(\boldsymbol{r}'-\boldsymbol{r}_v))\,\mathrm{d}V' \\ &= \int_{\boldsymbol{r}'\in T'}\partial_n\left(\frac{1}{R}\right)\frac{tr(\overline{\overline{\chi}})}{3}\,\mathrm{d}V' - \int_{\boldsymbol{r}'\in\partial T'}\partial_n\left(\frac{1}{R}\right)\hat{\boldsymbol{n}}_o\cdot\overline{\overline{\chi}}\,(\boldsymbol{r}'-\boldsymbol{r}_v)\,\mathrm{d}S' \\ &= \frac{tr(\overline{\overline{\chi}})}{12\pi}I_{8|T'} - \sum_{k=1}^{4}\frac{1}{4\pi}\left(\overline{\overline{\chi}}\hat{\boldsymbol{n}}_k\cdot\boldsymbol{I}_{9|\partial T'_k} + (\hat{\boldsymbol{n}}_k\cdot\overline{\overline{\chi}}\boldsymbol{r}_v)\,\hat{\boldsymbol{n}}\cdot\boldsymbol{I}_{10|\partial T'_k}\right)\,. \end{aligned} \tag{3.74}$$

Applying the divergence theorem for the first integral, we get

$$\begin{aligned} I_{8|T'} &= -\hat{\boldsymbol{n}}\cdot\sum_{k=1}^{4}\hat{\boldsymbol{n}}_k\int_{\boldsymbol{r}'\in\partial T'_k}\frac{1}{R}\,\mathrm{d}S' \\ &= -\sum_{k=1}^{4}(\hat{\boldsymbol{n}}\cdot\hat{\boldsymbol{n}}_k)I_{6|\partial T'_k}\,. \end{aligned} \tag{3.75}$$

By expressing $\boldsymbol{r}'$ in the local coordinates of the integration triangle, the second integral can be decomposed into

$$\begin{aligned} \boldsymbol{I}_{9|\partial T'_k} &= \int_{\boldsymbol{r}'\in\partial T'_k}\hat{\boldsymbol{n}}\cdot\nabla\left(\frac{1}{R}\right)\boldsymbol{r}'\mathrm{d}S' \\ &= \int_{\partial T'_k}\hat{\boldsymbol{n}}\cdot\nabla\left(\frac{1}{R}\right)(\boldsymbol{p}_0+u\hat{\boldsymbol{u}}+v\hat{\boldsymbol{v}})\,\mathrm{d}S' \\ &= (\hat{\boldsymbol{n}}\cdot\boldsymbol{I}_{10|\partial T'_k})\,\boldsymbol{p}_0 + (\hat{\boldsymbol{n}}\cdot\boldsymbol{I}_{11|\partial T'_k})\,\hat{\boldsymbol{u}} + (\hat{\boldsymbol{n}}\cdot\boldsymbol{I}_{12|\partial T'_k})\,\hat{\boldsymbol{v}}\,, \end{aligned} \tag{3.76}$$

where the triangle notations are illustrated in Figure 3.8, and the integrals $\boldsymbol{I}_{10|t'}$, $\boldsymbol{I}_{11|t'}$ and $\boldsymbol{I}_{12|t'}$ on triangle t' can be computed analytically following [62].

Finally, in the special case where the observation point lies in the source triangle, which happens for all half source SWG functions which are tested by a pyramid function on the intersecting boundary, we have $\partial_n G = 0$, so the corresponding surface integral in $I_{7|T'}$ is set to zero and its singularity gives rise to the operator matrix $\mathbf{G_{sv}}$.

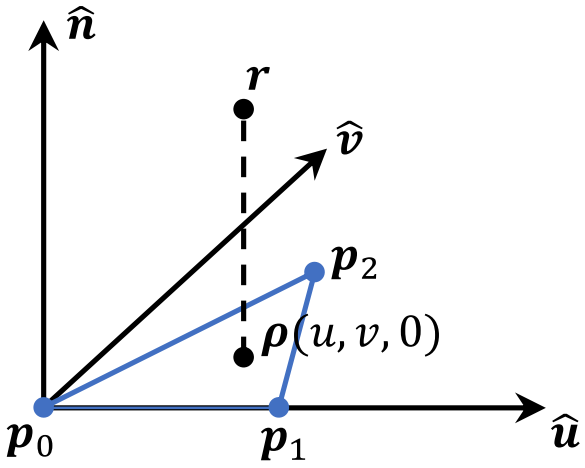

Figure 3.8: Example source triangle. A local coordinate system $(\hat{\boldsymbol{u}}, \hat{\boldsymbol{v}}, \hat{\boldsymbol{n}})$ centered on the first triangle vertex $\boldsymbol{p}_0$ is defined and $\boldsymbol{\rho}$ is the projection of the observation point $\boldsymbol{r}$ in the triangle plane.

Wire Source Integrals

The strategy employed for wire source integrals in the near field is similar to that adopted in [127], and consists in rewriting the 3D cylinder (volume) integral into a 1D segment integral by deriving a semi-analytical expression of the wire kernel (3.46) and leveraging the fact that the source basis function is constant over the cross section.

A singularity arises for self terms in S_{ww}. Again, transferring the gradient on the kernel to the testing side via the Gauss divergence theorem, the basis function contributions are constant on the integration domains (derivative of piecewise-linear functions). The remaining weak singularity is removed by writing the source integral in polar coordinates. Thus, for an observation point $\boldsymbol{r}$ on the wire segment, the source term $(\mathcal{S}_v \overline{\overline{\chi}} \boldsymbol{w}_j)(\boldsymbol{r})$ requires the evaluation of the integral on the cylinder

c' with radius a and length l

$$\begin{aligned} I_{13|c'} &= \int_{c'} \frac{1}{R}\,\mathrm{d}V' \\ &= \int_{z'=0}^{l}\int_{\theta'=0}^{2\pi}\int_{\rho'=0}^{a} \frac{\rho'}{\|\boldsymbol{r}-\boldsymbol{r}'\|}\,\mathrm{d}\rho'\mathrm{d}\theta'\mathrm{d}z' \\ &= 2\pi\int_{z'=0}^{l}\int_{\rho'=0}^{a} \frac{\rho'}{\sqrt{\rho'^2+(z-z')^2}}\,\mathrm{d}\rho'\mathrm{d}z' \\ &= 2\pi\int_{z'=0}^{l}\left(\sqrt{a^2+(z-z')^2}-|z-z'|\right)\mathrm{d}z' \\ &= \pi\left((l-z)\sqrt{a^2+(l-z)^2}+z\sqrt{a^2+z^2}\right. \\ &\quad \left. + a^2\log\frac{\sqrt{a^2+(l-z)^2}+l-z}{\sqrt{a^2+z^2}-z} - l^2+2zl-2z^2\right). \end{aligned} \tag{3.77}$$

Right-Hand Side

As defined previously, the right-hand side vector is obtained by testing the dipole excitation with each basis function. As usual, for SWG and hat functions, the gradient of the $\mathcal{S}_v$ operator in eq. (3.63) is transferred to the testing function. For instance, assume that the source is a dipole located at $\boldsymbol{r}_0 \in \Omega_1$ with a moment $\boldsymbol{q}$. The primary current density is thus given by (2.8). Considering a testing SWG function $\boldsymbol{v}_i$ defined on two tetrahedra T_i^+ and T_i^-, we have

$$\begin{aligned} (\boldsymbol{b}_v)_i &= -\langle \boldsymbol{v}_i, \sum_j \frac{1}{\sigma_j}\nabla\mathcal{S}_v\boldsymbol{J}_p|_{\Omega_j}\rangle_{T_i^+\cup T_i^-} \\ &= \frac{1}{\sigma_1}\langle \nabla\cdot\boldsymbol{v}_i, \mathcal{S}_v\boldsymbol{J}_p|_{\Omega_1}\rangle_{T_i^+\cup T_i^-} \\ &= \frac{1}{\sigma_1}\int_{T_i^+\cup T_i^-}\nabla\cdot(\boldsymbol{v}_i(\boldsymbol{r}))\int_{\Omega_1} G(\boldsymbol{r},\boldsymbol{r}')\nabla'\cdot(\boldsymbol{q}\,\delta(\boldsymbol{r}_0-\boldsymbol{r}'))\,\mathrm{d}V'\mathrm{d}V \\ &= \frac{1}{\sigma_1}\int_{T_i^+\cup T_i^-}\nabla\cdot(\boldsymbol{v}_i(\boldsymbol{r}))\,\boldsymbol{q}\cdot\nabla G(\boldsymbol{r},\boldsymbol{r}_0)\,\mathrm{d}V \\ &= \frac{a_i}{\sigma_1}\,\boldsymbol{q}\cdot\left(\frac{1}{V_i^+}\int_{T_i^+}\nabla G(\boldsymbol{r},\boldsymbol{r}_0)\,\mathrm{d}V + \frac{1}{V_i^-}\int_{T_i^-}\nabla G(\boldsymbol{r},\boldsymbol{r}_0)\,\mathrm{d}V\right), \end{aligned} \tag{3.78}$$

which can be evaluated numerically or analytically from (3.74). In contrast, the normal gradient cannot be applied to the surface basis functions. The right-hand

side entry tested with a pyramid function s_i supported in Γ_{kl} has the expression

$$\begin{aligned}(\boldsymbol{b_s})_i &= -(\sigma_k - \sigma_l)\langle s_i, \sum_j \frac{1}{\sigma_j}\mathcal{D}_v^* \boldsymbol{J}_p|_{\Omega_j}\rangle_{\Gamma_{kl}} \\ &= -\frac{(\sigma_k - \sigma_l)}{\sigma_1}\sum_{t_i}\int_{t_i} s_i(\boldsymbol{r})\,\hat{\boldsymbol{n}}\cdot\nabla\int_{\Omega_1} G(\boldsymbol{r},\boldsymbol{r}')\nabla'\cdot(\boldsymbol{q}\,\delta(\boldsymbol{r}_0-\boldsymbol{r}'))\,\mathrm{d}V'\mathrm{d}S \\ &= -\frac{(\sigma_k - \sigma_l)}{\sigma_1}\sum_{t_i}\int_{t_i} s_i(\boldsymbol{r})\,\hat{\boldsymbol{n}}\cdot\nabla(\boldsymbol{q}\cdot\nabla G(\boldsymbol{r},\boldsymbol{r}_0))\,\mathrm{d}S\,, \end{aligned} \tag{3.79}$$

which appears harder to evaluate than the previously derived integrals. Nevertheless, a closed-form analytical expression in terms of triangle edge integrals can still be obtained with the strategy described in [5].

3.5 Leadfield Computation

One major application of the EEG forward problem is the construction of a gain or leadfield matrix $\mathbf{L}$, which relates a distribution of N_d primary dipolar sources with unitary amplitude to a set of N_e measuring electrodes. Essentially, this corresponds to discretizing or quantizing the source and measurement spaces. We assume that the dipole distribution covers the whole brain with a fine enough resolution. Then, any brain activity can be modeled as the activation of one or several sources and is measured on the scalp electrodes as the linear combination of the columns of $\mathbf{L}$ corresponding to the activated sources according to the superposition principle. This leads to the equation

$$\begin{bmatrix}\phi_1\\ \phi_2\\ \vdots\\ \phi_{N_e}\end{bmatrix} = \begin{bmatrix}L_{11} & L_{12} & \dots & L_{1N_d}\\ L_{21} & L_{22} & & \vdots\\ \vdots & & \ddots & \vdots\\ L_{N_e1} & \dots & \dots & L_{N_eN_d}\end{bmatrix}\begin{bmatrix}j_1\\ j_2\\ \vdots\\ j_{N_d}\end{bmatrix}, \tag{3.80}$$

where ϕ_i is the measured potential on the i^{th} electrode and j_i is the amplitude of the i^{th} current dipole. From the solution described in the previous section, one way to obtain $\mathbf{L}$ would be to solve N_d forward problems, in which only one dipole per forward problem is active. This dipole constitutes the only contribution to $\boldsymbol{J}_p$ and the resulting potential is calculated by applying (3.66) for each electrode position. This means that we need to solve eq. (3.64) for N_d different right-hand sides $\boldsymbol{b}$, which appears quite computationally expensive when the source space is finely discretized (in typical applications, $N_d \approx 10^3$ to 10^4). Comparatively, the number of electrodes is quite small ($N_e \approx 10^1$ to 10^2), which can be exploited with the Helmholtz principle of reciprocity to drastically reduce the required computational effort. In matrix form, we have

$$\mathbf{L} = \mathbf{S}\mathbf{A}^{-1}\mathbf{B}\,, \tag{3.81}$$

where $\mathbf{A}$ is the hybrid system matrix, $\mathbf{B} = [\boldsymbol{b}_1 \dots \boldsymbol{b}_{N_d}]$ is the $N_{DoF} \times N_d$ matrix of right-hand sides (each column $\boldsymbol{b}_i$ corresponds to the unitary activation of a single dipole) and $\mathbf{S} = [\mathbf{S_{ms}}^T \mathbf{S_{mv}}^T \mathbf{S_{mw}}^T]^T$ is the $N_e \times N_{DoF}$ discrete single-layer operator point-tested at each electrode position $\boldsymbol{r}_i$,

$$(\mathbf{S_{ms}})_{ij} = \int_\Gamma G(\boldsymbol{r}_i, \boldsymbol{r}')\, s_j(\boldsymbol{r}')\, \mathrm{d}S' \tag{3.82}$$

$$(\mathbf{S_{mv}})_{ij} = \frac{1}{\sigma_j} \int_\Omega G(\boldsymbol{r}_i, \boldsymbol{r}') \nabla' \cdot (\overline{\overline{\chi}} \boldsymbol{v}_j(\boldsymbol{r}'))\, \mathrm{d}V' \tag{3.83}$$

$$(\mathbf{S_{mw}})_{ij} = \frac{1}{\sigma_j} \int_\Lambda G(\boldsymbol{r}_i, \boldsymbol{r}') \nabla' \cdot (\overline{\overline{\chi}} \boldsymbol{w}_j(\boldsymbol{r}'))\, \mathrm{d}V' \,. \tag{3.84}$$

For a small system, $\mathbf{A}$ can be inverted directly and then multiplied on the left by $\mathbf{S}$ and on the right by $\mathbf{B}$. However, a direct matrix inversion, e.g. via LU decomposition is a costly $\mathcal{O}(N_{DoF}^3)$ operation. Therefore, when the number of unknowns is too high, it is preferable to use a Krylov subspace method such as the Conjugate Gradient Squared method [114] or the Generalized Minimal Residual method [104]. As opposed to direct inversion, such methods do not invert the full matrix. Instead, for a given right-hand side vector $\boldsymbol{b}$, they iteratively look for a vector $\boldsymbol{x}$ that satisfies $\mathbf{A}\boldsymbol{x} = \boldsymbol{b}$ up to a tolerated residual error. Therefore, with iterative solvers, the time needed to compute the full leadfield is proportional to the number of right-hand sides.

In this context, applying the reciprocity principle is straightforward and corresponds to computing the leadfield from (3.81) as

$$\mathbf{L} = (\mathbf{S}\mathbf{A}^{-1})\mathbf{B}\,, \tag{3.85}$$

instead of

$$\mathbf{L} = \mathbf{S}(\mathbf{A}^{-1}\mathbf{B})\,, \tag{3.86}$$

where the parentheses determine the order in which the operations are done. This means that we can get the leadfield matrix by either solving the system for N_e left-hand sides or for N_d right-hand sides. Thus, when $N_d > N_e$, it is more advantageous to use (3.85).

The physical interpretation is that the electric potential between two electrodes and resulting from a unitary dipole source (formed by two points infinitely close to each other) is the same as the potential difference between these two points resulting from the unitary current injection and extraction at the two electrodes.

3.6 Wire Conductivity Model

Due to the high resistivity of the skull, it is quite difficult to get a precise estimate of the white matter conductivity, especially given its inhomogeneous and

anisotropic structure. Furthermore, while tractography provides us with a set a streamlines, the radius of each wire remains to be determined. Therefore we describe here a procedure to obtain a model of white matter conductivity consistent with dMRI.

The choice of the tractography algorithm and its parameters (step size, stopping criterion, seeding strategy, etc.) is impactful as different algorithms are known to produce very different tractograms both in terms of density and shape [74]. This is because the reconstructed streamlines are an estimation of the white matter structure based on an indirect observation (the measured water displacement). An interesting approach for the proposed hybrid formulation consists in clustering the tractogram streamlines [46], resulting in a more concise representation of the main conductive paths in the brain. Not only does it help reducing inter-tractography and parameter variability [47], but it also brings the resolution of the fiber structure to that of meshes used to discretize the other tissue geometries, thus reducing the number of fiber unknowns. As tractograms are an indirect representation of axon bundles, each individual streamline is understood as some cross-sectional area of white matter [112]. Therefore, given a total streamline length L, the wire radius a is adjusted to match a known volume of white matter V (approximately $450\,\mathrm{cm}^3$ [134]) as

$$a = \sqrt{\frac{V}{\pi L}}\,. \tag{3.87}$$

Note that in the proposed formulation, each wire may have a different radius. In fact, the estimation of individual wire radiuses can alternatively be part of the tractography routine as in [111, 33].

Once the radius is fixed, and given a longitudinal and radial white matter conductivity, we solve a homogenization problem to obtain an equivalent or effective homogeneous (but possibly anisotropic) brain conductivity. We consider only the inner domain Ω_1 containing all the wires, and for a given background conductivity σ_1 and longitudinal wire conductivity σ_l, we look for an effective conductivity $\overline{\overline{\sigma}}_e$ which satisfies

$$\langle \boldsymbol{J} \rangle = \overline{\overline{\sigma}}_e \langle \boldsymbol{E} \rangle\,, \tag{3.88}$$

where

$$\langle \cdot \rangle = \frac{1}{V_{\Omega_1}} \int_{\Omega_1} \cdot \,\mathrm{d}V \tag{3.89}$$

denotes the volume average over Ω_1. By imposing a boundary condition on the normal component of the current density $\overline{\overline{\sigma}}\nabla\phi$ on the boundary $\partial\Omega_1$, i.e.

$$\hat{\boldsymbol{n}} \cdot \overline{\overline{\sigma}}\nabla\phi = \hat{\boldsymbol{n}} \cdot \boldsymbol{J}_0\,, \quad \boldsymbol{r} \in \partial\Omega_1\,, \tag{3.90}$$

where $\boldsymbol{J}_0$ is an imposed current density, the volume average for the component

along the x-axis of the current density satisfies

$$\begin{aligned}\langle \boldsymbol{J} \rangle_x &= \frac{1}{V_{\Omega_1}} \int_{\Omega_1} \hat{\boldsymbol{x}} \cdot \boldsymbol{J} \, \mathrm{d}V \\ &= \frac{1}{V_{\Omega_1}} \int_{\Omega_1} \nabla \cdot (x\boldsymbol{J}) \, \mathrm{d}V - \frac{1}{V_{\Omega_1}} \int_{\Omega_1} x \, \nabla \cdot \boldsymbol{J} \, \mathrm{d}V \,, \end{aligned} \tag{3.91}$$

where we used the vector calculus identity for a scalar a and a vector $\boldsymbol{b}$,

$$\nabla \cdot (a\boldsymbol{b}) = a \nabla \cdot \boldsymbol{b} + (\nabla a) \cdot \boldsymbol{b} \,. \tag{3.92}$$

In the absence of an internal primary source, the Poisson's equation (3.12) reduces to $\nabla \cdot \boldsymbol{J} = 0$ so the second term in (3.91) vanishes. Using Gauss divergence theorem, it follows that

$$\begin{aligned}\langle \boldsymbol{J} \rangle_x &= \frac{1}{V_{\Omega_1}} \int_{\Omega_1} \nabla \cdot (x\boldsymbol{J}) \, \mathrm{d}V \\ &= \frac{1}{V_{\Omega_1}} \int_{\partial\Omega_1} x\boldsymbol{J} \cdot \hat{\boldsymbol{n}} \, \mathrm{d}S \\ &= \frac{\boldsymbol{J}_0}{V_{\Omega_1}} \cdot \int_{\partial\Omega_1} x\hat{\boldsymbol{n}} \, \mathrm{d}S \\ &= \frac{\boldsymbol{J}_0}{V_{\Omega_1}} \cdot \int_{\Omega_1} \nabla x \, \mathrm{d}V \\ &= \boldsymbol{J}_0 \cdot \hat{\boldsymbol{x}} \\ &= \boldsymbol{J}_{0x} \,. \end{aligned} \tag{3.93}$$

Applying the same reasoning for the $\hat{\boldsymbol{y}}$ and $\hat{\boldsymbol{z}}$ unit vectors, we thus obtain

$$\langle \boldsymbol{J} \rangle = \boldsymbol{J}_0 \,. \tag{3.94}$$

Then, we apply the hybrid integral equation formulation presented in Section 3.3 to obtain the scalar potential ϕ on $\partial\Omega_1$. The volume average of the electric field is then given by

$$\langle \boldsymbol{E}^{(\boldsymbol{J}_0)} \rangle = -\frac{1}{V_{\Omega_1}} \int_{\partial\Omega_1} \phi \hat{\boldsymbol{n}} \, \mathrm{d}S \,, \tag{3.95}$$

where the subscript on the vector $\boldsymbol{E}^{(\boldsymbol{J}_0)}$ indicates the dependency on the imposed current. Thus, solving three forward problems for $\boldsymbol{J}_0 \in \{\hat{\boldsymbol{x}}, \hat{\boldsymbol{y}}, \hat{\boldsymbol{z}}\}$ gives us the effective conductivity as

$$\overline{\overline{\sigma}}_e = \begin{bmatrix} \langle \boldsymbol{E}^{(\boldsymbol{x})} \rangle_x & 0 & 0 \\ 0 & \langle \boldsymbol{E}^{(\boldsymbol{y})} \rangle_y & 0 \\ 0 & 0 & \langle \boldsymbol{E}^{(\boldsymbol{z})} \rangle_z \end{bmatrix}^{-1} . \tag{3.96}$$

By definition, as $\overline{\overline{\sigma}}_e$ satisfies Ohm's law (3.88) averaged over the volume, it corresponds to the electrically equivalent average (homogenized) conductivity of the inhomogeneous domain Ω_1 for the specified boundary condition (3.90). This value can then be compared with brain conductivity values reported in literature to ensure that the obtained wire-based conductivity model of the white matter is realistic.

3.7 Numerical Results

A series of numerical experiments are showcased to demonstrate the validity of the new hybrid formulation. This is achieved by comparing its solution with reference solutions obtained from other solvers. Although analytical and semi-analytical solutions exist for spherical models [37, 135], comparison for more complex shapes such as a realistically shaped skull or the fibers in the white matter can only be performed against other numerical solutions. In that case, a reference solution is obtained from a commercial finite element solver (COMSOL Multiphysics) applied on a highly refined mesh with high order basis functions to minimize the impact of discretization errors.

3.7.1 Validation on Canonical Models

Piecewise-Homogeneous Spherical Model

Following a well-established practice in literature [83], we first benchmark the accuracy of the formulation with a standard 3-layer spherical model which approximates the head with three concentric spheres corresponding, in order, to the brain, skull and scalp compartments. This geometry is depicted in Figure 3.9a. The layers have normalized radiuses of 0.87, 0.92, and 1, and piecewise conductivities of 0.33, 0.01 and $0.33\,\mathrm{S\,m^{-1}}$, respectively. The average mesh element size is 0.1, resulting in a total of 4220 vertices and 8528 triangles. In this piecewise isotropic case, the conductivity contrast is null and the proposed formulation is equivalent to the adjoint double-layer BEM [66]. Hence, this scenario allows us to verify the accuracy of the surface integral equations alone.

A current dipole acting as the primary source is placed along the x-axis with a dipole moment of $[1\,,1\,,1]$ in the cartesian xyz-coordinate system. For comparison with standard numerical solvers, a symmetric BEM solution is computed with OpenMEEG [50], along with a FEM solution obtained with the FieldTrip toolbox [90]. In all formulations, we have used the same mesh element size, as well as piecewise linear basis functions. The accuracy is measured as the relative ℓ_2-error of the scalp electric potential, i.e.

$$\epsilon = \frac{\|\boldsymbol{x}_{ref} - \boldsymbol{x}\|}{\|\boldsymbol{x}_{ref}\|}\,, \tag{3.97}$$

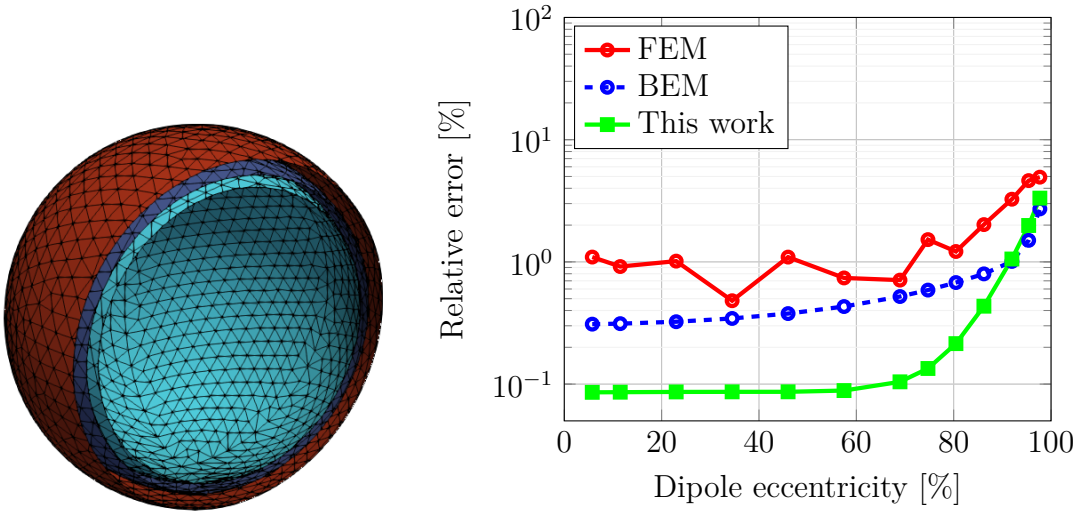

(a) (b)

Figure 3.9: (a) 3-layer isotropic head geometry modeled as three concentric spheres with constant conductivity and (b) relative error of the proposed and standard methods with respect to an analytical solution.

and is plotted in Figure 3.9b as a function of the eccentricity of the source, since sources closer to the surfaces are more sensitive to discretization errors. All solutions display good accuracy, with less than 5 % relative error compared to the analytical solution across all dipole positions. As expected [66], the hybrid (adjoint double-layer) formulation is the most accurate representation up to 90% eccentricity, over which the distance to the surface of discontinuity gets smaller than the mesh element size.

Spherical Model with Anisotropic Skull

Next, we add anisotropy in the skull by discretizing the volume between the two innermost spheres as shown in Figure 3.10a. The conductivity tensor described in Section 3.2.2 is computed with hard bone conductivity $\sigma_{hard} = 6.4\,\mathrm{mS\,m^{-1}}$ and soft bone conductivity $\sigma_{soft} = 26.85\,\mathrm{mS\,m^{-1}}$ [34]. The soft bone thickness $t_s(\boldsymbol{r}) \in [0,\ 1]$ is defined such that it is equal to 1 in an arbitrary position $\boldsymbol{p} = \begin{bmatrix}0.9 & 0 & 0\end{bmatrix}^T$ within the skull and decreases linearly to 0 according to the distance to $\boldsymbol{p}$. This results in a non spherically symmetric, inhomogeneous and anisotropic conductivity profile for which no analytical solution is readily available. Therefore, the reference is instead a FEM solution obtained with the COMSOL Multiphysics software, computed with quadratic basis functions on a refined mesh. Just like in the first example, FieldTrip FEM and OpenMEEG (symmetric) BEM solutions with the same mesh resolutions as in the hybrid solver are presented for comparison. For the BEM solution, an

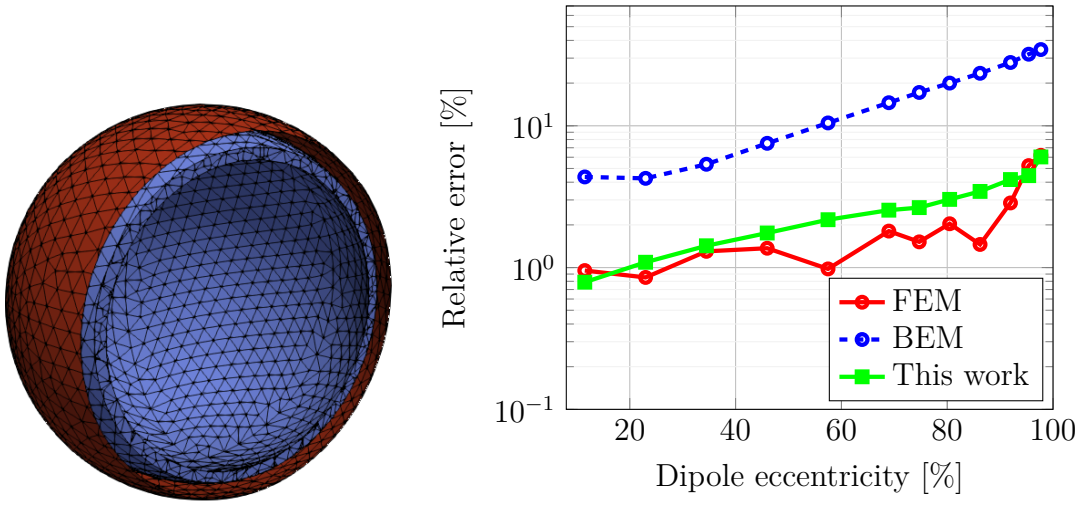

(a) (b)

Figure 3.10: (a) 3-layer head geometry with inhomogeneous skull conductivity. The skull anisotropy is accounted for by discretizing the skull volume (in between the first two spheres) with tetrahedral elements; (b) relative error of the proposed and standard methods with respect to a high resolution FEM solution.

isotropic conductivity value of $0.01\,\mathrm{S\,m^{-1}}$ for the skull is used.

The relative errors are displayed in Figure 3.10b. The impact of skull anisotropy is clear: for very deep sources, which are far away from the skull layer, the isotropic conductivity value is a reasonable approximation (less than 5 % error for symmetric BEM), but the error progressively increases for shallower sources since a single constant scalar value cannot account for the anisotropy and heterogeneity close to volume elements. The relative errors are also higher for the anisotropy-handling FEM and proposed solutions when compared to the simpler isotropic case, but they still remain well below 5 % even for sources close to the skull. The similar level of accuracy of both formulations highlights the ability of the proposed method to match the anisotropic modeling with volume elements just as well as a FEM-based formulation.

Spherical Model with Anisotropic Skull and White Matter

Finally, we further complexify the spherical model by adding a white matter contribution in the form of bundles of fibers oriented along the x- and y-axes within the innermost sphere, as illustrated in Figure 3.11a. The 30 cylindrical fibers have a normalized radius of 0.05, a length of 1.4 and a longitudinal conductivity that is ten times that of the background. Again, a higher resolution FEM solution with quadratic basis functions (3 110 264 unknowns, $h = 0.03$) is used as reference. As explained in Section 3.4.1, no tetrahedral discretization in the inner sphere is needed

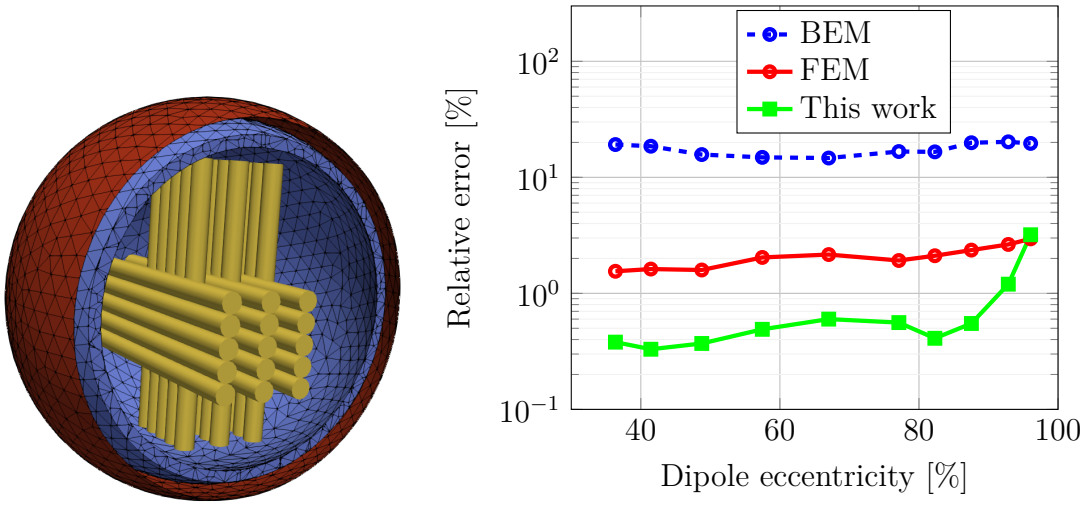

(a) (b)

Figure 3.11: (a) 3-layer spherical head geometry with inhomogeneous skull and white matter. The skull anisotropy is accounted for by discretizing the skull volume with tetrahedral elements whereas the fibrous white matter anisotropy is modeled with x- and y-oriented bundles of 15 cylindrical fibers along which the white matter is 10 times more conductive; (b) relative error of the proposed and standard methods with respect to a high resolution FEM solution.

for the hybrid solver, and instead, each fiber axis is meshed into 14 segments of length 0.1. This results in an additional 450 fiber functions to account for the white matter anisotropy, for a total of 23 358 unknowns. In comparison, the symmetric BEM solution has 12 648 unknowns and the linear anisotropic FEM solution contains 394 807 unknowns. The relative errors are displayed in Figure 3.11b. Once more, the comparison with the symmetric BEM highlights how standard surface modeling, which omits the fiber and volume integral equations results in important errors (around 20 %). In contrast, the hybrid formulation exhibits less than 5 % relative error up to very high source eccentricity, performing slightly better than the completely volumetric FEM solution. This experiment confirms the ability of the proposed formulation to overcome the model approximations of a standard BEM approach.

Overall, these tests on canonical structures illustrate the flexibility of the hybrid solver in dealing with the different kinds of anisotropy in the human head. This is achieved by exploiting the structured geometry of the inhomogeneous domains, leading to a much more efficient discretization than full volume-based methods.

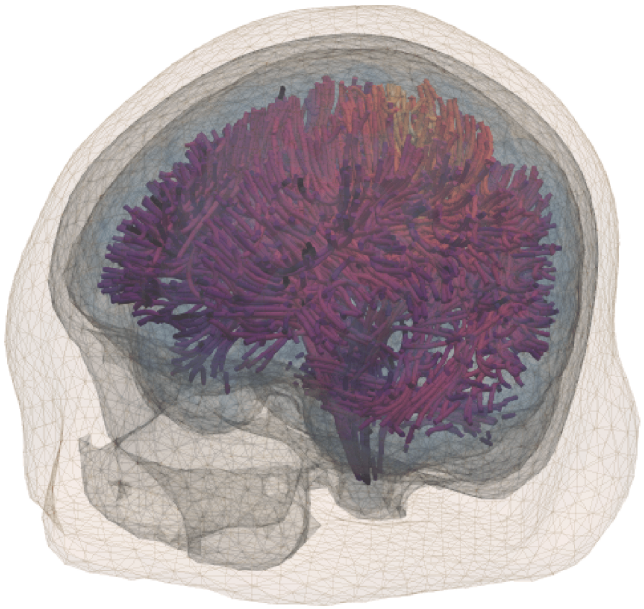

Figure 3.12: Complete mesh geometry with tractography-generated white matter fibers.

3.7.2 Validation of the White Matter Conductivity Model

The hybrid solver is also applied on a realistic head model derived from the MRI of a single subject from the Wu-Minn Human Connectome Project database [121] to highlight its applicability. Surface and volume meshes were obtained after preprocessing [48], segmentation and tessellation [116] of the structural MRI data. The different head compartments were assigned commonly used conductivity values [73]. The soft bone thickness of the skull is defined as an affine function of the local skull thickness. A probabilistic tractography algorithm [117] was applied on the subject's dMRI data to generate a bundle of non-connected streamlines, which was subsequently clustered [47] to obtain a fiber map of the white matter. The subject-specific model is illustrated in Figure 3.12.

The fiber radius was adjusted to match a white matter volume of $450\,\mathrm{cm}^3$. We applied the procedure described in Section 3.6 with the anisotropic longitudinal and transversal conductivities reported in [85] and obtained the homogenized brain conductivity tensor

$$\overline{\overline{\sigma}}_e = \begin{bmatrix} 0.1755 & 0 & 0 \\ 0 & 0.1915 & 0 \\ 0 & 0 & 0.1855 \end{bmatrix}. \tag{3.98}$$

These values are fairly close to the isotropic brain conductivity $\sigma_{brain} = 0.18\ \mathrm{S\,m^{-1}}$ [73], and thus confirm that our fiber conductivity model is consistent with the

conductivity values reported in literature.

3.7.3 Comparison with a Realistic FEM Model

The comparison of the proposed technique with another numerical method is difficult as anisotropy is either not considered or modeled differently. As explained in Section 3.3.3, a state-of-the-art anisotropic FEM solution would consist in discretizing the full volume of the head and, for each element in the white matter, assign a conductivity tensor derived with the help of DTI data. The hybrid solver, however, takes advantage of the fact that the white matter is considered anisotropic along some fiber pathways tracked by tractography and thus only requires the discretization of one-dimensional fibers, a structure which is quite different from the fully tetrahedral FEM mesh.

Considering these constraints, we followed a specific protocol to obtain comparable hybrid and state-of-the-art anisotropic solutions in a realistic setting. The meshing sequence obtained after preprocessing provides volume (tetrahedral) meshes of the different head tissues and matching surface (triangular) meshes of their boundaries. Each tissue is assigned a commonly used conductivity value [73], as summarized in Table 3.1. The skull anisotropy is modeled following (3.10), with the soft bone fraction t_s defined as an affine function of the local skull thickness. Furthermore, a white matter mask was extracted from the dMRI data. Then, for each voxel in a 1.25 mm isotropic grid and within the mask, the diffusion tensor was computed via a least-square fit. The conductivity tensor on each voxel in the white matter was finally obtained by following a mean conductivity volume constraint [103]. This protocol ensures that although the hybrid and FEM solvers are based on different numerical methods, and in particular different ways of modeling the white matter anisotropy, the discretized models have approximately the same conductivity profiles. The surface potential, skull and white matter currents obtained with the hybrid method are illustrated in Figure 3.13.

Figure 3.14 displays the difference between the hybrid and the anisotropic FEM models. The cortical surface is made of 24991 vertices, and for each dipolar source placed on a vertex and oriented normally to the surface, this difference is computed as the relative error of the electric potential obtained on a standardized set of 76 electrodes. The electrodes and cortex structure are depicted in Figure 3.15.

Table 3.1: Conductivity values used in the isotropic and anisotropic models.

	Brain	WM lon.	WM tra.	Skull	Hard bone	Soft bone	Scalp
σ ($\mathrm{S\,m^{-1}}$)	0.18	1.13	0.13	0.01	0.0064	0.02685	0.43

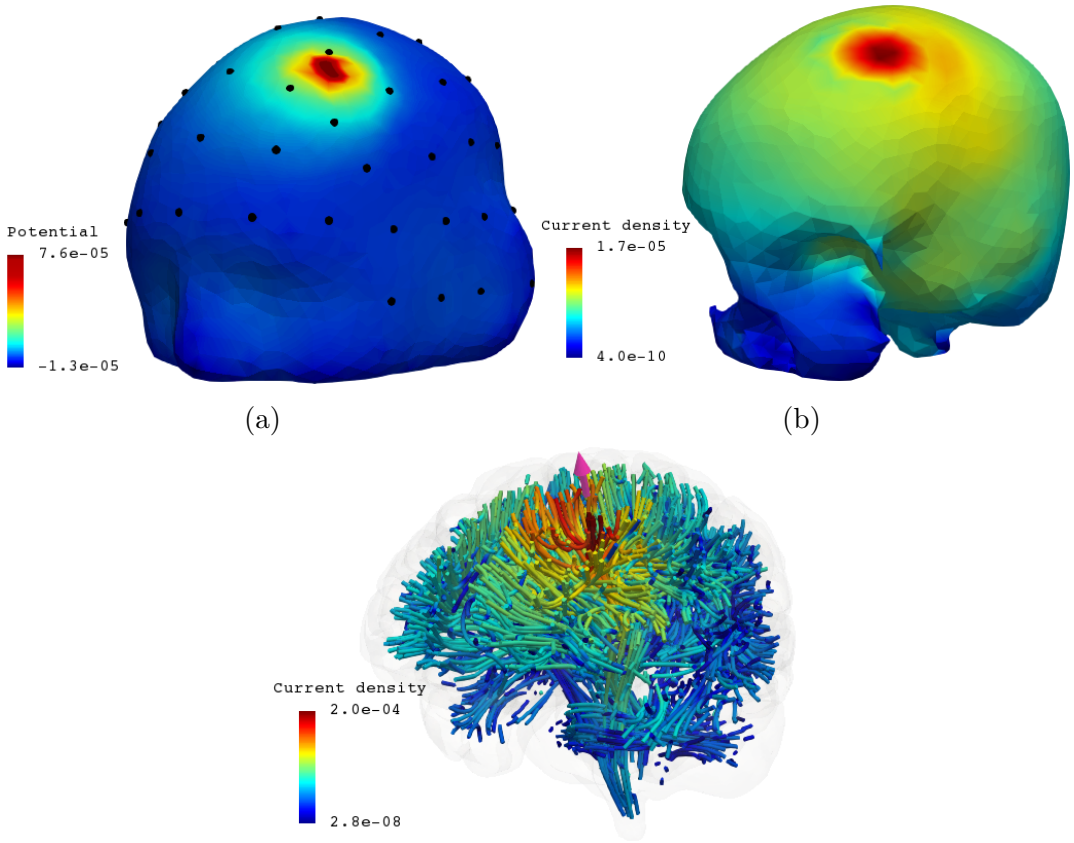

Figure 3.13: (a) Scalp surface potential, (b) skull volume currents, and (c) fiber currents computed with the hybrid formulation. The arrow in (c) represents the cortical dipole and the black dots in (a) indicate the electrode positions.

The effect of anisotropy modeling is highlighted with two other commonly employed metrics, the Relative Difference Measure (RDM) and the logarithmic magnitude difference measure (lnMAG) [52], which are displayed on the cortex in Figure 3.16 and Figure 3.17. The RDM map indicates that the deeper the sources the more dissimilar the scalp topographies. This is expected, as deep sources are more likely to be surrounded by fibers than shallow sources, and thus are more affected by the anisotropy. The lnMAG map shows how isotropic conductivity values are a compromise that cannot be optimal for all sources. Overall, the potential produced by shallow sources have too low of an amplitude whereas that of deep sources is too high. Therefore, by using a different homogenized conductivity, we would decrease the relative difference for some sources but also increase it for others.

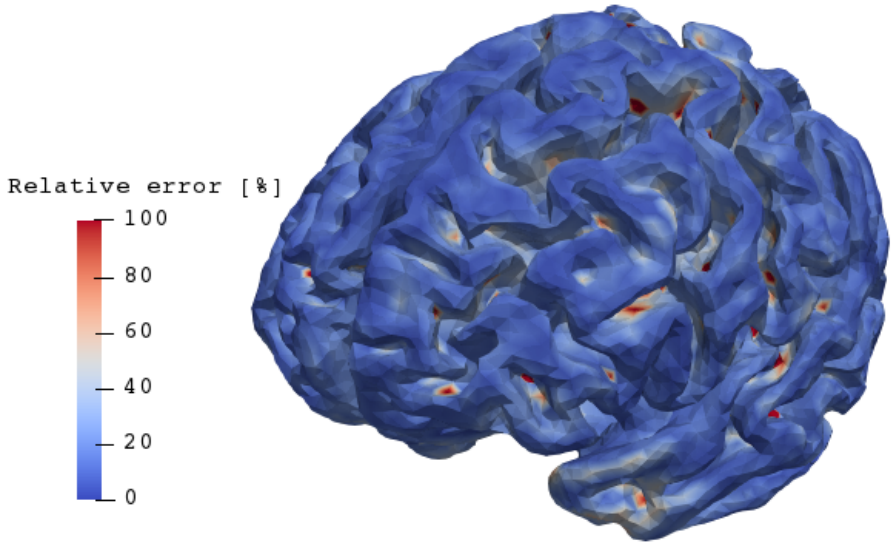

Figure 3.14: Cortex map of the relative error between the anisotropic FEM and hybrid solver.

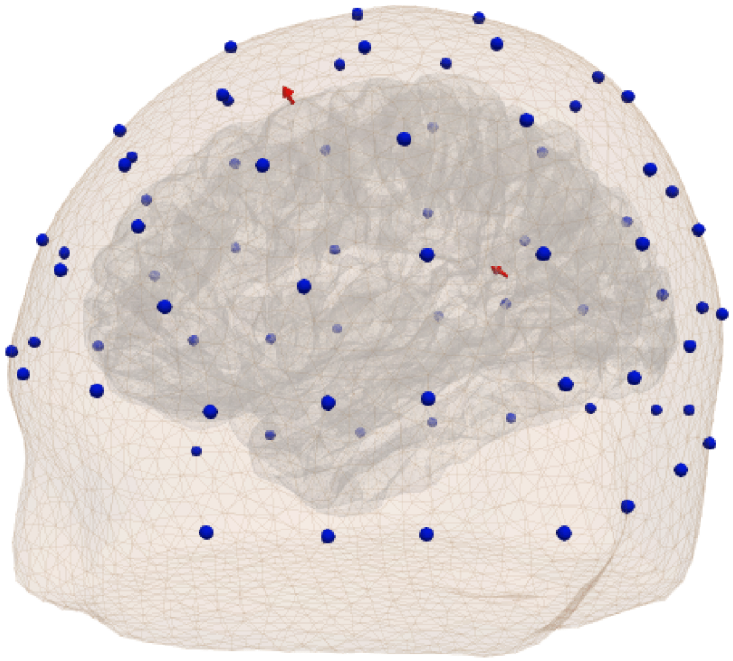

Figure 3.15: Electrodes (blue dots) and example dipoles (red arrows) overlaid on top of the scalp and cortex meshes, respectively.

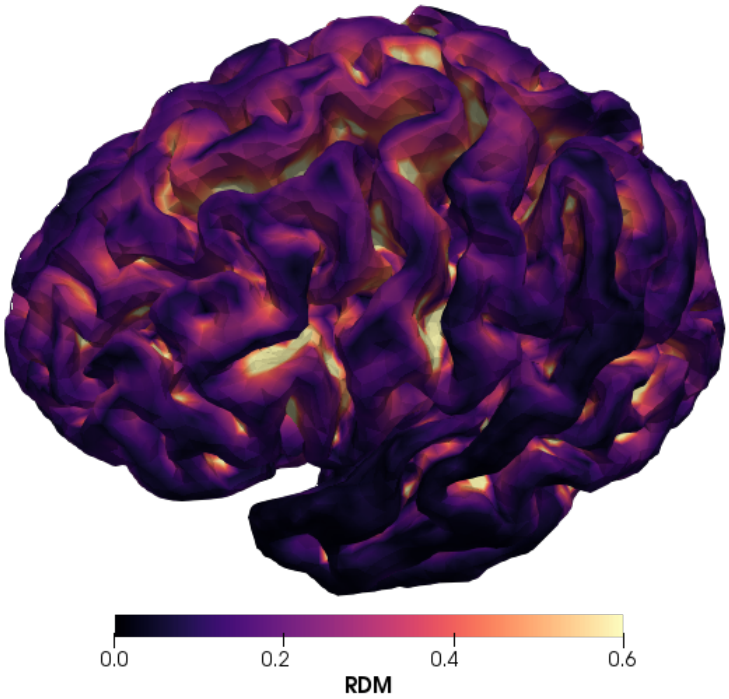

Figure 3.16: Cortex map of the Relative Difference Magnitude between piecewise isotropic and anisotropic head volume.

The topographic and magnitude changes between the two numerical methods and the different conductivity models are further illustrated in Figure 3.18 which displays the scalp potential generated by a deep and a shallow source (red arrows in Figure 3.15). We can also appreciate how the hybrid and FEM curves have the same shape for the shallow source and how their difference lies mainly in amplitude, while the deep source produces a more dissimilar scalp map. Both numerical methods produce almost identical solutions in the piecewise isotropic case, and remain in relatively good agreement in the other case despite the fact that they use intrinsically different models of anisotropy. Overall, this numerical experiment confirms that the proposed multimodal MRI-based hybrid integral method is consistent with a DTI volume-based anisotropic model of white matter despite their intrinsic modeling differences.

3.8 Conclusion

In this chapter we have presented a new solution to the anisotropic EEG forward problem that does not require a full volumetric discretization of the head. The standard boundary integral formulation was coupled with thin volume and wire integral equations that adequately match the non-uniform conductivities of the

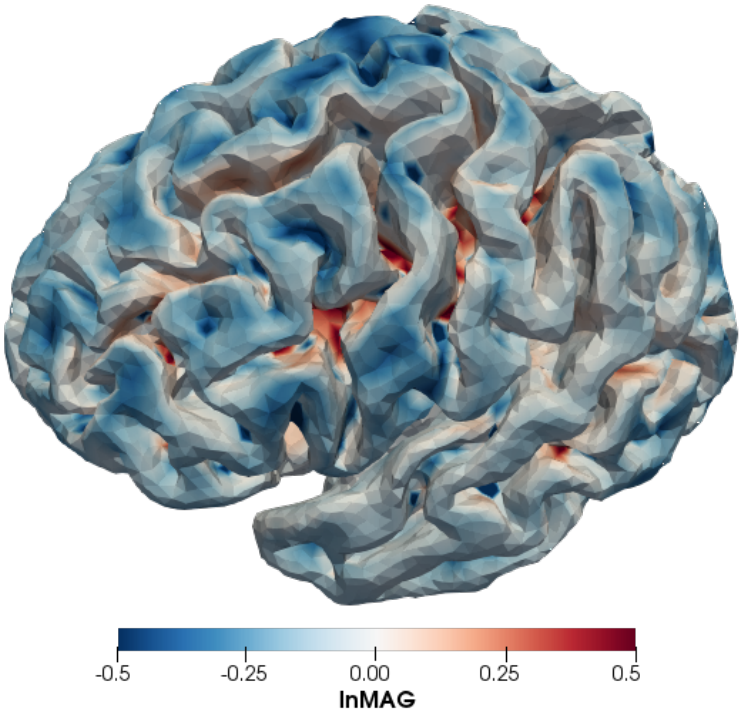

Figure 3.17: Cortex map of the logarithmic magnitude difference between piecewise isotropic and anisotropic head volume.

skull and white matter, respectively. The accuracy and flexibility of this BEM-like and anisotropy-handling formulation was demonstrated on a canonical model. A realistic scenario illustrated its applicability in a clinical environment, in which the patient-specific physiological properties were derived from multimodal biomedical imaging techniques.

Additionally, like the classical BEM, the $\mathcal{O}(N^2)$ asymptotic complexity in matrix building and storage of the proposed integral equation method can furthermore be reduced to linear complexity with fast solvers [13, 72]. This, combined with the tailored discretization strategy, would result in a highly efficient solver. The asymptotic acceleration of integral equation methods is studied in the next chapter.

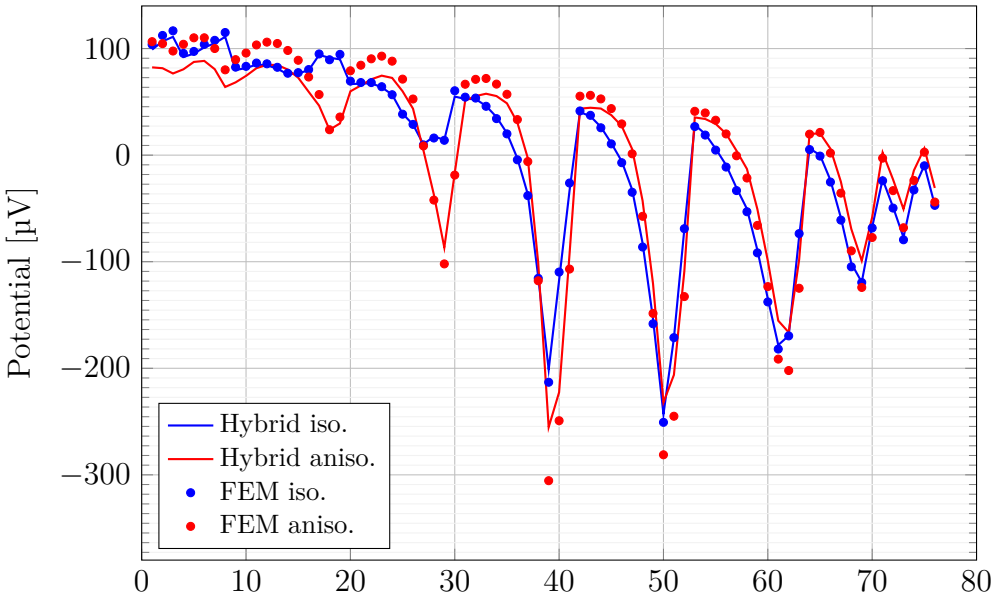

(a)

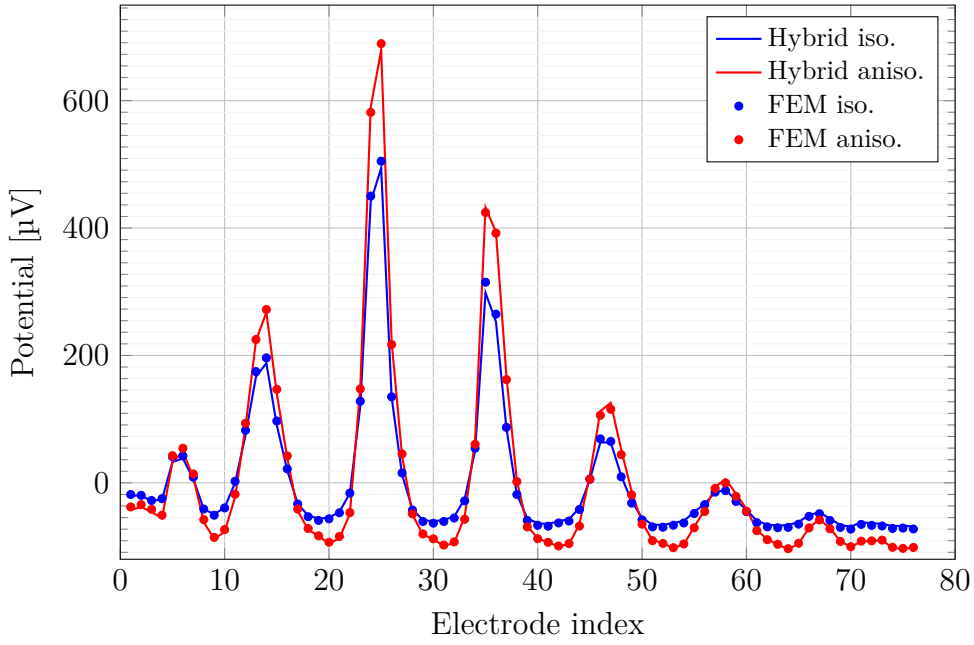

(b)

Figure 3.18: Scalp electrode potential resulting from (a) a deep and (b) a shallow source obtained from solving the EEG forward problem with the hybrid integral method (continuous lines) and FEM (dots) and with isotropic (blue) and anisotropic (red) conductivity assumptions.

Chapter 4

A Fast Electromagnetic Solver for EEG Modeling

The core advantage of Boundary Element Method (BEM) solvers for the forward problem of Electroencephalography (EEG) lies in the fact that the dimension of the unknown space is reduced by one compared to solvers based on differential equations like the Finite Element Method (FEM). Traditionally, the BEM has been used for small objects or low-resolution geometries, which would result in a few thousand unknowns N. Thus, matrix filling, storage and inversion could all be done on a portable machine in a moderate time and computational effort without the need for acceleration techniques. Technological progress in structural brain imaging now allows for very precise, high resolution models of the human head and better discriminability of its different tissues and their boundaries [120]. For instance, the brain compartment, classically modeled as homogeneous, can be further divided into white matter, gray matter and cerebrospinal fluid domains, each having a distinct conductivity [124]. The inclusion of more head tissues at a higher resolution, as well as the modeling of inhomogeneity and anisotropy with strategies such as those developed in the previous chapter inevitably increase the number of unknowns. However, without specific treatment, standard BEM solvers are unable to exploit this increase in modeling accuracy. Indeed, due to the non-local nature of the involved operators, the discrete BEM systems are full, meaning that matrix filling and storage grow in $\mathcal{O}(N^2)$ and a full matrix inversion in $\mathcal{O}(N^3)$ complexity.

Fortunately, these complexities can be drastically reduced with the help of fast solver techniques, such as the Adaptive Cross Approximation (ACA) [13], Multilevel Fast Multipole Method (MLFMM) [113], Adapted Integral Method (AIM) [17], and Multilevel Matrix Decomposition Algorithm (MLMDA) [78]. Fundamentally, all these methods exploit the fact that while the matrix of the system to be solved is in general full rank, there are submatrices which are compressible, i.e. they can be replaced by low-rank approximants that require less memory than the original

entries and allow for a faster matrix-vector multiplication.

Although well-established in the high-frequency electromagnetic community [29], fast solver techniques are quite uncommon in the field of EEG [67, 59]. Therefore, in the following, we explain the principle of matrix compressibility which ultimately allows for efficient linear or almost linear integral equation-based solvers, then develop a new acceleration technique for the construction of computational head models. Finally, numerical experiments demonstrate its performance and practical advantages in EEG forward modeling.

4.1 Low-Rank Approximation

The concept of matrix compression is related to its rank and determines the number of operations required to perform a matrix-vector multiplication. The solution of a discrete system $\mathbf{A}\boldsymbol{x} = \boldsymbol{b}$, where $\mathbf{A}$ is a square matrix resulting from the discretization of N linearly independent equations, can be obtained with a complexity $\mathcal{O}(N_{iter}N_{mvp})$ per right-hand side $\boldsymbol{b}$, where N_{mvp} is the computational cost of a matrix-vector product and N_{iter} is the number of iterations when using Krylov subspace iterative solvers, such as the Conjugate Gradient Squared method (CGS) [114] or the Generalized Minimal Residual method (GMRES) [104]. Therefore, a fast matrix-vector product is of particular interest because the solution of the problem can subsequently be obtained in low complexity.

4.1.1 Fast Matrix-Vector Multiplication for Rank-Deficient Matrices

Let us first consider the $N \times N$ matrix of ones

$$\mathbf{M_1} = \begin{bmatrix} 1 & \dots & 1 \\ \vdots & \ddots & \vdots \\ 1 & \dots & 1 \end{bmatrix} . \tag{4.1}$$

Naively, the dense product with a vector $\boldsymbol{v}$ costs $\mathcal{O}(N)$ operations per row (N multiplications and $N-1$ additions). Given that there are N rows, the complexity of the matrix-vector product is then $\mathcal{O}(N^2)$. However, denoting $\boldsymbol{v_1}$ the size N vector of ones, we notice that $\mathbf{M_1} = \boldsymbol{v_1}\boldsymbol{v_1}^T$ so that the matrix-vector product $\boldsymbol{b} = \mathbf{M_1}\boldsymbol{v}$ can be performed in two steps as

$$a = \boldsymbol{v_1}^T\boldsymbol{v} \,, \tag{4.2a}$$

$$\boldsymbol{b} = \boldsymbol{v_1} a \,. \tag{4.2b}$$

Each step costs $\mathcal{O}(N)$ operations, so the matrix-vector product can be performed in linear complexity in this case. The interpretation is that despite being of size

$N \times N$, no matter the value of N, $\mathbf{M_1}$ has a constant rank equal to 1, that is, it can be described with a single vector $\boldsymbol{v_1}$ and thus the matrix-vector product is reduced to two products with a row vector (4.2a) and with a column vector (4.2b).

The previous observation can be used to derive the complexity of the matrix-vector product for an $N \times N$ matrix $\mathbf{M}$ of rank k. The singular value decomposition (SVD) of $\mathbf{M}$ reads

$$\mathbf{M} = \mathbf{U}\boldsymbol{\Sigma}\mathbf{V}^T \,, \tag{4.3}$$

where $\mathbf{U} = [\boldsymbol{u}_1 \dots \boldsymbol{u}_N]$ and $\mathbf{V} = [\boldsymbol{v}_1 \dots \boldsymbol{v}_N]$ are orthogonal matrices and $\boldsymbol{\Sigma}$ is a diagonal matrix that contains the k non-zero singular values $\sigma_1 \geq \sigma_2 \geq \cdots \geq \sigma_k > 0$. The matrix-vector product can then be written as the sum of k rank-1 matrix-vector products

$$\mathbf{M}\boldsymbol{v} = \sum_{l=1}^{k} \sigma_l \boldsymbol{u}_l (\boldsymbol{v}_l^T \boldsymbol{v}) \,, \tag{4.4}$$

which costs $\mathcal{O}(kN)$ operations. Therefore, as long as k is small, the matrix-vector multiplication has a linear complexity.

This result can further be generalized to matrices that are full-rank but for which the singular values decay fast. Given a tolerance ϵ, if there exists a low-rank matrix $\widetilde{\mathbf{M}}$ that satisfies

$$\frac{\|\mathbf{M} - \widetilde{\mathbf{M}}\|_2}{\|\mathbf{M}\|_2} \leq \epsilon \,, \tag{4.5}$$

where $\|\cdot\|_2$ denotes the matrix spectral norm, then the full-rank matrix-vector product $\mathbf{M}\boldsymbol{v}$ can be approximated by the low-rank matrix-vector product $\widetilde{\mathbf{M}}\boldsymbol{v}$. In fact, if we compute the SVD of $\mathbf{M}$ and choose k such that

$$\sigma_{k-1} > \epsilon\sigma_1 > \sigma_k \,, \tag{4.6}$$

then the matrix

$$\mathbf{M}_k = \mathbf{U}_k \boldsymbol{\Sigma}_k \mathbf{V}_k^T \,, \tag{4.7}$$

where

$$\mathbf{U}_k = \mathbf{U}_{:,1:k} \,, \quad \mathbf{V}_k = \mathbf{V}_{:,1:k} \,, \quad \boldsymbol{\Sigma}_k = \boldsymbol{\Sigma}_{1:k,1:k} \,, \tag{4.8}$$

is the best rank-k approximation of $\mathbf{M}$ satisfying (4.5) [14]. In that sense, the SVD of a matrix provides an optimal indicator of its compressibility. Therefore, the full-rank, but rank-k compressible matrix $\mathbf{M}$ which contains N^2 elements can be economically represented as

$$\mathbf{M} \approx \mathbf{A}\mathbf{B}^T \tag{4.9}$$

using two $N \times k$ matrices $\mathbf{A} = \mathbf{U}_k\boldsymbol{\Sigma}_k$ and $\mathbf{B} = \mathbf{V}_k$. The total storage requirement is $2kN$ elements and the multiplication by a vector is done in $\mathcal{O}(kN)$ operations. Therefore, if k is independent from N, which is the case for Calderón-Zygmund [35] operators such as those used in this work, these complexities are linear with respect to N.

4.1.2 Example Case

To illustrate the previous concept, let us consider the static single-layer operator matrix $\mathbf{S}$ whose entries are

$$\mathbf{S}_{ij} = \frac{1}{4\pi} \int_\Gamma f_i(\boldsymbol{r}) \int_\Gamma \frac{1}{\|\boldsymbol{r} - \boldsymbol{r}'\|} f_j(\boldsymbol{r}') \, \mathrm{d}S' \mathrm{d}S \,, \tag{4.10}$$

where Γ is the surface of a sphere, discretized with $N = 1110$ unknowns, and f_k is the piecewise constant basis function defined on the k^{th} triangle of the discretized geometry. This operator matrix appears for instance in the symmetric BEM formulation.

Since the static Green's function G, which constitutes the kernel of $\mathbf{S}$, is asymptotically smooth [19], it can be shown that any submatrix of $\mathbf{S}$ corresponding to the interactions between spatially well-separated subsets of basis functions has an exponentially decaying spectrum [13]. Following the reasoning of the previous section, such property implies that it can be approximated by a low-rank matrix for a fixed approximation threshold, independently of the number of basis functions inside the well-separated subsets.

To visualize the compressibility of $\mathbf{S}$, we compute its SVD of and plot the normalized singular values in decreasing order. Figure 4.1 displays the first 300 singular values, and we can observe that the spectrum (blue curve) decays quite slowly. With a tolerance of $\epsilon = 10^{-3}$ (purple curve), not even a single value can be truncated since in this example, $\sigma_N > \epsilon\sigma_1$.

However, if we restrict ourselves to a 300×300 submatrix of $\mathbf{S}$ representing well-separated off-diagonal interactions, the corresponding SVD in Figure 4.1 (yellow curve) is much more compressible. It could in fact be approximated by a matrix of rank 10 only. Consequently, using (4.9), this off-diagonal block can be represented with two rectangular matrices of size 300×10. This yields a compression rate of

$$1 - \frac{300 \times 10 \times 2}{300 \times 300} \approx 93\% \,. \tag{4.11}$$

Not all submatrices are as compressible. Notably, the red curve in Figure 4.1 shows the singular values of the 300×300 diagonal submatrix corresponding to the same testing elements. We see that the spectrum decays almost as slowly as the full operator matrix. Therefore, this example shows that compressibility depends on the spatial discriminability of the interactions. Indeed, the distance from a given testing element to a faraway source element is almost the same as that to another source element near the first source element, as illustrated in Figure 4.2. We see that $d_{f1} \approx d_{f2}$, so that the interactions of the testing triangle (in black) with the far source triangles (in blue) will be similar. This observation does not hold for near triangles (in orange), but since there are only few ($\mathcal{O}(1)$) near source elements for each testing element, the set of near interactions for the whole matrix comprises only $\mathcal{O}(N)$ entries.

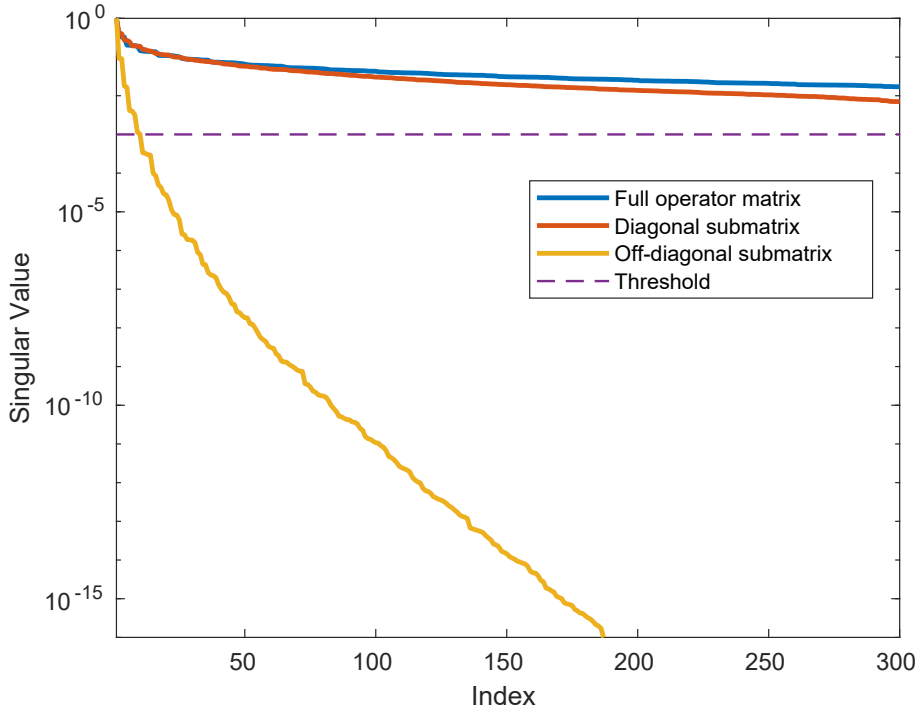

Figure 4.1: Singular value decompositions of the static single-layer operator matrix, a diagonal submatrix and an off-diagonal submatrix.

This encourages us to treat the various groups of interactions differently. Some of them, the off-diagonal blocks, can be economically approximated by low-rank matrices, while the rest (the diagonal blocks) needs to be computed accurately. The latter blocks, which represent self and neighbor interactions, should not be compressed, but fortunately account for only $\mathcal{O}(N)$ interactions. Overall, this yields a representation that would be much more efficient than the original full matrix, both in terms of storage and matrix-vector product complexity. Formally, we want to decompose any operator matrix $\mathbf{Z}$ to be compressed into

$$\mathbf{Z} \approx \mathbf{Z}_{near} + \widetilde{\mathbf{Z}}_{far} \,, \tag{4.12}$$

where $\mathbf{Z}_{near}$ is an uncompressible diagonal matrix that is sparse (thus contains only $\mathcal{O}(N)$ non-zero elements) and the approximation $\widetilde{\mathbf{Z}}_{far}$ is a compressed representation of the remainder, which represents all the far interactions.

Being far is of course relative and depends on the proximity of the source elements. In particular, on a discretized geometry, the distance of neighbor cells is defined by the cell size, which is constant for a uniform mesh. An efficient discrimination between near and far interactions can be obtained via an octree decomposition, that provides a multilevel, or hierarchical, partition of the mesh.

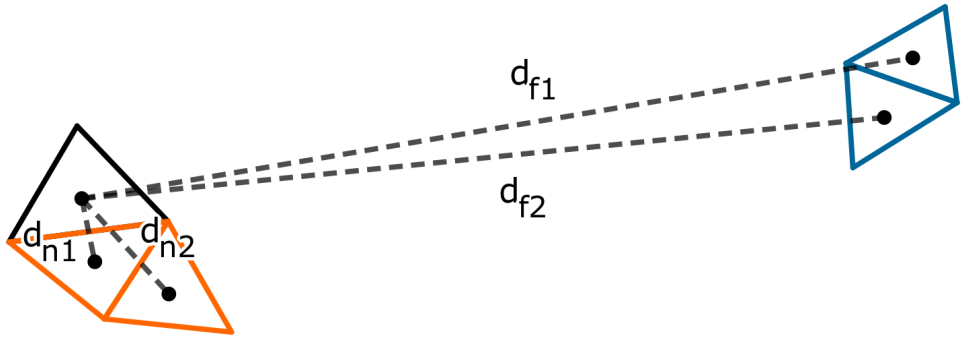

Figure 4.2: Distances between near and far mesh elements. The black triangle represents a testing element, interacting with near and far source triangles in orange and blue, respectively.

4.2 Hierarchical Matrix Decomposition

4.2.1 Octree Partitioning

Each basis function corresponds to an interacting element of the system matrix. Given the mesh of the geometry under consideration, the basis functions are each represented by a single point at the barycenter of the cell(s) defining their support. The set of points is denoted $I = \{i_0, \ldots, i_{N-1}\}$. An octree is a multilevel hierarchical partition of the set of points. We define the parameter n_{max} as the maximum number of points within a leaf box. The first level ($l = 0$) of the octree B consists in a cubic box b_0^0 that contains all the points. The octree is then recursively defined as follows: if any box at level l contains more than n_{max} points, then each non-empty box b_i^l of that level is subdivided into 8 children boxes $b_j^{l+1}, \ldots, b_{j+7}^{l+1}$ (where j boxes have already been constructed at level $l+1$) that have half the side length of the parent box b_i^l. This subdivision process is repeated until the deepest boxes all contain at most n_{max} points. Boxes without children are called leaf boxes. The diameter of a box is the distance between two opposite corners, and represents the maximum distance between any two points within the box. The octree partitioning is illustrated in Figure 4.3. It is worth mentioning that the union of the boxes at any level l form a partition of the entire set of basis functions.

An alternative parametrization to n_{max} consists in setting instead the minimum box size e_{L-1}, i.e. the edge length of the boxes at the deepest level $L-1$. If the mesh is almost uniform and e_{L-1} is chosen proportional to the mesh element size h, the maximum number of elements per box remains bounded. The number of levels L is then determined by doubling the box size until the entire geometry is contained in a single box (the root). Once the root is determined, the subdivision process is applied iteratively for all non-empty boxes until the last level.

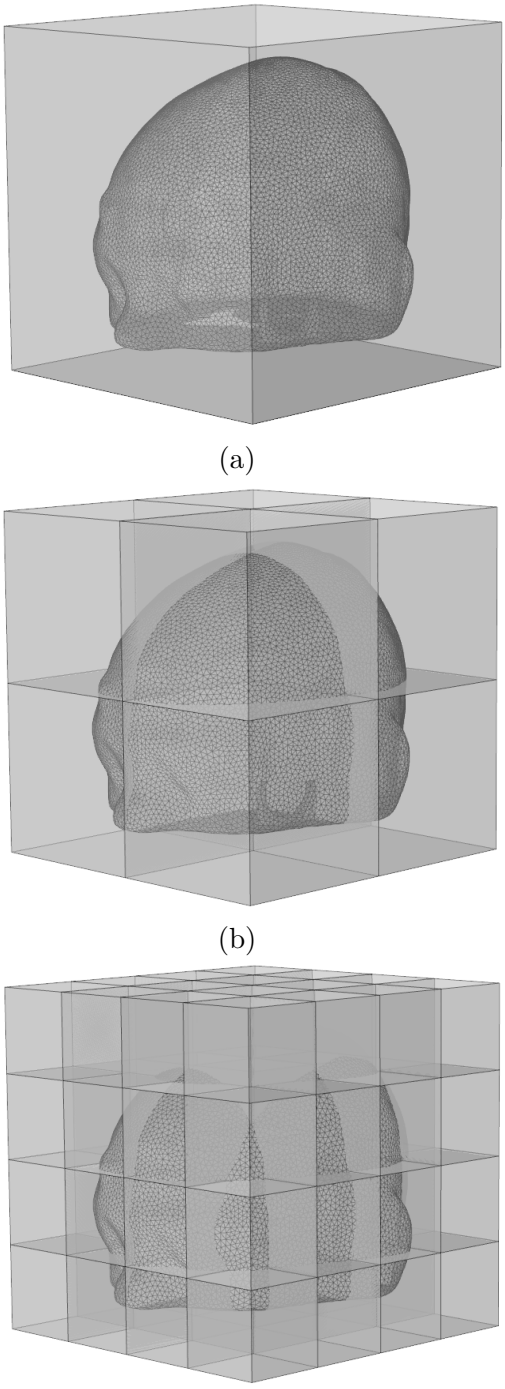

(a)

(b)

(c)

Figure 4.3: Geometrical representation of the octree decomposition of a head model at (a) level 0, (b) level 1 and (c) level 2.

Algorithm 1: Construction of the block cluster tree

```
Input  : testing octree B_T, source octree B_S
Output: block cluster tree T_{B_T × B_S}
initialization: close boxes of r_{B_T} ← {r_{B_S}};
for level l do
    for testing box t do
        for source box s close to t do
            if 4.13 then
                create compressible block β^l_{t×s};
            else if t or s is leaf then
                create non compressible block β̄^l_{t×s};
            else
                for child box t' do
                    for child box s' do
                        add s' to the list of close boxes of t';
                    end
                end
            end
        end
    end
end
```

4.2.2 Block Cluster Partitioning

Since an octree B represents a partition of the set of elements, the set of interactions can itself be partitioned with a so-called block cluster tree $T_{B\times B}$ whose elements are pairs of testing and source boxes from B. This is equivalent to partitioning the operator matrix into submatrices. If we consider different sets of basis functions for the testing and source discretizations, one octree must be defined for each set. For simplicity, we assume here that B applies to both testing and source functions. We define the following admissibility criterion: two boxes t, s from B with centers $\boldsymbol{c}_t, \boldsymbol{c}_s$ and diameters d_t, d_s form an admissible block if

$$\eta \left\| \boldsymbol{c}_t - \boldsymbol{c}_s \right\| > \max(d_t, d_s)\,, \tag{4.13}$$

where $\eta > 0$ is the admissibility parameter. When $\eta = 1$, we see that two boxes are admissible if they do not touch, i.e. there is at least one box between them. Thus, the admissibility condition defines a relative discrimination rule between near field and far field interactions.

A level-consistent block cluster tree $T_{B\times B}$ is then constructed recursively starting from the root according to Algorithm 1. Level-consistent means that boxes

interact only with boxes of the same level. The idea behind the construction of the block cluster tree is relatively intuitive. If two clusters of testing and source elements are admissible, they can economically be represented in a compressed block β. Otherwise, the submatrix associated to the corresponding interactions is a diagonal or near-diagonal block, and if at least one of the two clusters is a leaf, it is represented as a non-compressed block $\bar{\beta}$. Finally, if neither condition is satisfied, the boxes are subdivided and the decision is delayed to the next level.

In particular, a compressible block is created if and only if (a) the boxes are admissible and (b) their parents are not. Therefore, compressible interactions are compressed at the lowest possible level (closest to the root), which ensures that the compression is done between as big clusters as possible. This concept is illustrated in Figure 4.4. By construction, and since B is a partition of the set of basis functions, all of the interactions in the operator matrix are partitioned into either compressible or full blocks. In the next section, we describe an algorithm which performs the block compression in almost linear complexity.

4.3 Fast Matrix Compression

We saw previously that an $m \times n$ matrix block $\mathbf{M}$ deemed compressible by the block cluster tree is optimally approximated by the rank-k product

$$\mathbf{M} \approx \mathbf{A}\mathbf{B}^T , \tag{4.14}$$

where the $m \times k$ matrix $\mathbf{A} = \mathbf{U}_k\mathbf{\Sigma}_k$ and $n \times k$ matrix $\mathbf{B} = \mathbf{V}_k$ are computed from the truncated SVD of $\mathbf{M}$ [14]. However, the SVD itself is computationally expensive. Its complexity is $\mathcal{O}(m^2 n)$, the same as the full matrix inversion (if $m = n$). It also requires the computation of all the elements in $\mathbf{M}$, which makes it impractical. Therefore, instead of the SVD, we use the ACA [14], which is an efficient algorithm for the compression of low-rank matrices. Other popular fast solver techniques such as the MLFMM require an expansion of the kernel and therefore necessitate a complete reimplementation effort. In contrast, the ACA is purely algebraic in the sense that it does not require a specific treatment depending on the kernel of the operator matrix. As such, when applicable, it can be conveniently seen as a black-box algorithm to be applied on top of an existing non-accelerated electromagnetic solver.

The ACA algorithm, described in Algorithm 2, works intuitively by sequentially computing a set of rows and columns of the original matrix. If the residual error (in Frobenius norm) estimated at the end of each iteration is higher than the prescribed ACA tolerance, the algorithm finds new pivots to determine a new row and column to be added to the previously computed ones. In other words, the rank of the approximant is gradually incremented at each iteration until convergence. In the extreme case where the number of iterations reaches the dimension of the

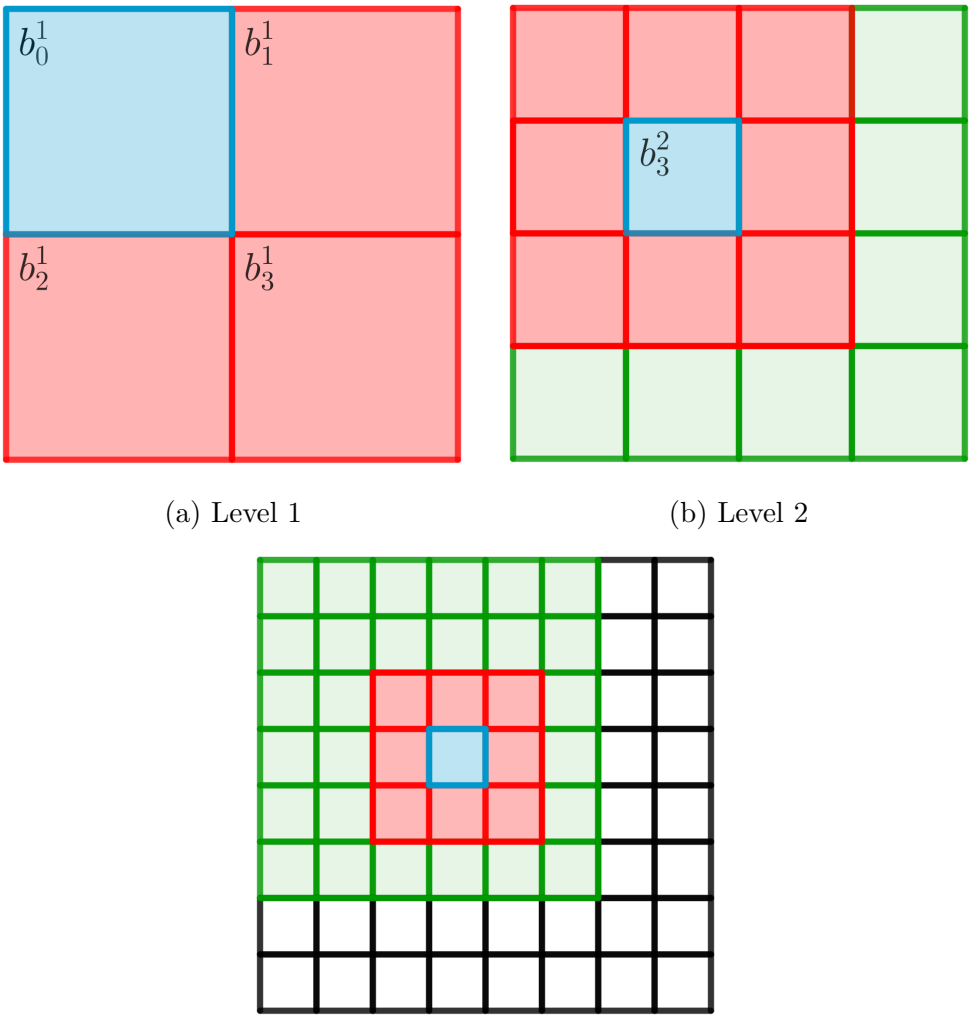

(a) Level 1

(b) Level 2

(c) Level 3

Figure 4.4: Block admissibility at different levels of a quadtree, the 2D version of an octree. Blue boxes represent testing boxes, green and red boxes represent admissible and non-admissible source boxes, respectively. Uncolored boxes indicate that the corresponding block interactions are already treated at a parent level.

block, i.e. $k = \min(m, n)$, the block has been computed entirely. However, the admissibility criterion (4.13) ensures that blocks deemed compressible are spatially well-separated, thus guaranteeing the exponential decay of the approximation error as the rank increases for matrices generated by an asymptotically smooth kernel [14]. Therefore, for a fixed accuracy ϵ, k remains constant and much lower than m or n as the mesh resolution increases The rank-k ACA approximation of the block

Algorithm 2: Adaptive Cross Approximation

Input : tolerance ϵ
Output: low-rank approximant $\widetilde{\mathbf{M}} = \mathbf{UV} = \mathbf{C}\mathbf{R}_k^{-1}\mathbf{L}_k^{-1}\mathbf{R}$
initialization: set $i_k = 1$, $I_{sel} = \{i_k\}$, $J_{sel} = \{\,\}$, $\|\widetilde{\mathbf{M}}\|^2 = 0$,
$\mathbf{C}, \mathbf{R}, \mathbf{U}, \mathbf{V} = \mathbf{0}, \mathbf{L}_k^{-1}, \mathbf{R}_k^{-1} = [\,]$;
for $k \leftarrow 1$ **to** $\min(m, n)$ **do**
  $\boldsymbol{v}_k \leftarrow \mathbf{M}(i_k, :)$;
  $\mathbf{R}(k, :) \leftarrow \boldsymbol{v}_k$;
  $\boldsymbol{v}_k \leftarrow \boldsymbol{v}_k - \mathbf{U}(i_k, 1 : k-1)\mathbf{V}(1 : k-1, :)$;
  $j_k \leftarrow \max_{j \notin J_{sel}}(|\boldsymbol{v}_k|)$;
  $J_{sel} \leftarrow J_{sel} \cup j_k$;
  if $\boldsymbol{v}_k(j_k) \neq 0$ **then**
    $\boldsymbol{v}_k \leftarrow \boldsymbol{v}_k / \boldsymbol{v}_k(j_k)$;
  end
  $\mathbf{V}(k, :) \leftarrow \boldsymbol{v}_k$;
  $\boldsymbol{u}_k \leftarrow \mathbf{M}(:, j_k)$;
  $\mathbf{C}(:, k) \leftarrow \boldsymbol{u}_k$;
  $\boldsymbol{u}_k \leftarrow \boldsymbol{u}_k - \mathbf{V}(1 : k-1, j_k)\mathbf{U}(: , 1 : k-1)$;
  $\mathbf{U}(:, k) \leftarrow \boldsymbol{u}_k$;
  $d_k \leftarrow \mathbf{M}(i_k, j_k) - \mathbf{U}(i_k, 1 : k-1)\mathbf{V}(1 : k-1, j_k)$;
  $\mathbf{L}_k^{-1} \leftarrow \begin{bmatrix} \mathbf{L}_k^{-1} & \mathbf{0} \\ -\frac{1}{d_k}\mathbf{U}(i_k, 1 : k-1)\mathbf{L}_k^{-1} & \frac{1}{d_k} \end{bmatrix}$;
  $\mathbf{R}_k^{-1} \leftarrow \begin{bmatrix} \mathbf{R}_k^{-1} & -\mathbf{R}_k^{-1}\mathbf{V}(1 : k-1, j_k) \\ \mathbf{0} & 1 \end{bmatrix}$;
  $\|\widetilde{\mathbf{M}}\|^2 \leftarrow \|\widetilde{\mathbf{M}}\|^2 + \|\boldsymbol{u}_k\|^2\|\boldsymbol{v}_k\|^2 + 2\sum_{l=1}^{k-1} |\boldsymbol{u}_l^T\boldsymbol{u}_k||\boldsymbol{v}_l^T\boldsymbol{v}_k|$;
  if $\|\boldsymbol{u}_k\|\|\boldsymbol{v}_k\| < \epsilon\|\widetilde{\mathbf{M}}\|$ **then**
    break;
  end
  $i_k \leftarrow \max_{i \notin I_{sel}}(|\boldsymbol{u}_k|)$;
  $I_{sel} \leftarrow I_{sel} \cup i_k$;
end

is then

$$\widetilde{\mathbf{M}} = \mathbf{U}\mathbf{V}^T \tag{4.15a}$$
$$= \mathbf{C}\mathbf{M}_k^{-1}\mathbf{R}\,, \tag{4.15b}$$

where $\mathbf{C}$ (resp. $\mathbf{R}$) contains k columns (resp. rows) of $\mathbf{M}$ selected by the ACA and

$$\mathbf{M}_k = \mathbf{L}_k\mathbf{R}_k \tag{4.16}$$

is the $k \times k$ matrix of the entries of $\mathbf{M}$ at the intersection of $\mathbf{C}$ and $\mathbf{R}$. It should be noted that in practice, the expression (4.15a) is used and the computation of $\mathbf{C}$, $\mathbf{R}$, $\mathbf{L}_k^{-1}$ and $\mathbf{R}_k^{-1}$ can be entirely skipped, although the alternative form (4.15b) directly exhibits the fact that only k rows and columns need to be computed.

In the following, we call the $m \times k$ matrix $\mathbf{U}$ the column matrix, since it is built from a linear combination of the k columns selected by the ACA. Similarly the $k \times n$ matrix $\mathbf{V}^T$ is called the row matrix. Contrary to the SVD, the ACA requires to compute only a few entries of the original matrix. In fact, assuming that k is bounded across all compressible blocks of the operator, the total storage requirement is of complexity $\mathcal{O}(N \log N)$. The matrix-vector product is then performed by going through all the blocks and summing the block-vector products. Therefore, the complexity of the matrix-vector product is also $\mathcal{O}(N \log N)$.

4.4 QR-SVD Matrix Recompression

The ACA algorithm provides a compressed representation of a matrix by storing only a few rows and columns. However, the resulting row matrix $\mathbf{V}^T$ and column matrix $\mathbf{U}$ are not orthogonal in general. Therefore, they could themselves be orthogonalized to be represented even more efficiently. This process is called recompression, i.e. it is an additional compression performed on the compressed matrices. Observing that $\mathbf{U}$ and $\mathbf{V}$ have a dimension k independent from the matrix dimensions $m \times n$, it is possible to orthogonalize the matrices without compromising the asymptotic complexity of the fast solver.

First, a QR decomposition is performed on the column matrix as

$$\mathbf{U} = \mathbf{Q}_\mathbf{U}\mathbf{R}_\mathbf{U}\,, \tag{4.17}$$

where $\mathbf{Q}_\mathbf{U}$ is an $m \times k$ orthogonal matrix and $\mathbf{R}_\mathbf{U}$ is a square upper triangular matrix. This operation can be performed in $\mathcal{O}(k^2 m)$ complexity [22]. Similarly, the row matrix is decomposed in $\mathcal{O}(k^2 n)$ complexity as

$$\mathbf{V} = \mathbf{Q}_\mathbf{V}\mathbf{R}_\mathbf{V}\,. \tag{4.18}$$

The compressed block thus takes the form

$$\widetilde{\mathbf{M}} = \mathbf{U}\mathbf{V}^T = \mathbf{Q}_\mathbf{U}\mathbf{R}_\mathbf{U}\mathbf{R}_\mathbf{V}{}^T\mathbf{Q}_\mathbf{V}{}^T\,. \tag{4.19}$$

Since the middle block $\mathbf{R}_\mathbf{U}\mathbf{R}_\mathbf{V}{}^T$ is of size $k \times k$, we can compute its SVD in $\mathcal{O}(k^3)$ complexity, which, importantly, does not depend on the original matrix dimensions. This yields

$$\mathbf{R}_\mathbf{U}\mathbf{R}_\mathbf{V}{}^T = \mathbf{U}_S\mathbf{\Sigma}_S\mathbf{V}_S^T\,. \tag{4.20}$$

Then, similarly as described in Section 4.1.1, only $k' \leq k$ rows and columns of the SVD can be selected, according to

$$\sigma_{k'} \geq \epsilon'\sigma_1 > \sigma_{k'+1}\,, \tag{4.21}$$

where σ_i are the singular values in the diagonal matrix $\mathbf{\Sigma}_S$ and ϵ' is an arbitrarily defined recompression threshold. The matrix $\mathbf{M}$ is therefore economically represented as the rank-k' approximant

$$\widetilde{\mathbf{M}} = \mathbf{U'V'}^T \,, \tag{4.22}$$

where the recompressed $m \times k'$ column matrix $\mathbf{U'}$ and $n \times k'$ row matrix $\mathbf{V'^T}$ read

$$\mathbf{U'} = \mathbf{Q_U} \mathbf{U}_{S,k'} \mathbf{\Sigma}_{k'} \tag{4.23}$$

$$\mathbf{V'} = \mathbf{Q_V} \mathbf{V}_{S,k'} \,, \tag{4.24}$$

where $\mathbf{U}_{S,k'}$, $\mathbf{\Sigma}_{k'}$ and $\mathbf{V}_{S,k'}$ are the truncated matrices of the SVD. The recompression process has an overall computational complexity of $\mathcal{O}(k^2(m+n))$ which is of the same order as the ACA. It can be performed immediately after the ACA compression of a matrix block, thereby storing the $m \times n$ matrix with $k'(m+n)$ entries only. Since the QR-SVD is performed on the ACA product $\mathbf{UV}^T$, this process will not improve the error with respect to the actual matrix $\mathbf{M}$ in general, but at least provides an optimal representation of the approximation while maintaining the computational complexity of the ACA.

4.5 Compression of the Green's Function

4.5.1 Sparse Transformation Matrix Representation

Until this point, the interactions have always been considered between basis functions. While this seems logical given that the operator matrix entry $\mathbf{Z}_{ij}$ corresponds to the interaction between the i^{th} testing basis function and the j^{th} source basis function, it is also possible to consider more elementary interactions. Notably, the interaction between basis functions that span several cells (which is the case for piecewise linear functions and SWG functions) can be computed as the sum of the interactions between the basis functions restricted to each cell, i.e.

$$\begin{aligned}
\mathbf{Z}_{ij} &= \int_\Gamma f_i(\boldsymbol{r}) \int_\Gamma K(\boldsymbol{r}, \boldsymbol{r'}) f_j(\boldsymbol{r'}) \,\mathrm{d}S' \mathrm{d}S \\
&= \sum_{c_i} \sum_{c_j} \int_{c_i} \int_{c_j} f_i|_{c_i}(\boldsymbol{r}) K(\boldsymbol{r}, \boldsymbol{r'}) f_j|_{c_j}(\boldsymbol{r'}) \,\mathrm{d}S' \mathrm{d}S \\
&= \sum_{c_i} \sum_{c_j} \mathbf{Z^c}_{c_i c_j} \,,
\end{aligned} \tag{4.25}$$

where Γ is the discretized domain, K is the kernel of the operator, f_i is a basis function with the cells c_i as its support, and $\mathbf{Z^c}$ is an operator made of cell interactions. Furthermore, since in the far field, integrals are computed numerically via a

double Gaussian quadrature rule, the interactions in a compressible far field block can be rewritten as

$$\mathbf{Z}_{ij} = \sum_{c_i} \sum_{c_j} a_{c_i} a_{c_j} \sum_{p \in c_i} \sum_{q \in c_j} w_p f_i(\boldsymbol{r}_p) K(\boldsymbol{r}_p, \boldsymbol{r}'_q) w_q f_j(\boldsymbol{r}'_q)\,, \tag{4.26}$$

where $\boldsymbol{r}_p$ (resp. $\boldsymbol{r}_q$) is a quadrature point on cell c_i (resp. c_j), a_{c_i} and a_{c_j} are the areas of the cells and w_p and w_q are normalized Gaussian weights. This shows that far field interactions between basis functions effectively boil down to the evaluation of the kernel on the set of all quadrature points. Contrary to the set I of basis function barycenters introduced in Section 4.2.1, quadrature points do not represent basis functions supported on one or more cells. This means that in general, an octree and a block cluster tree built upon the quadrature point interactions can be defined independently from basis function or cell size considerations. We therefore introduce the transformation matrix $\mathbf{\Theta}$ mapping the j^{th} cell to the i^{th} basis function

$$(\mathbf{\Theta})_{ij} = \begin{cases} 1 & \text{if } c_j \text{ belongs to the support of } f_i \\ 0 & \text{otherwise}\,, \end{cases} \tag{4.27}$$

as well as the transformation matrix $\mathbf{\Xi}$ mapping the j^{th} quadrature point to the i^{th} cell

$$(\mathbf{\Xi})_{ij} = \begin{cases} a_{c_j} w_j f_i(\boldsymbol{r}_j) & \text{if } \boldsymbol{r}_j \text{ belongs to } c_i \\ 0 & \text{otherwise}\,. \end{cases} \tag{4.28}$$

Additionally, we also introduce the kernel matrix of the quadrature points

$$(\mathbf{K})_{ij} = \begin{cases} K(\boldsymbol{r}_i, \boldsymbol{r}_j) & \text{if } i \neq j \\ 0 & \text{otherwise}\,. \end{cases} \tag{4.29}$$

Like $\mathbf{Z}$, if the kernel function K is asymptotically smooth, the kernel matrix $\mathbf{K}$ can also be compressed blockwise for submatrices corresponding to well-separated group of interactions [14]. We thus decompose it as $\mathbf{K} = \mathbf{K}_{near} + \mathbf{K}_{far}$, where $\mathbf{K}_{far}$ contains all the interactions that are used in double quadrature integrals to compute $\mathbf{Z}$ as in (4.26). The operator matrix $\mathbf{Z}$ then reads

$$\begin{aligned} \mathbf{Z} &= \mathbf{Z}_{near} + \mathbf{Z}_{far} \\ &= \mathbf{Z}_{near} + \mathbf{\Theta}\mathbf{\Xi}\mathbf{K}_{far}\mathbf{\Xi}^T\mathbf{\Theta}^T\,. \end{aligned} \tag{4.30}$$

While the point interaction matrix $\mathbf{K}_{far}$ is based on an octree partition of the quadrature points, the near field is still computed in a cell-based or basis function-based manner to avoid singularities and ensure accurate evaluation of the matrix entries. This inhomogeneity in the treatment of the near versus far field means that $\mathbf{Z}_{near}$ and $\mathbf{Z}_{far}$ may not be complementary sets anymore. To illustrate this, consider

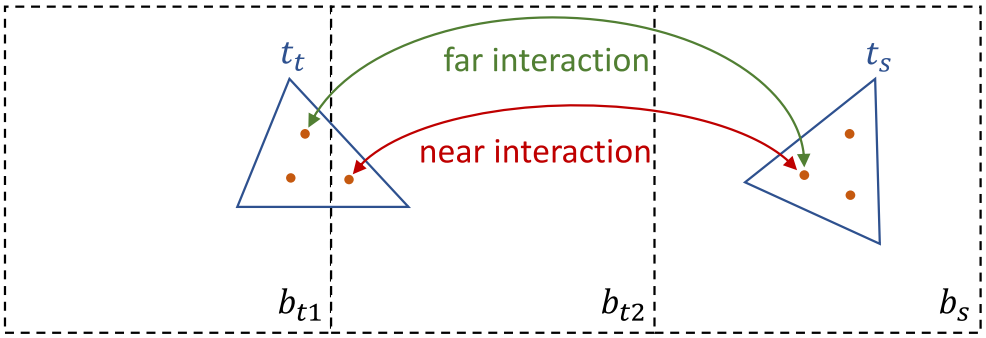

Figure 4.5: Example of a cell split between two octree boxes. Without treatment, part of the interaction between the two triangle cells is computed in both near and far blocks.

for instance that for a q-point quadrature rule, the quadrature points of a testing cell t_t are split into two neighbor boxes b_{t1} and b_{t2} by the octree decomposition. Given a source box that is adjacent to b_{t2} but not b_{t1} and contains a source cell t_s as shown in Figure 4.5, the former will form a near field interaction while the latter represents a far field interaction. As a result, the cell interaction between the two triangles is fully computed once in $\mathbf{Z}_{near}$ but also partly in $\mathbf{Z}_{far}$ due to the points located in b_{t1}. This redundancy is alleviated by imposing that all quadrature points within a cell must belong to the same leaf box during the octree decomposition. This can be achieved by associating all the quadrature points to their respective cell center, which does not compromise the octree partitioning as long as $q < n_{max}$.

Alternatively, it is possible to employ instead a correction scheme similar in principle to the one used in the pre-corrected Fast Fourier Transform (FFT) [97]. This is achieved by subtracting the double quadrature integrals from the accurate analytical or semi-analytical integrals in $\mathbf{Z}_{near}$ to remove the inaccurate contributions from the uncompressed blocks in $\mathbf{K}$.

Owing to the fact that they contain local information, $\mathbf{\Xi}$ and $\mathbf{\Theta}$ are sparse. Therefore, they can be multiplied with a vector in $\mathcal{O}(N)$ operations which, assuming that $\mathbf{K}_{far}$ has been compressed, do not increase the asymptotic complexity of the overall matrix-vector product. In this form, originally introduced in [4], the non-separable part of the interaction is isolated into the matrix of quadrature point interactions $\mathbf{K}$. Compressing $\mathbf{K}_{far}$ instead of $\mathbf{Z}_{far}$ has several advantages:

- the computation of matrix entries is very fast since it boils down to the simple evaluation of the Green's function, and no integral is involved;
- the compressibility is possibly higher from factoring out the contribution of the basis functions;
- other parameters (e.g. a material scaling) are also factored out.

This appears quite advantageous for hybrid formulations with volume and/or wire unknowns such as the one presented in the previous chapter. Because operator-specific parameters are excluded from $\mathbf{K}$, a compressed approximation $\widetilde{\mathbf{K}}$ of the low-level point matrix can be used for several operator matrices that share the same kernel function K. Beyond hybrid formulations, this versatility may be highly beneficial in a wider range of methods. For instance, it could allow for a single compression of both single-layer and hypersingular operator matrices in symmetric formulations, or a single compression of the scalar and the vector potential in the Electric Field Integral Equation (EFIE) for antenna analysis and scattering problems. In this work, this property is leveraged in two ways: to compress matrices with different discretizations in the next section, as well as to compress matrices with different material scalings in Chapter 5.

Beyond the fact that preprocessing becomes somewhat more involved, a caveat of using a point compression is that it is sensitive to cancelling integrals between different cells, as explained later in this chapter. This motivates the development in Section 4.5.4 of an appropriate cure which does not compromise the asymptotic complexity.

Another drawback of a point compression is that the dimension of the matrix to be compressed is multiplied by the number of quadrature points per cell. In practice, since compressible blocks correspond to far field interactions, a limited amount of points per cell is sufficiently accurate and therefore does not drastically increase the dimensionality of the problem.

4.5.2 Compression of Multiple Operators

The hybrid formulation introduced in Chapter 3 contains several types of unknowns (wire, surface and volume), leading to an overall system matrix that is made of several operator matrix blocks (one for each combination of basis functions). Since each block operator has a distinct kernel, scaling and/or set of testing and source functions, the standard approach [15, 93] with the ACA is to perform one compression for each block, e.g. if the overall system matrix $\mathbf{Z}$ takes the form

$$\mathbf{Z} = \begin{bmatrix} \mathbf{A} & \mathbf{B} \\ \mathbf{C} & \mathbf{D} \end{bmatrix} , \tag{4.31}$$

then the fast matrix-vector multiplication $\boldsymbol{v} = \mathbf{Z}\boldsymbol{x}$ is performed as

$$\begin{aligned}
\boldsymbol{v} &= \mathbf{Z}\boldsymbol{x} \\
&= \begin{bmatrix} \mathbf{A} & \mathbf{B} \\ \mathbf{C} & \mathbf{D} \end{bmatrix} \begin{bmatrix} \boldsymbol{x}_1 \\ \boldsymbol{x}_2 \end{bmatrix} \\
&= \begin{bmatrix} \mathbf{A}\boldsymbol{x}_1 + \mathbf{B}\boldsymbol{x}_2 \\ \mathbf{C}\boldsymbol{x}_1 + \mathbf{D}\boldsymbol{x}_2 \end{bmatrix} \\
&\approx \begin{bmatrix} \mathbf{A}_{near}\boldsymbol{x}_1 + \mathbf{B}_{near}\boldsymbol{x}_2 \\ \mathbf{C}_{near}\boldsymbol{x}_1 + \mathbf{D}_{near}\boldsymbol{x}_2 \end{bmatrix} + \begin{bmatrix} \widetilde{\mathbf{A}}_{far}\boldsymbol{x}_1 + \widetilde{\mathbf{B}}_{far}\boldsymbol{x}_2 \\ \widetilde{\mathbf{C}}_{far}\boldsymbol{x}_1 + \widetilde{\mathbf{D}}_{far}\boldsymbol{x}_2 \end{bmatrix},
\end{aligned} \tag{4.32}$$

where $\mathbf{A}_{near}$, $\mathbf{B}_{near}$, $\mathbf{C}_{near}$, $\mathbf{D}_{near}$ are the uncompressed blocks representing the near field interactions, and $\widetilde{\mathbf{A}}_{far}$, $\widetilde{\mathbf{B}}_{far}$, $\widetilde{\mathbf{C}}_{far}$, $\widetilde{\mathbf{D}}_{far}$ are the individual compressions of each block. Indeed, the inhomogeneous matrix $\mathbf{Z}$ as a whole is not in general asymptotically smooth and therefore the exponential decay of singular values is not guaranteed. Notably, for the hybrid formulation, the surface tested blocks are potential equations while the others are current equations. While this naturally incites us to compress each block individually, this unfortunately introduces some redundancy when we consider the fact that the support of the different types of basis functions may overlap. For instance, in the hybrid formulation, part of the surface basis functions are defined on the boundary of the volume basis functions. Therefore, instead of compressing the blocks independently, it would be interesting to cluster and compress together different elements when they are geometrically close. In this context, the proposed point-based compression of the Green's function presented in the previous section is perfectly suitable since, up to differences in the kernel function itself, factoring out basis function and scaling contributions makes the inner system matrix homogeneous.

From the hybrid system matrix given in (3.64), it appears that the block operator matrices with the same testing functions have the same kernel. Indeed, there is a double-layer kernel $\nabla_n G$ when the rows correspond to pyramid testing functions, and a single-layer kernel G otherwise. Therefore, a fast matrix-vector product for the overall system matrix can be obtained with only two compressions, one for each kernel.

For simplicity, in the following, we restrict our analysis to two types of basis functions (surface pyramids and SWG functions) and neglect the wire anisotropy, although the extension to this case is straightforward. We denote:

- q_{tet} the set of quadrature points belonging to the tetrahedra volume;
- q_f the set of quadrature points belonging to the tetrahedra faces, i.e. their boundaries;
- q_{tri} the set of quadrature points belonging to the triangles, i.e. those that belong to the surface mesh delimiting the background conductivity jumps.

Three octrees are then built:

- B_v, which partitions the SWG quadrature points $q_{swg} = q_{tet} \cup q_f$;
- B_s, which partitions the pyramid quadrature points q_{tri};
- B_a, which partitions the complete set of all quadrature points $q_a = q_{swg} \cup q_{tri}$.

The block cluster trees are finally obtained from the octrees:

- $T_{B_s \times B_a}$, which partitions the interactions with surface testing;
- $T_{B_v \times B_a}$, which partitions the interactions with volume testing.

We can see that there are only two block cluster trees compared to the four that would be required with a standard ACA. The point interactions of each block cluster tree are compressed via the ACA algorithm followed by a QR-SVD recompression to get the single- and adjoint double-layer compressions $\widetilde{\mathbf{S}}$ and $\widetilde{\mathbf{D}}^*$, respectively. The mapping matrices $\boldsymbol{\Theta}$ and $\boldsymbol{\Xi}$ from Section 4.5.1 must be adjusted to take into account the multiple types of basis functions, cells and quadrature points. We thus define:

- $\boldsymbol{\Xi}_{v,v}$, mapping the SWG quadrature points to the volume cells

$$(\boldsymbol{\Xi}_{v,v})_{ij} = \begin{cases} a_{c_j} w_j \nabla \cdot (\boldsymbol{v}_i(\boldsymbol{r}_j)) & \text{if } \boldsymbol{r}_j \in q_{swg} \text{ belongs to } c_i \\ 0 & \text{otherwise}\,, \end{cases} \tag{4.33}$$

- $\boldsymbol{\Xi}_{a,\chi v}$, mapping all quadrature points to the volume cells

$$(\boldsymbol{\Xi}_{a,\chi v})_{ij} = \begin{cases} {\sigma_i}^{-1} a_{c_j} w_j \nabla \cdot (\overline{\overline{\chi}} \boldsymbol{v}_i(\boldsymbol{r}_j)) & \text{if } \boldsymbol{r}_j \in q_a \text{ belongs to } c_i \\ 0 & \text{otherwise}\,, \end{cases} \tag{4.34}$$

- $\boldsymbol{\Xi}_{s,s}$, mapping the pyramid quadrature points to the surface cells

$$(\boldsymbol{\Xi}_{s,s})_{ij} = \begin{cases} a_{c_j} w_j s_i(\boldsymbol{r}_j) & \text{if } \boldsymbol{r}_j \in q_{tri} \text{ belongs to } c_i \\ 0 & \text{otherwise}\,, \end{cases} \tag{4.35}$$

- $\boldsymbol{\Xi}_{a,s}$, mapping all quadrature points to the surface cells

$$(\boldsymbol{\Xi}_{a,s})_{ij} = \begin{cases} (\sigma_l - \sigma_k) a_{c_j} w_j s_i(\boldsymbol{r}_j) & \text{if } \boldsymbol{r}_j \in q_a \text{ belongs to } c_i \in \Gamma_{kl} \\ 0 & \text{otherwise}\,, \end{cases} \tag{4.36}$$

where s_i and $\boldsymbol{v}_i$ are pyramid and SWG basis functions, respectively. Similarly as in (4.27), we also define three sparse cell to basis function mapping matrices for:

- the SWG functions $\mathbf{\Theta}_v$;
- the anisotropic SWG functions $\mathbf{\Theta}_{\chi v}$;
- the pyramid functions $\mathbf{\Theta}_s$.

The matrix entries are equal to 1 when the relevant cell (tetrahedron or triangle) belongs to the support of the corresponding basis function. A distinct mapping $\mathbf{\Theta}_{\chi v}$ is needed for anisotropic SWG functions, i.e. SWG functions that are scaled by an anisotropic constrast $\overline{\overline{\chi}}$, because contrary to isotropic SWG functions, they are possibly non-zero on all the faces making up the boundary of the SWG tetrahedra instead of only the defining face. Note also that cell-wise scalings (e.g. σ_i^{-1} or $\sigma_l - \sigma_k$) can alternatively be placed on the $\mathbf{\Theta}$ matrices rather than the $\mathbf{\Xi}$ matrices.

Finally, the four non-local operator matrices $\mathbf{D}^*_{\mathbf{ss}}$, $\mathbf{D}^*_{\mathbf{sv}}$, $\mathbf{S}_{\mathbf{vs}}$ and $\mathbf{S}_{\mathbf{vv}}$ are obtained via

$$\mathbf{D}^*_{\mathbf{ss}} \approx \mathbf{D}^*_{\mathbf{ss}near} + \mathbf{\Theta}_{\mathbf{s}} \mathbf{\Xi}_{s,s} \widetilde{\mathbf{D}}^* \mathbf{\Xi}^T_{a,s} {\mathbf{\Theta}_{\mathbf{s}}}^T \tag{4.37}$$

$$\mathbf{D}^*_{\mathbf{sv}} \approx \mathbf{D}^*_{\mathbf{sv}near} + \mathbf{\Theta}_{\mathbf{s}} \mathbf{\Xi}_{s,s} \widetilde{\mathbf{D}}^* \mathbf{\Xi}^T_{a,\chi v} {\mathbf{\Theta}_{\boldsymbol{\chi}\mathbf{v}}}^T \tag{4.38}$$

$$\mathbf{S}_{\mathbf{vs}} \approx \mathbf{S}_{\mathbf{vs}near} + \mathbf{\Theta}_{v} \mathbf{\Xi}_{v,v} \widetilde{\mathbf{S}} \mathbf{\Xi}^T_{a,s} {\mathbf{\Theta}_{\mathbf{s}}}^T \tag{4.39}$$

$$\mathbf{S}_{\mathbf{vv}} \approx \mathbf{S}_{\mathbf{vv}near} + \mathbf{\Theta}_{v} \mathbf{\Xi}_{v,v} \widetilde{\mathbf{S}} \mathbf{\Xi}^T_{a,\chi v} {\mathbf{\Theta}_{\boldsymbol{\chi}\mathbf{v}}}^T . \tag{4.40}$$

With this representation, the fast matrix-vector multiplication $\boldsymbol{v} = \mathbf{Z}\boldsymbol{x}$, where

$$\mathbf{Z} = \begin{bmatrix} \mathbf{G}_{\mathbf{ss}} - \mathbf{D}^*_{\mathbf{ss}} & \mathbf{G}_{\mathbf{sv}} - \mathbf{D}^*_{\mathbf{sv}} \\ -\mathbf{S}_{\mathbf{vs}} & \mathbf{G}_{\mathbf{vv}} + \mathbf{S}_{\mathbf{vv}} \end{bmatrix} , \tag{4.41}$$

and

$$\boldsymbol{x} = \begin{bmatrix} \boldsymbol{x}_s \\ \boldsymbol{x}_v \end{bmatrix} , \tag{4.42}$$

is performed with the following sequence of operations

- for the far field interactions:

$$\boldsymbol{x}^{(\mathbf{1})}_s = \mathbf{\Xi}^T_{a,s} ({\mathbf{\Theta}_{\mathbf{s}}}^T \boldsymbol{x}_s) \tag{4.43a}$$

$$\boldsymbol{x}^{(\mathbf{2}s)}_s = \mathbf{\Theta}_{\mathbf{s}} (\mathbf{\Xi}_{s,s} (\widetilde{\mathbf{D}}^* \boldsymbol{x}^{(\mathbf{1})}_s)) \tag{4.43b}$$

$$\boldsymbol{x}^{(\mathbf{2}v)}_s = \mathbf{\Theta}_{v} (\mathbf{\Xi}_{v,v} (\widetilde{\mathbf{S}} \boldsymbol{x}^{(\mathbf{1})}_s)) \tag{4.43c}$$

$$\boldsymbol{x}^{(\mathbf{1})}_v = \mathbf{\Xi}^T_{a,\chi v} ({\mathbf{\Theta}_{\boldsymbol{\chi}\mathbf{v}}}^T \boldsymbol{x}_v) \tag{4.44a}$$

$$\boldsymbol{x}^{(\mathbf{2}s)}_v = \mathbf{\Theta}_{\mathbf{s}} (\mathbf{\Xi}_{s,s} (\widetilde{\mathbf{D}}^* \boldsymbol{x}^{(\mathbf{1})}_v)) \tag{4.44b}$$

$$\boldsymbol{x}^{(\mathbf{2}v)}_v = \mathbf{\Theta}_{v} (\mathbf{\Xi}_{v,v} (\widetilde{\mathbf{S}} \boldsymbol{x}^{(\mathbf{1})}_v)) , \tag{4.44c}$$

- for the near field interactions:

$$\boldsymbol{x}_{near}^{(ss)} = (\mathbf{G_{ss}} - \mathbf{D}^{*}_{\mathbf{ss}near})\boldsymbol{x_s} \tag{4.45}$$
$$\boldsymbol{x}_{near}^{(sv)} = (\mathbf{G_{sv}} - \mathbf{D}^{*}_{\mathbf{sv}near})\boldsymbol{x_v} \tag{4.46}$$
$$\boldsymbol{x}_{near}^{(vs)} = \mathbf{S}_{\mathbf{vs}near}\boldsymbol{x_s} \tag{4.47}$$
$$\boldsymbol{x}_{near}^{(vv)} = (\mathbf{G_{vv}} + \mathbf{S}_{\mathbf{vv}near})\boldsymbol{x_v}\,, \tag{4.48}$$

- for the deflation (to set the resulting potential to zero-mean [26]), which is handled exactly as in the first example of Section 4.1.1:

$$\boldsymbol{x}_{defl} = \lambda \mathbf{1}(\mathbf{1}^T \boldsymbol{x_s})\,, \tag{4.49}$$

- combining everything:

$$\boldsymbol{v} = \begin{bmatrix} \boldsymbol{x}_{near}^{(ss)} - \boldsymbol{x}_{\boldsymbol{s}}^{(\boldsymbol{2s})} + \boldsymbol{x}_{near}^{(sv)} - \boldsymbol{x}_{\boldsymbol{v}}^{(\boldsymbol{2s})} + \boldsymbol{x}_{defl} \\ -\boldsymbol{x}_{near}^{(vs)} + \boldsymbol{x}_{\boldsymbol{s}}^{(\boldsymbol{2v})} + \boldsymbol{x}_{near}^{(vv)} + \boldsymbol{x}_{\boldsymbol{v}}^{(\boldsymbol{2v})} \end{bmatrix}\,. \tag{4.50}$$

All the operations in the matrix-vector product involve only $\mathcal{O}(N)$ sparse matrix-vector products and $\mathcal{O}(N \log N)$ compressed matrix-vector products, which leads to an overall complexity of $\mathcal{O}(N \log N)$. Furthermore, only two compressions, for the Green's function and its normal derivative, are needed to compute the full matrix system compression.

Although the low-level compression of the Green's function proves to be more versatile than a standard compression scheme at the basis function level, an important issue arises in the computation of the $\mathbf{S_{vv}}$ operator matrix. This problem actually holds for any formulation that requires a hypersingular operator. In the standard symmetric BEM setting (without fast solver), the hypersingular matrix $\mathbf{N}$ is computed from the entries of the single-layer matrix $\mathbf{S}$, as described e.g. in [66, Equation (29)]. This stems from a theorem demonstrated in [84]. Accordingly, if we wanted to accelerate the symmetric BEM with a point compression strategy, it would be desirable to use a single compressed matrix to get both $\widetilde{\mathbf{N}}$ and $\widetilde{\mathbf{S}}$.

Unfortunately, if we used the point compression scheme presented thus far with a reasonably low tolerance ϵ, we would end up with a completely wrong approximation matrix $\widetilde{\mathbf{S}}_{\mathbf{vv}}$ (or $\widetilde{\mathbf{N}}$ in the symmetric BEM). The reason for this high inaccuracy problem is the presence of integral cancellations, and it is explained and illustrated in the following.

4.5.3 Numerical Stability

Consider a pair of far interacting testing and source SWG functions $\boldsymbol{v}_i$ and $\boldsymbol{v}_j$, as illustrated in Figure 4.6, with $R = \|\boldsymbol{c}_j^+ - \boldsymbol{c}_i^+\|$. For the sake of simplicity, assume that

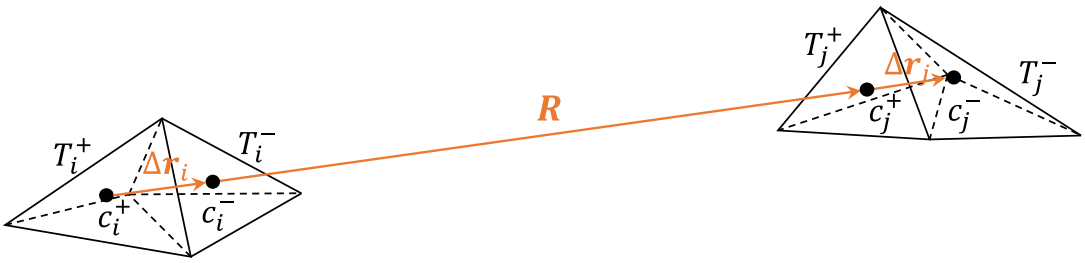

Figure 4.6: The tetrahedral support of a pair of interacting basis functions. The distance between two adjacent cell centers is proportional to the mesh parameter h, which is small compared to $R = \|\boldsymbol{R}\|$ for a far interaction.

the conductivity contrast is homogeneously equal to 1 in the tetrahedral supports $T_i^+ \cup T_i^-$ and $T_j^+ \cup T_j^-$. The general piecewise inhomogeneous and anisotropic case involves additional surface integrals on the tetrahedron faces but the underlying issue remains. From Section 3.4.2, the volume-volume interaction is

$$\begin{aligned}
(\mathbf{S_{vv}})_{ij} = & -\int_{T_i^+\cup T_i^-} \nabla\cdot\boldsymbol{v}_i(\boldsymbol{r}) \int_{T_j^+\cup T_j^-} G(\boldsymbol{r},\boldsymbol{r}')\nabla'\cdot\boldsymbol{v}_j(\boldsymbol{r}')\,\mathrm{d}V'\mathrm{d}V \\
= & -\frac{a_i a_j}{V_i^+ V_j^+}\int_{T_i^+}\int_{T_j^+} G(\boldsymbol{r},\boldsymbol{r}')\,\mathrm{d}V'\mathrm{d}V \\
& +\frac{a_i a_j}{V_i^+ V_j^-}\int_{T_i^+}\int_{T_j-} G(\boldsymbol{r},\boldsymbol{r}')\,\mathrm{d}V'\mathrm{d}V \\
& +\frac{a_i a_j}{V_i^- V_j^+}\int_{T_i^-}\int_{T_j+} G(\boldsymbol{r},\boldsymbol{r}')\,\mathrm{d}V'\mathrm{d}V \\
& -\frac{a_i a_j}{V_i^- V_j^-}\int_{T_i^-}\int_{T_j-} G(\boldsymbol{r},\boldsymbol{r}')\,\mathrm{d}V'\mathrm{d}V\,. \qquad (4.51)
\end{aligned}$$

The interaction is therefore the sum of four terms, two with positive signs and two with negative signs due to the fact that an SWG function points toward its defining face in its "+" tetrahedron and away from it in the "-" tetrahedron, as illustrated in Figure 3.6.

Since the two SWG functions are far from each other, all four double integrals have a similar value. To simplify the notation, in the following we consider far interaction integrals approximated with 1-point Gaussian quadrature integrals. We thus get

$$(\mathbf{S_{vv}})_{ij} = -a_i a_j \left(G(\boldsymbol{c}_i^+,\boldsymbol{c}_j^+) - G(\boldsymbol{c}_i^+,\boldsymbol{c}_j^-) - G(\boldsymbol{c}_i^-,\boldsymbol{c}_j^+) + G(\boldsymbol{c}_i^-,\boldsymbol{c}_j^-)\right)\,, \qquad (4.52)$$

where $\boldsymbol{c}_i^\pm$ (resp. $\boldsymbol{c}_j^\pm$) is the center of tetrahedron $T_i^\pm$ (resp. $T_j^\pm$). Using the notation in Figure 4.6, we then have $\|\Delta\boldsymbol{r}_i\| \approx \|\Delta\boldsymbol{r}_j\| \approx h \ll R$, where h is the mesh element size and $R = \|\boldsymbol{R}\|$. This implies that the four terms almost cancel each other in

the sum, resulting in a much smaller value than that of any of the individual terms. More explicitly, the first term in (4.52) reads

$$G(\boldsymbol{c}_i^+, \boldsymbol{c}_j^+) = \frac{1}{\|\boldsymbol{c}_i^+ - \boldsymbol{c}_j^+\|} = \frac{1}{R}\,. \tag{4.53}$$

A Taylor expansion of G in $(\boldsymbol{c}_i^+, \boldsymbol{c}_j^+)$ reveals for the second term that

$$\begin{aligned} G(\boldsymbol{c}_i^+, \boldsymbol{c}_j^-) &= \frac{1}{\|\boldsymbol{c}_i^+ - \boldsymbol{c}_j^+ + \boldsymbol{c}_j^+ - \boldsymbol{c}_j^-\|} \\ &= \frac{1}{\|R + \Delta\boldsymbol{r}_j\|} \\ &= \frac{1}{R} - \frac{\Delta\boldsymbol{r}_j \cdot \hat{\boldsymbol{r}}}{R^2} + \frac{3(\Delta\boldsymbol{r}_j \cdot \hat{\boldsymbol{r}})^2}{2R^3} - \frac{\|\Delta\boldsymbol{r}_j\|^2}{2R^3} + \mathcal{O}\left(\frac{h^3}{R^4}\right), \end{aligned} \tag{4.54}$$

where $\hat{\boldsymbol{r}} = \boldsymbol{R}/R$. Similarly for the last two terms, we get

$$G(\boldsymbol{c}_i^-, \boldsymbol{c}_j^+) = \frac{1}{R} - \frac{\Delta\boldsymbol{r}_i \cdot \hat{\boldsymbol{r}}}{R^2} + \frac{3(\Delta\boldsymbol{r}_i \cdot \hat{\boldsymbol{r}})^2}{2R^3} - \frac{\|\Delta\boldsymbol{r}_i\|^2}{2R^3} + \mathcal{O}\left(\frac{h^3}{R^4}\right) \tag{4.55}$$

$$G(\boldsymbol{c}_i^-, \boldsymbol{c}_j^-) = \frac{1}{R} - \frac{\Delta\boldsymbol{r}_{ij} \cdot \hat{\boldsymbol{r}}}{R^2} + \frac{3(\Delta\boldsymbol{r}_{ij} \cdot \hat{\boldsymbol{r}})^2}{2R^3} - \frac{\|\Delta\boldsymbol{r}_{ij}\|^2}{2R^3} + \mathcal{O}\left(\frac{h^3}{R^4}\right), \tag{4.56}$$

where $\Delta\boldsymbol{r}_{ij} = \Delta\boldsymbol{r}_i + \Delta\boldsymbol{r}_j$. Thus, summing all four terms in (4.52) results in

$$\begin{aligned} (\mathbf{S_{vv}})_{ij} &= -a_i a_j \left(3\frac{(\Delta\boldsymbol{r}_i \cdot \hat{\boldsymbol{r}})\,(\Delta\boldsymbol{r}_j \cdot \hat{\boldsymbol{r}})}{R^3} - \frac{\Delta\boldsymbol{r}_i \cdot \Delta\boldsymbol{r}_j}{R^3} + \mathcal{O}\left(\frac{h^3}{R^4}\right)\right) \\ &= \mathcal{O}\left(\frac{h^2}{R^3}\right). \end{aligned} \tag{4.57}$$

This means that, for a given mesh element size, the interaction between a pair of basis functions in $\mathbf{S_{vv}}$ is roughly proportional to $1/R^3$. This is to be contrasted with the individual point interactions in (4.52), that evaluate to the Green's function $G(\boldsymbol{r}, \boldsymbol{r}')$, and thus decrease comparatively slowly in $1/R$.

This difference in asymptotic scalings becomes an issue when put in the context of a compressing algorithm, for which the accuracy of the matrix entries is guaranteed only up to a given threshold. Indeed, consider that we compress the matrix of quadrature point interaction $\mathbf{K}$ (the kernel being the Green's function G) with a fixed tolerance ϵ. The entry-wise absolute error in $\tilde{\mathbf{K}}$ can be of order ϵ/R, which, past a certain distance R dominates the corresponding final matrix entries in $\mathbf{S_{vv}}$ that scale in $1/R^3$.

As a minimal example, assume that the block cluster tree decomposition of $\mathbf{K}$ contains an admissible block $\mathbf{K}_\beta$ which is exactly made of the two pairs of points in Figure 4.6, i.e. the testing points are $\boldsymbol{c}_i^+$ and $\boldsymbol{c}_i^-$ and the source points are $\boldsymbol{c}_j^+$ and $\boldsymbol{c}_j^-$.

The corresponding final matrix entry is $(\mathbf{S_{vv}})_{ij}$ as given in (4.52). For simplicity, the points are all aligned and we assume the equality $\Delta \boldsymbol{r}_i = -\Delta \boldsymbol{r}_j = h\hat{\boldsymbol{r}}$, so that we can write this block as

$$\mathbf{K}_\beta = \begin{bmatrix} G(\boldsymbol{c}_i^+, \boldsymbol{c}_j^+) & G(\boldsymbol{c}_i^+, \boldsymbol{c}_j^-) \\ G(\boldsymbol{c}_i^-, \boldsymbol{c}_j^+) & G(\boldsymbol{c}_i^-, \boldsymbol{c}_j^-) \end{bmatrix} = \begin{bmatrix} \dfrac{1}{R} & \dfrac{1}{R+h} \\ \dfrac{1}{R-h} & \dfrac{1}{R} \end{bmatrix} . \tag{4.58}$$

In that case, we have

$$(\mathbf{S_{vv}})_{ij} = \frac{2a_i a_j h^2}{R(R+h)(R-h)} , \tag{4.59}$$

which, as expected, scales in $1/R^3$. Furthermore, the equivalence of matrix norms ensures that for any $n \times n$ matrix $\mathbf{A}$ we have in particular the inequality [58]

$$\sqrt{n}\|\mathbf{A}\|_2 \geq \|\mathbf{A}\|_F , \tag{4.60}$$

where $\|\cdot\|_F$ denotes the Frobenius norm. Thus, the spectral norm of $\mathbf{K}_\beta$ is lower bounded by

$$\begin{aligned} \|\mathbf{K}_\beta\|_2 &\geq \frac{1}{\sqrt{2}}\|\mathbf{K}_\beta\|_F \\ &\geq \frac{1}{\sqrt{2}}\sqrt{\frac{1}{R^2} + \frac{1}{(R+h)^2} + \frac{1}{(R-h)^2} + \frac{1}{R^2}} \\ &\geq \frac{\sqrt{2}}{R+h} . \end{aligned} \tag{4.61}$$

A rank-1 approximation $\widetilde{\mathbf{K}}_\beta$ given by

$$\widetilde{\mathbf{K}}_\beta = \begin{bmatrix} \dfrac{1}{R} & \dfrac{1}{R} \\ \dfrac{1}{R} & \dfrac{1}{R} \end{bmatrix} , \tag{4.62}$$

has an element-wise error

$$\mathbf{K}_\beta - \widetilde{\mathbf{K}}_\beta = \begin{bmatrix} 0 & \dfrac{-h}{R(R+h)} \\ \dfrac{h}{R(R-h)} & 0 \end{bmatrix} . \tag{4.63}$$

The spectral norm of this anti-diagonal matrix is given by its highest amplitude element, i.e.

$$\|\mathbf{K}_\beta - \widetilde{\mathbf{K}}_\beta\|_2 = \frac{h}{R(R-h)} . \tag{4.64}$$

For a fixed tolerance $\epsilon < 1$, we further assume that the two pairs of tetrahedra are sufficiently far from each other that we also have the inequality

$$R > h\left(1 + \frac{\sqrt{2}}{\epsilon}\right). \tag{4.65}$$

Thus, combining (4.61) and (4.64), we get the upper bound of the relative error

$$\begin{aligned} \frac{\|\mathbf{K}_\beta - \widetilde{\mathbf{K}}_\beta\|_2}{\|\mathbf{K}_\beta\|_2} &\leq \frac{h(R+h)}{\sqrt{2}R(R-h)} \\ &< \frac{\sqrt{2}h}{R-h} \\ &< \epsilon\,, \end{aligned} \tag{4.66}$$

which confirms that $\widetilde{\mathbf{K}}_\beta$ is a valid rank-1 approximation of $\mathbf{K}_\beta$ for the prescribed accuracy ϵ. However, according to (4.52) the corresponding approximated matrix entry in $\widetilde{\mathbf{S}}_{\mathbf{vv}}$ is

$$\begin{aligned} (\widetilde{\mathbf{S}}_{\mathbf{vv}})_{ij} &= -a_i a_j \left(\widetilde{G}(\boldsymbol{c}_i^+, \boldsymbol{c}_j^+) - \widetilde{G}(\boldsymbol{c}_i^+, \boldsymbol{c}_j^-) - \widetilde{G}(\boldsymbol{c}_i^-, \boldsymbol{c}_j^+) + \widetilde{G}(\boldsymbol{c}_i^-, \boldsymbol{c}_j^-)\right) \\ &= -a_i a_j \left(\frac{1}{R} - \frac{1}{R} - \frac{1}{R} + \frac{1}{R}\right) \\ &= 0\,. \end{aligned} \tag{4.67}$$

Therefore, it follows that

$$\frac{|(\mathbf{S}_{\mathbf{vv}})_{ij} - (\widetilde{\mathbf{S}}_{\mathbf{vv}})_{ij}|}{|(\mathbf{S}_{\mathbf{vv}})_{ij}|} = 1 > \epsilon\,, \tag{4.68}$$

which means that the error in $\widetilde{\mathbf{S}}_{\mathbf{vv}}$ is not bounded by ϵ. This example shows that beyond a certain distance, the entries in the final matrix $\mathbf{S}_{\mathbf{vv}}$ require a higher accuracy than that guaranteed by the compression of the point kernel matrix $\mathbf{K}$. As a result, these entries may be pure noise.

4.5.4 Minimum Spanning Tree Solution

The previous analysis showed a discrepancy between the amplitude of the point interactions in $\mathbf{K}$ and the final matrix entries in $\mathbf{Z}$. This issue can be solved by using interactions that have the same asymptotic scaling as the desired final result while still retaining the simplicity of point interactions. This is achieved with the following strategy.

We denote Q_t the set of N_t testing quadrature points needed to get the desired operator matrix, i.e. used to compute the outer numerical integrals. A graph of

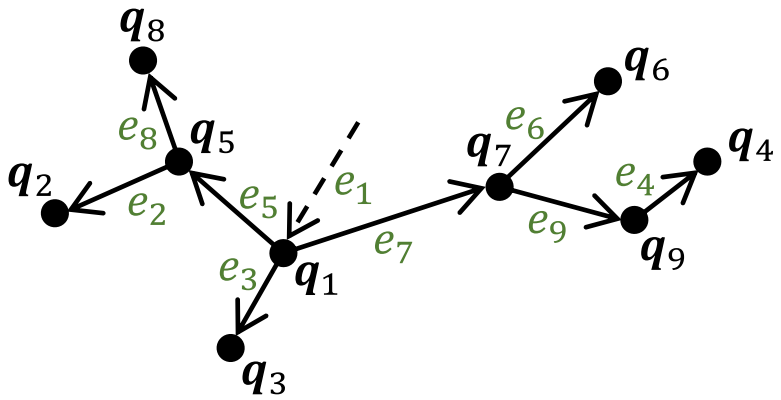

Figure 4.7: Minimum spanning tree for a set of 9 quadrature points. The dashed arrow represents the incomplete edge with no origin and pointing to the tree root.

weighted edges between each point and all nearby points is created in $\mathcal{O}(N_t \log N_t)$ complexity using the octree decomposition of Q_t. The weight of each edge is equal to its length. Then, from this graph, a minimum spanning tree (MST) E_t is built. E_t is a subset of $N_t - 1$ graph edges connecting the N_t points without cycle and having the minimum possible total weight. It is also obtained in $\mathcal{O}(N_t \log N_t)$ complexity. Then, an arbitrary point of Q_t is defined as the root of the MST, and the edges are directed from the root to the leaves. The origin point of an edge is called parent of the end point. Since E_t contains no cycle, each point in Q_t has a unique parent, except for the root, which is ancestor of all other points and has itself no parent. To have as many edges as the number of testing points, we append to E_t an additional incomplete root edge that ends on the root testing point but has no origin. An example MST is illustrated in Figure 4.7.

Instead of building a point interaction matrix $\widetilde{\mathbf{K}}$, we will compute an edge interaction matrix $\widetilde{\mathbf{K}}_\mathbf{e}$. Each edge of E_t is associated to its middle point and the set of edges is decomposed into the octree B_{te}. The same procedure is applied to the set of source quadrature points Q_s to get the octree of source edges B_{se}. We then build the block cluster tree $T_{B_{te} \times B_{se}}$ that partitions all the edge interactions. The edge interaction between the i^{th} testing edge with origin and end points $\boldsymbol{q}_i^+$ and $\boldsymbol{q}_i^-$, and the j^{th} source edge with origin and end points $\boldsymbol{q}_j^+$ and $\boldsymbol{q}_j^-$, is defined as

$$(\mathbf{K}_\mathbf{e})_{ij} = K(\boldsymbol{q}_i^+, \boldsymbol{q}_j^+) - K(\boldsymbol{q}_i^+, \boldsymbol{q}_j^-) - K(\boldsymbol{q}_i^-, \boldsymbol{q}_j^+) + K(\boldsymbol{q}_i^-, \boldsymbol{q}_j^-)\,. \tag{4.69}$$

If testing and source quadrature points coincide, the singular kernel function is set to 0. Furthermore, the row corresponding to the interaction of the testing root edge with all source edges, as well as the column corresponding to the interaction of all testing edges with the source root edge, are excluded from the block cluster tree and fully computed outside the compression. This represents a small memory

overhead of $N_t + N_s - 1$ entries. To compute them, the terms involving a missing origin point in (4.69) are set to 0.

Compared to the point interactions of $\mathbf{K}$ (cf. (4.29)), edge interactions require slightly more operations but have the same amplitude as the cancelling entries of the operator matrix $\mathbf{Z}$. Therefore, the compression of $\mathbf{K_e}$ does not compromise the accuracy of $\mathbf{Z}$ beyond the ACA tolerance ϵ.

The two kernel matrices $\mathbf{K}$ and $\mathbf{K_e}$ are related by the product

$$\mathbf{K_e} = \mathbf{T}_t \mathbf{K} \mathbf{T}_s^T \,, \tag{4.70}$$

where $\mathbf{T}_t$ and $\mathbf{T}_s$ are square testing and source point-to-edge transformation matrices respectively. These matrices are sparse and easily obtained as

$$(\mathbf{T}_t)_{ij} = \begin{cases} 1 & \text{if } \boldsymbol{q}_j = \boldsymbol{q}_i^+ \text{ (testing edge origin)} \\ -1 & \text{if } \boldsymbol{q}_j = \boldsymbol{q}_i^- \text{ (testing edge end)} \\ 0 & \text{otherwise}\,, \end{cases} \tag{4.71}$$

and similarly for $\mathbf{T}_s$ with source edges and quadrature points. Thus, after compressing $\mathbf{K_e}$, and following (4.30), the approximation of $\mathbf{Z}$ reads

$$\begin{aligned} \widetilde{\mathbf{Z}} &= \mathbf{Z}_{near} + \mathbf{\Theta \Xi} \widetilde{\mathbf{K}} \mathbf{\Xi}^T \mathbf{\Theta}^T \\ &= \mathbf{Z}_{near} + \mathbf{\Theta \Xi} {\mathbf{T_t}}^{-1} \widetilde{\mathbf{K_e}} ({\mathbf{T_s}}^T)^{-1} \mathbf{\Xi}^T \mathbf{\Theta}^T \,. \end{aligned} \tag{4.72}$$

While the $\mathbf{T}$ matrices are sparse, their inverses are not. If they were stored explicitly, the memory cost and matrix-vector multiplication $\widetilde{\mathbf{Z}}\boldsymbol{x}$ would be in $\mathcal{O}(N^2)$ complexity, which does not fit a fast solver. Fortunately, we can use the tree structure of the testing and source MST to avoid dense matrices and get the matrix-vector product $\boldsymbol{u} = {\mathbf{T_t}}^{-1}\boldsymbol{x}$ and $\boldsymbol{v} = ({\mathbf{T_s}}^T)^{-1}\boldsymbol{x}$ in linear complexity.

In the first case, the coefficient corresponding to the root point is directly obtained from the root edge entry as

$$u_r = -x_r \,, \tag{4.73}$$

where r is the root index of E_t. Then, the testing MST is traversed downward following the recursive relation

$$u_i = u_{p(i)} - x_i \,, \tag{4.74}$$

where $p(i)$ is the parent of point i. The relationship is reversed in the transposed case: any leaf coefficient l is determined from $\boldsymbol{x}$ as

$$v_l = -x_l \,, \tag{4.75}$$

and the source MST is traversed in ascending order according to the recursive relation

$$v_i = -x_i + \sum_{j \in c(i)} v_j \,, \tag{4.76}$$

where $c(i)$ is the set of children of i in E_s. Since each point is traversed exactly once, both matrix-vector multiplications are performed in linear complexity.

4.6 Multithreaded Implementation of the Fast Solver

An important feature of fast solvers is their scalability, and in particular, how easily they can be parallelized to take full advantage of the available computational resources. For the proposed fast solver, parallelism was implemented with offline task scheduling in a shared memory environment. Due to the block structure of the fast solver, all computations are relatively easy to parallelize. We distinguish three main operations:

- the near field computation;
- the far field compression;
- the matrix-vector multiplication.

The first two operations constitute the matrix filling effort, while the last one is key to how fast the solution of the problem is obtained with an iterative solver. Owing to the block cluster tree described in Section 4.2.2, each block can be computed and multiplied independently from all other blocks. This provides a trivial way to parallelize the matrix filling. Each worker (a thread or process) is assigned a set of blocks and fills them sequentially by allocating the required memory, and either

- for full blocks (near field), computing all of the interactions in the block;
- for compressible blocks (far field), applying the ACA algorithm and recompressing immediately with the QR-SVD algorithm.

For a full block of size $m \times n$, the workload and memory requirements are known exactly in advance. The number of entries to compute simply corresponds to the product of the dimensions of the block, equal to mn. However, the same cannot be said about compressible blocks. Indeed, in this case, only k rows and columns are computed and the memory cost is $k(m+n)$. Since the compression rank k is determined adaptively during the ACA algorithm, neither memory nor computation time are known in advance. For this reason, some blocks may be compressed by a worker much faster than the others and scheduling a completely balanced workload across all workers is more challenging. To combat this issue, a possibility is to estimate in advance the rank and use this information to distribute the workload as evenly as possible. In the current implementation, we opted to call the parallel compression over all the blocks within each level separately. Indeed, blocks within the same level have the same testing and source box edge lengths as well as the same relative spatial separation (there is approximately one box between every pair of boxes making an admissible block). Thus, given the translation and

rotation invariance properties of the Green's function, the compressibility should be similar across the blocks.

As highlighted in (4.32) and (4.50), the matrix-vector multiplication is performed separately for the near and far interactions and the results are summed together. The near field matrix-vector product is simply computed as a sparse matrix-vector product. As in the matrix filling process, the far field matrix-vector product follows the block structure of the block cluster tree. It also benefits from the level-wise distinction of the blocks. Indeed, within each block cluster tree level, all the blocks that have the same testing box fill the same rows of the matrix-vector product, and two blocks that have different testing boxes fill different rows. Therefore, the far field matrix-vector product is easily parallelized without race condition by assigning to each worker all the blocks with the same testing box within each level.

4.7 Numerical Results

4.7.1 Spherical Model

The performance of the proposed fast solver technique for EEG forward modeling is validated with numerical experiments. We first test it on a homogeneous sphere of radius 1, uniformly discretized into several meshes with decreasing average edge length. A dipole excitation is placed near the center of the sphere. The ACA tolerance is set to $\epsilon = 10^{-3}$, the recompression tolerance to $\epsilon' = 10^{-2}$, the admissibility parameter to $\eta = 1$ and the minimum box size to 2 times the average cell diameter. A 1-point quadrature rule is used for the compression of the far field interactions while we use an accurate semi-analytical integration rule (analytical source integral and 7-point quadrature testing integral) for near field interactions.

Despite the 10^{-2} compression threshold, the solution accuracy remains very high as illustrated in Figure 4.8, with a relative error against an analytical solution around 10^{-4}. This demonstrates the efficiency of the multilevel partitioning, which allows us to isolate a small near field computed with high precision while the highly compressible rest of the matrix has a comparatively smaller impact on the solution accuracy.

Next, we show the memory consumption of the fast solver at different discretizations in Figure 4.9. It can be seen that both near field and far field interactions grow almost linearly with the number of unknowns. This shows that a standard BEM problem with up to 1 million unknowns can run on a standard computer without problem. In comparison, without fast solver acceleration, storing the full BEM system matrix of a mesh with about 50 000 unknowns would already exceed the memory cost of the compressed problem with 1 million unknowns.

The asymptotic reduction in memory cost directly translates to a reduction in

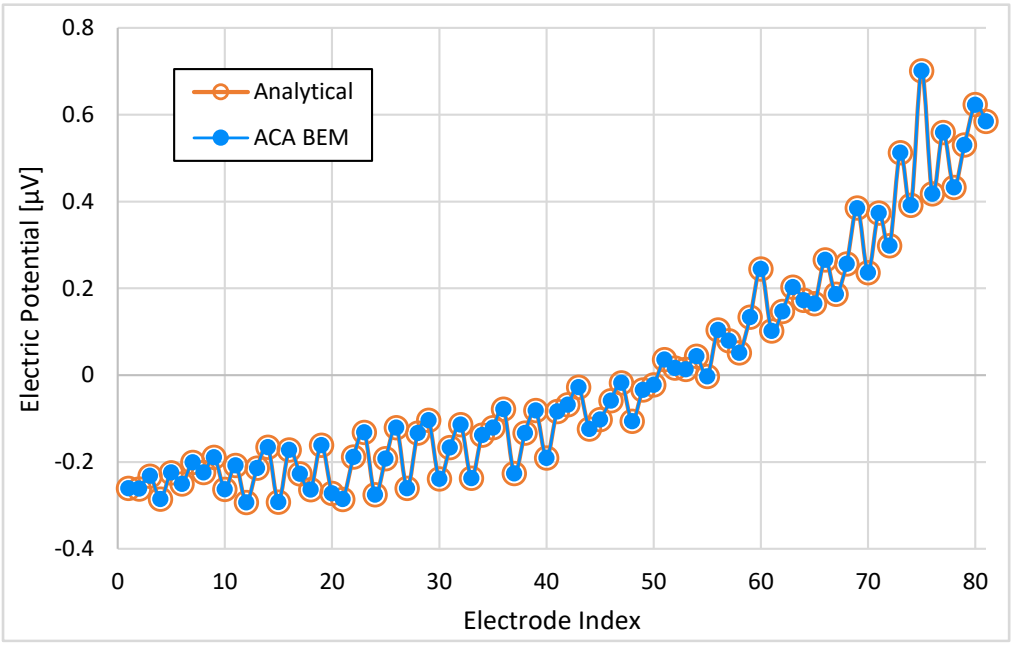

Figure 4.8: Electric potential obtained analytically and with the fast BEM solver on a set of 81 electrodes uniformly sampling the unit sphere.

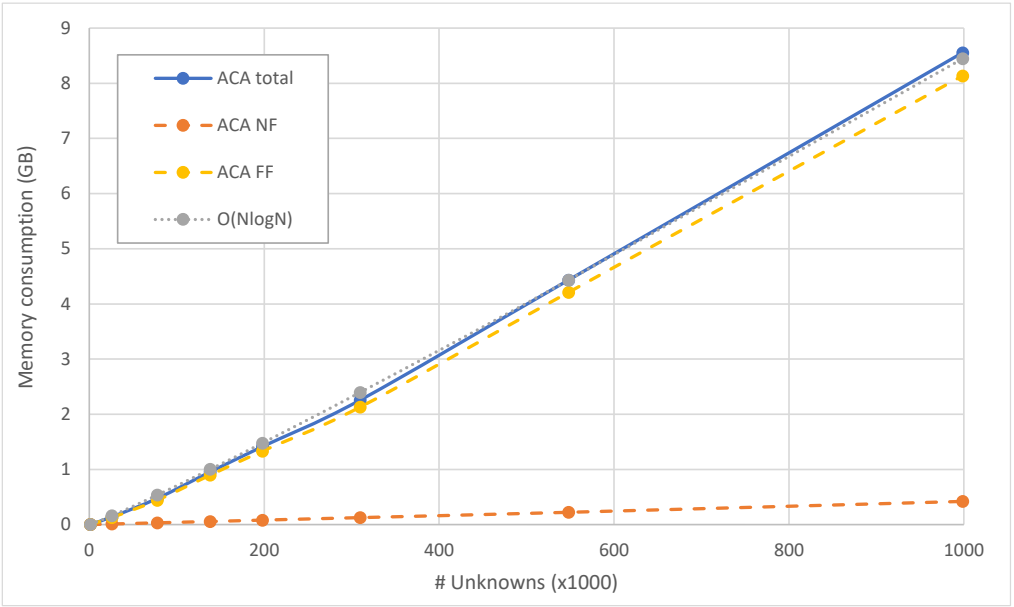

Figure 4.9: Memory cost of the compressed adjoint double-layer operator matrix on the sphere.

computation time. In Figure 4.10, the matrix filling time, i.e. the computation time of all near and compressed far interactions is displayed for different numbers

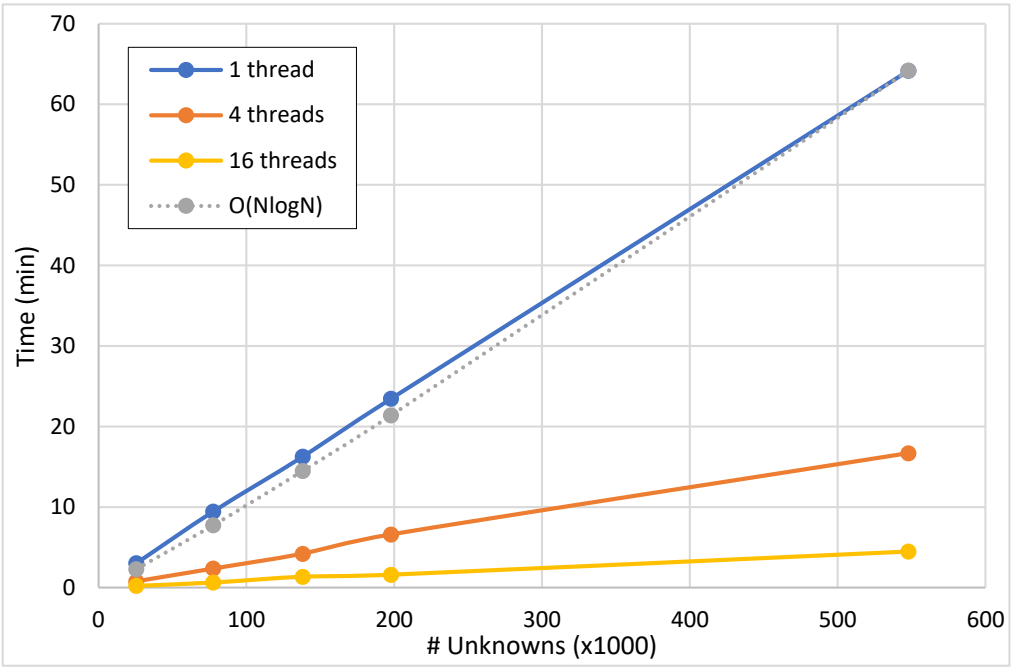

Figure 4.10: Filling time of the compressed adjoint double-layer operator matrix on the sphere.

of threads. Again, we clearly observe an $\mathcal{O}(N \log N)$ evolution with the number of unknowns. This is in agreement with the fact that the ACA algorithm computes only $\mathcal{O}(N \log N)$ interactions. Furthermore, the parallelization strategy appears quite optimal, with a reduction of computation time that is proportional to the number of threads used.

Finally, the matrix-vector product time is displayed in Figure 4.11. Again, only $\mathcal{O}(N \log N)$ operations are performed since the compressed ACA representation of the non-local operator contains only $\mathcal{O}(N \log N)$ elements. Therefore, a problem with a few hundred thousand unknowns can be solved in only a few seconds per right-hand side. The parallelization of the matrix-vector product is however slightly less optimal than in the filling case. This could be explained by the relatively low number of computations done by each thread, which accentuates the workload imbalance. To improve upon this issue, we can exploit the fact that after compression the number of elements in the compressed matrix is known exactly, and it is therefore possible to design a more balanced workload distribution. Furthermore, for problems with many right-hand sides (more than the number of workers), such as the computation of a leadfield matrix with a dense electrode array, one may simply parallelize over the independent right-hand sides rather than within the matrix-vector product.

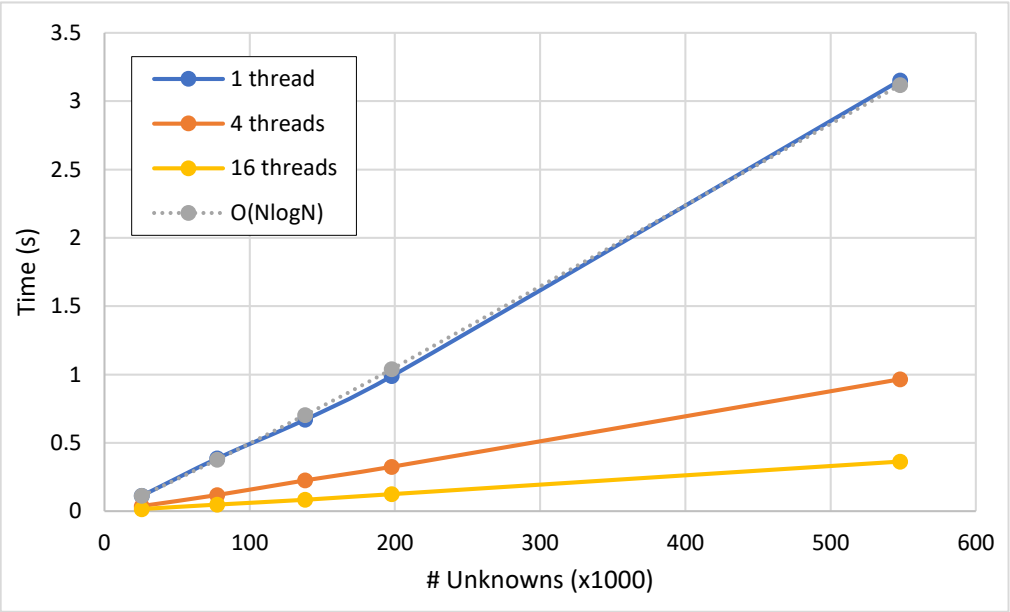

Figure 4.11: Matrix-vector multiplication timing.

4.7.2 MRI-Derived Model

The fast solver scheme with the multi-block compression is tested in a hybrid surface-volume setting. A realistic, MRI-derived head model was obtained following a procedure similar to Section 3.7.3. It consists of 3 triangular meshes delimiting the brain, skull and scalp compartments and a tetrahedral mesh of the anisotropic skull volume. We solve the hybrid surface-volume system as described in Section 4.5.2 with the proposed fast solver technique. The total number of unknowns is 33 278. While relatively large, it remains small enough that it can be solved and stored in full with the standard (non-accelerated) method which is used as a reference. A set of 8022 dipoles covering the cortex surface is used as source and the leadfield matrix is generated for a set of 72 electrodes placed on the scalp. The same parameters as in the previous sphere example are used for the fast solver. After the setup, which includes the filling of all required operator matrices and right-hand sides, the solution is obtained via the GMRES solver with a tolerance of 10^{-3}.

The memory and timing comparison is showed in Table 4.1. The potential obtained on the scalp surface with the fast solver is illustrated in Figure 4.12. We can observe that for this moderate-sized problem, the fast solver reduces memory and time consumption by a factor of 10. Furthermore, these computational gains do not compromise the solution accuracy as illustrated in Figure 4.13, and the relative leadfield matrix error with respect to the full matrix is below 10^{-2}.

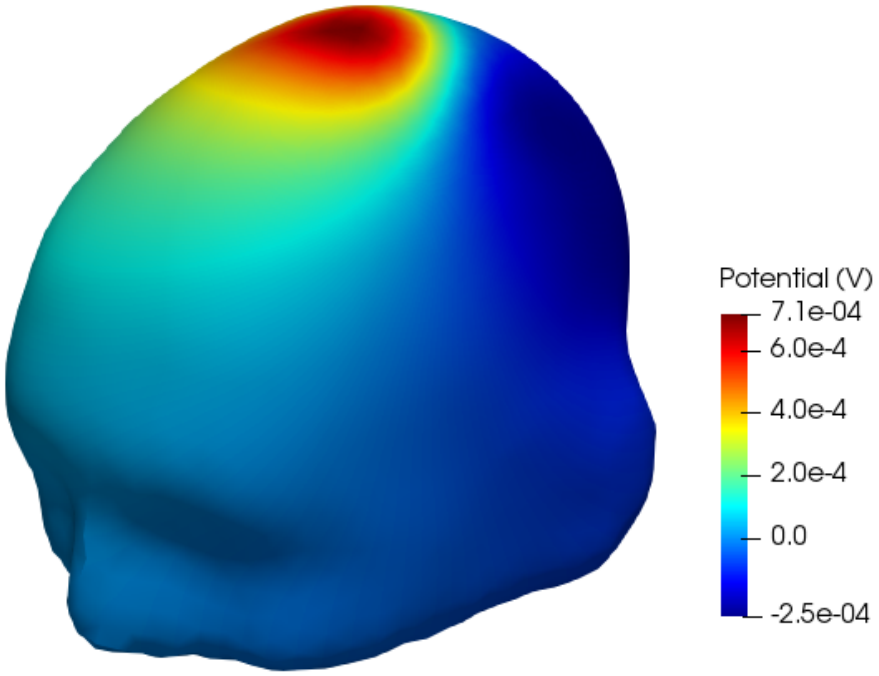

Figure 4.12: Electric potential on the scalp surface obtained with the fast solver.

4.8 Conclusion

We have presented a fast solver technique for EEG forward modeling. Based on the multilevel Adaptive Cross Approximation algorithm, it compresses the Green's function kernel in terms of quadrature point interactions. Furthermore, we developed a correction scheme using a spanning tree linking all quadrature points. For a small overhead, the resulting compression preserves the accuracy of operator matrices requiring the divergence of basis functions up to the desired tolerance while maintaining the practical advantages of a point compression. This makes it particularly suitable for integral equation formulations that involve several types of basis functions or material scalings, as multiple operator matrices can be compressed

Table 4.1: Memory and timing comparison between the standard and fast hybrid solver.

	Memory (MB)	Setup time (s)	Solution time (s)	Leadfield total time (s)
Standard solver	4224	4206	78	4441
Accelerated solver	351	394	22	462

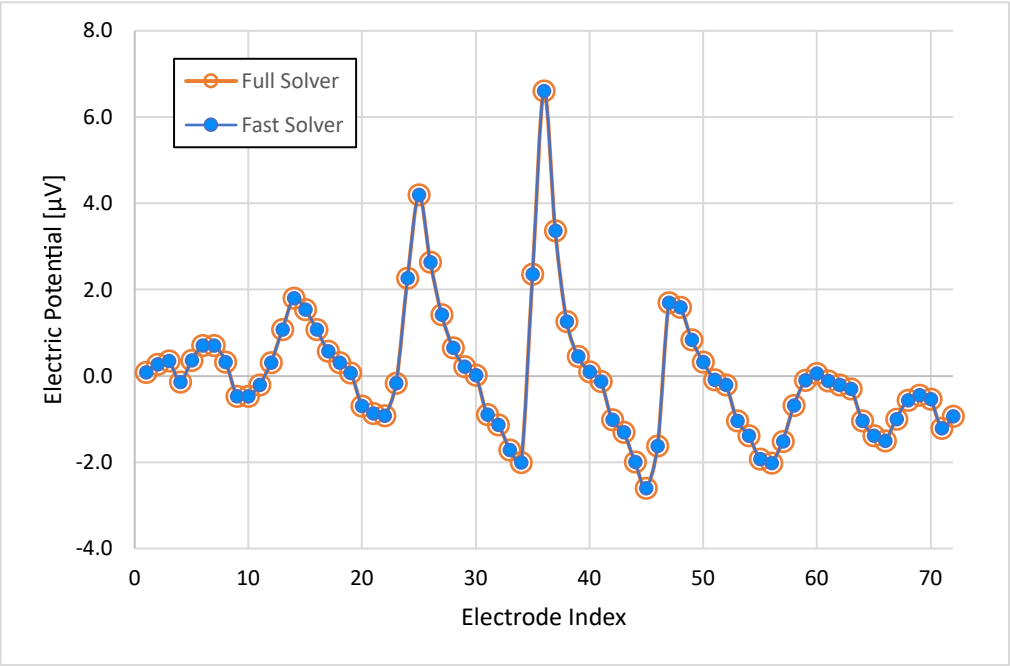

Figure 4.13: Electric potential obtained with the accelerated and non-accelerated solvers on a standardized set of 72 electrodes covering the head surface.

with a single compression. In practical applications, the proposed fast solver drastically reduces both time and memory cost for the generation of computational head models.

Chapter 5

A New Framework for Tissue Conductivity Estimation

The previous chapters focused on solving an Electroencephalography (EEG) forward problem, for which there is enough information about the equations and boundary conditions to make it well-posed. This means that it is uniquely solvable as a square system with as many independent equations and unknowns. Another family of problems, called inverse problems, arises when such information is not as complete [123]. Inverse problems are typically ill-posed. Depending on the modeling assumptions, there can be an infinity of solutions because there are more unknowns than there are equations. To bypass this issue, one can make the rectangular system square by introducing additional independent equations via the use of regularization techniques. However, the inverse problem may still remain ill-posed in the sense that small changes in the input may lead to large changes in the output solution. More generally, the unknowns of an inverse problem may not have a linear dependency with the system to solve, which makes their determination more challenging.

A classical EEG inverse problem is that of source imaging, which aims at estimating, possibly in real-time, the brain activity from EEG recordings [7]. Another important inverse problem consists in reconstructing the unknown effective conductivity profile of different head tissues. We present a new and efficient inverse strategy to solve this problem in an integral equation framework which includes on one hand the possibility to model inhomogeneity and anisotropy, and on the other hand leverages the fast solver technique presented in Chapter 4 to alleviate the computational burden and enables a fast conductivity estimation.

5.1 Tissue Conductivity Imaging

The inverse tissue conductivity problem consists in determining the conductivity of the media through which brain signals or external stimuli reach measurement electrodes at the surface of the head [27, 44]. While the head conductivity was assumed to be perfectly known in the previous chapters, in reality, the exact conductivity profile remains a topic of investigation [76]. The main reason for this is because the conductivity of each tissue varies between individuals due to factors such as age and gender. Notably, the shape and composition (e.g. fluid content) of the different head compartments evolve over extended time periods, which directly affect the electrical properties of the tissues. There are also variations in reported conductivity values in literature due to different recording techniques and experimental conditions (e.g. frequency and temperature) [57]. Finally, there are complications due to the fact that for all practical purposes, in vivo tissue conductivity is not the same as that measured in vitro. For this reason, conductivity estimation should preferably be done non-invasively [76].

The skull conductivity is of particular interest, given that its very high resistivity compared to the other tissues creates a bio-shielding effect which greatly impacts the EEG recordings [88]. One non-invasive technique is Electrical Impedance Tomography (EIT), which consists in solving an inverse problem where the head volume geometry obtained via Magnetic Resonance Imaging (MRI) and/or Computed Tomography (CT) scans, as well as boundary measurements, are known, and the conductivity distribution is to be determined [10, 44, 119]. Although non-invasive, EIT requires the solution of a forward problem, which can be computationally expensive considering that this must be performed several times in an iterative scheme. In the following, we derive the solution of the EIT forward problem in a general inhomogeneous setting, which, differently from the standard Boundary Element Method (BEM), allows local conductivity changes in small volume elements. We then derive an optimization algorithm adapted to the inhomogeneous case which makes it more versatile in its modeling abilities than standard Boundary BEM EIT solvers. This algorithm is combined with the new fast solver described in the previous chapter to enable the efficient solution of the ill-posed conductivity estimation problem. Numerical experiments confirm the validity of the proposed EIT solver.

5.2 Inhomogeneous EIT Forward Problem

A standard EIT system comprises a set of N_e recording electrodes and a current generator. The generator is connected to a pair of electrodes to form a closed circuit through which a current flows with controlled amplitude and frequency. The voltage is then recorded on the remaining electrodes and demodulated to yield

a vector $\boldsymbol{v}^m$ of $N_e - 2$ measurements of the electric potential. This constitutes an EIT dataset, which may be enlarged with several injection pairs. The inverse problem of EIT then consists in building a forward model (parametrized by the conductivity distribution) that best matches the EIT dataset [32, 43].

The EIT forward problem can be derived similarly to the standard EEG forward problem studied previously. The main difference is that an electric current is injected through a pair of surface electrodes, which can be assumed to be strong enough that the neural brain activity is negligible in comparison [30]. In response to this stimulus, an electric field is generated through the inhomogeneous and imperfectly conducting head medium and the electric potential on the scalp is recorded on the remaining electrodes [43].

Starting from an initial conductivity distribution guess, the inhomogeneous head medium is modeled similarly as in Chapter 3, by dividing it into compartments Ω_i with piecewise-homogeneous background conductivities σ_i and explicitly handling local inhomogeneities with the conductivity contrast

$$\overline{\overline{\chi}}_i(\boldsymbol{r}) = (\sigma_i \mathbf{I} - \overline{\overline{\sigma}})\,\overline{\overline{\sigma}}^{-1}(\boldsymbol{r})\,, \quad \boldsymbol{r} \in \Omega_i\,. \tag{5.1}$$

In the absence of a primary source in the volume, the Poisson's equation reads

$$\nabla \cdot (\overline{\overline{\sigma}}(\boldsymbol{r})\nabla\phi(\boldsymbol{r})) = 0, \quad \boldsymbol{r} \in \Omega\,. \tag{5.2}$$

We denote $\boldsymbol{r}_{inj}, \boldsymbol{r}_{extr} \in \partial\Omega$ the positions of the injection and extraction electrodes through which a current of amplitude I_0 is applied. The boundary conditions on each interface Γ_{ij} separating two compartments Ω_i and Ω_j are then

$$\phi(\boldsymbol{r})|^-_{\Gamma_{ij}} = \phi(\boldsymbol{r})|^+_{\Gamma_{ij}}\,, \tag{5.3a}$$

$$\hat{\boldsymbol{n}}(\boldsymbol{r}) \cdot \overline{\overline{\sigma}}(\boldsymbol{r})\nabla\phi(\boldsymbol{r})|^-_{\Gamma_{ij}} = \hat{\boldsymbol{n}}(\boldsymbol{r}) \cdot \overline{\overline{\sigma}}(\boldsymbol{r})\nabla\phi(\boldsymbol{r})|^+_{\Gamma_{ij}}\,, \quad j < N+1 \tag{5.3b}$$

$$\hat{\boldsymbol{n}}(\boldsymbol{r}) \cdot \overline{\overline{\sigma}}(\boldsymbol{r})\nabla\phi(\boldsymbol{r})|^-_{\Gamma_{iN+1}} = I_0(\delta_{r_{inj}}(\boldsymbol{r}) - \delta_{r_{extr}}(\boldsymbol{r}))\,, \tag{5.3c}$$

where we used the notation $\delta_{\boldsymbol{r}_0}(\boldsymbol{r}) = \delta(\boldsymbol{r} - \boldsymbol{r}_0)$. Note that the last equation applies to the external surface which is connected to the air with conductivity $\sigma_{N+1} = 0$. To simplify the notation, we also further assume that only the skull compartment Ω_s, $1 \leq s < N$ is inhomogeneous. This is justified by the fact that the EIT measurements resulting from a source and sink pair on the surface are mostly sensitive to the conductivity of the superficial layers, and therefore the deep white matter anisotropy does not strongly influence the result [119, 42]. Furthermore, the skull is by far the most resistive head tissue and, as such, has a strong impact on the surface measurements, which motivates us to handle it with the most realistic model [131, 1].

Following a similar derivation as in Section 3.3 with the modified boundary

condition (5.3c) leads to the surface integral equation on each interface Γ_{ij}

$$\frac{\sigma_i + \sigma_j}{2}\,\xi_{ij} + (\sigma_j - \sigma_i)\left(\hat{\boldsymbol{n}} \cdot \frac{\boldsymbol{J}_{eq_s}}{2\sigma_s} - \sum_{k,l=1}^{N+1} \mathcal{D}^* \xi_{kl} + \frac{1}{\sigma_s}\mathcal{D}_v^* \boldsymbol{J}_{eq_s}\right) = -\frac{I_0}{2}(\delta_{r_{inj}} - \delta_{r_{extr}})\,, \quad (5.4)$$

and the volume integral equation in Ω_s

$$(\sigma_s \mathbf{I} - \overline{\overline{\sigma}})^{-1}\boldsymbol{J}_{eq_s} - \sum_{k,l} \nabla\mathcal{S}\xi_{kl} + \frac{1}{\sigma_s}\nabla\mathcal{S}_v \boldsymbol{J}_{eq_s} = \mathbf{0}\,. \quad (5.5)$$

Once the surface and volume unknowns ξ_{kl} and $\boldsymbol{J}_{eq_s}$ are determined, the predicted potential on a surface electrode $\boldsymbol{r}_e$ is given by

$$\phi(\boldsymbol{r}_e) = \sum_{k,l} \mathcal{S}\xi_{kl}(\boldsymbol{r}_e) - \frac{1}{\sigma_s}\mathcal{S}_v^* \boldsymbol{J}_{eq_s}(\boldsymbol{r}_e)\,. \quad (5.6)$$

By expanding the surface unknowns with pyramid basis functions s_i (3.47) and the volume unknowns with SWG basis functions $\boldsymbol{v}_i$ (3.49) as

$$\xi(\boldsymbol{r}) = \sum_i \alpha_i s_i(\boldsymbol{r})\,, \quad (5.7)$$

$$\boldsymbol{J}_{eq}(\boldsymbol{r}) = \sum_i \overline{\overline{\chi}}\beta_i \boldsymbol{v}_i(\boldsymbol{r})\,, \quad (5.8)$$

the discrete surface and volume integral equations form the forward system

$$\mathbf{A}\boldsymbol{x} = \boldsymbol{b}\,, \quad (5.9)$$

with

$$\mathbf{A} = \begin{bmatrix} \mathbf{G_{ss}} - \mathbf{D_{ss}^*} & \mathbf{G_{sv}} - \mathbf{D_{sv}^*} \\ -\mathbf{S_{vs}} & \mathbf{G_{vv}} + \mathbf{S_{vv}} \end{bmatrix}\,, \quad (5.10)$$

where the operator matrices are defined in Section 3.4.2, and the i^{th} element of $\boldsymbol{b}$ is defined as

$$(\boldsymbol{b})_i = -\frac{I_0}{2}(s_i(\boldsymbol{r}_{inj}) - s_i(\boldsymbol{r}_{extr}))\,, \quad (5.11)$$

i.e. it is non-zero only on the two basis functions whose defining vertices coincide with the injection electrode pair. Finally, the expression of (5.6) applied to each measurement electrode gives us the vector of predicted potentials

$$\boldsymbol{v}^p = \mathbf{S}\boldsymbol{x} = \mathbf{S}\mathbf{A}^{-1}\boldsymbol{b}\,, \quad (5.12)$$

with $\mathbf{S} = [\mathbf{S_{ms}}^T \mathbf{S_{mv}}^T]^T$ defined from (3.82). The data error between the measured and the predicted potentials is the vector

$$\boldsymbol{\rho} = \boldsymbol{v}^p - \boldsymbol{v}^m\,. \quad (5.13)$$

The data error is non-zero in general due to noise sources, and we assume that they mainly come from modeling errors (in particular in the conductivity distribution) in the forward problem.

5.3 EIT Inverse Solution

We seek the conductivity distribution $\boldsymbol{\sigma} = [\sigma_1, \ldots, \sigma_{N_p}]^T$ (where N_p is the number of parameters, and depends on the modeling assumptions) in the head volume that best fits the electrode measurements. In other words, we want to minimize the cost function

$$f(\boldsymbol{\sigma}) = \|\boldsymbol{\rho}\|^2 = \|\mathbf{S}\mathbf{A}^{-1}\boldsymbol{b} - \boldsymbol{v}^m\|^2 , \tag{5.14}$$

where $\|\cdot\|$ denotes the Euclidian ℓ_2-norm. This is a non-linear problem because $\boldsymbol{\sigma}$ appears in $\mathbf{A}$ which needs to be inverted. Furthermore, in the inhomogeneous case, $\mathbf{S}$ also depends on $\boldsymbol{\sigma}$, which is not the case in the standard BEM where only piecewise-homogeneous media can be modeled. This problem can be linearized with iterative schemes such as the one described in the following. Given the conductivity distribution $\boldsymbol{\sigma}^{(n)}$ of iteration n, the EIT forward problem described in Section 5.2 is solved to get the solution $\boldsymbol{x}$, which is then used to compute $\boldsymbol{\rho}^{(n)} = \boldsymbol{\rho}(\boldsymbol{\sigma}^{(n)})$. From this error, a new conductivity distribution

$$\boldsymbol{\sigma}^{(n+1)} = \boldsymbol{\sigma}^{(n)} + \Delta\boldsymbol{\sigma} \tag{5.15}$$

is determined, which starts a new EIT iteration. The process is stopped when either f is below a threshold or $\boldsymbol{\sigma}$ has converged.

The conductivity update $\Delta\boldsymbol{\sigma}$ is determined via the Gauss-Newton method adapted to the inhomogeneous case and described hereafter. We introduce the following notation for the partial derivative matrix

$$\left(\frac{\partial \mathbf{M}}{\partial x}\right)_{ij} = \frac{\partial(\mathbf{M}_{ij})}{\partial x} , \tag{5.16}$$

where $\mathbf{M}$ is a matrix whose entries are function of the variable x. Considering that the optimal $\boldsymbol{\sigma}$ minimizes (5.14), the gradient vector of the cost function must be equal to zero, i.e. each parameter σ_j satisfies the equation

$$\begin{aligned}
& \frac{\partial f(\boldsymbol{\sigma})}{\partial \sigma_j} = 0 \\
\Leftrightarrow \quad & \frac{\partial}{\partial \sigma_j} \sum_{i=1}^{N_e-2} \left((\mathbf{S}\mathbf{A}^{-1}\boldsymbol{b})_i - \boldsymbol{v}_i^m\right)^2 = 0 \\
\Leftrightarrow \quad & 2 \sum_{i=1}^{N_e-2} \left((\mathbf{S}\mathbf{A}^{-1}\boldsymbol{b})_i - \boldsymbol{v}_i^m\right) \frac{\partial(\mathbf{S}\mathbf{A}^{-1}\boldsymbol{b})_i}{\partial \sigma_j} = 0 \\
\Leftrightarrow \quad & 2 \sum_{i=1}^{N_e-2} \left((\mathbf{S}\mathbf{A}^{-1}\boldsymbol{b})_i - \boldsymbol{v}_i^m\right) (\mathbf{J}^T)_{ij} = 0 ,
\end{aligned} \tag{5.17}$$

where the Jacobian matrix $\mathbf{J}$ is defined as

$$(\mathbf{J})_{ij} = \frac{\partial \boldsymbol{\rho}_i}{\partial \sigma_j} . \tag{5.18}$$

Equation (5.17) can be equivalently written in matrix form

$$2\mathbf{J}^T\boldsymbol{\rho} = \mathbf{0}\,. \tag{5.19}$$

Assuming that the difference between $\boldsymbol{\sigma}^{(n+1)}$ and $\boldsymbol{\sigma}^{(n)}$ is small enough, we perform a Taylor expansion of $\boldsymbol{\rho}$ in $\boldsymbol{\sigma}^{(n)}$ to obtain

$$\begin{aligned}\boldsymbol{\rho}(\boldsymbol{\sigma}^{(n+1)}) &= \boldsymbol{\rho}(\boldsymbol{\sigma}^{(n)} + \Delta\boldsymbol{\sigma}) \\ &\approx \boldsymbol{\rho}(\boldsymbol{\sigma}^{(n)}) + \mathbf{J}\Delta\boldsymbol{\sigma}\,.\end{aligned} \tag{5.20}$$

Therefore, inserting (5.20) in (5.19) gives the conductivity update for iteration $n+1$,

$$\begin{aligned} & 2\mathbf{J}^T\boldsymbol{\rho}^{(\boldsymbol{n+1})} = \mathbf{0} \\ \Leftrightarrow \quad & \mathbf{J}^T\mathbf{J}\Delta\boldsymbol{\sigma} = -\mathbf{J}^T\boldsymbol{\rho}^{(n)} \\ \Leftrightarrow \quad & \Delta\boldsymbol{\sigma} = -\left(\mathbf{J}^T\mathbf{J}\right)^{-1}\mathbf{J}^T\boldsymbol{\rho}^{(n)}\,. \end{aligned} \tag{5.21}$$

The Gauss-Newton process requires the evaluation of the Jacobian matrix at each iteration. In the inhomogeneous EIT formulation presented thus far, the columns of $\mathbf{J}$ read

$$\begin{aligned}(\mathbf{J})_{:,j} &= \frac{\partial(\boldsymbol{v}^p - \boldsymbol{v}^m)}{\partial\sigma_j} \\ &= \frac{\partial(\mathbf{S}\mathbf{A}^{-1}\boldsymbol{b})}{\partial\sigma_j} \\ &= \frac{\partial\mathbf{S}}{\partial\sigma_j}\mathbf{A}^{-1}\boldsymbol{b} + \mathbf{S}\frac{\partial\mathbf{A}^{-1}}{\partial\sigma_j}\boldsymbol{b} \\ &= \left(\frac{\partial\mathbf{S}}{\partial\sigma_j} - \mathbf{S}\mathbf{A}^{-1}\frac{\partial\mathbf{A}}{\partial\sigma_j}\right)\mathbf{A}^{-1}\boldsymbol{b}\,.\end{aligned} \tag{5.22}$$

In the following, denoting N_T the number of tetrahedra, we write $\boldsymbol{\sigma}$ as the vector of length $N_p = N + N_T$ whose first N entries are the background conductivities in each of the N head compartments, and the N_T last entries are the conductivities in the inhomogeneous tetrahedra. For simplicity, it is assumed that there is inhomogeneity but no anisotropy. Otherwise, each tetrahedron would have 6 parameters (instead of 1) corresponding to the upper triangular part of the anisotropic conductivity tensor $\overline{\overline{\sigma}}$. From (5.10) the partial derivative matrix of $\mathbf{A}$ can be constructed from the partial derivative matrix of each block. Using (3.55), the matrix entries are

- for the surface-surface block

$$\left(\frac{\partial\mathbf{G}_{\mathbf{ss}}}{\partial\sigma_p}\right)_{ij} = \frac{1}{2}\frac{\partial(\sigma_k + \sigma_l)}{\partial\sigma_p}\langle s_i, s_j\rangle_{\Gamma_{kl}}\,, \tag{5.23}$$

$$\left(\frac{\partial\mathbf{D}^*_{\mathbf{ss}}}{\partial\sigma_p}\right)_{ij} = \frac{\partial(\sigma_l - \sigma_k)}{\partial\sigma_p}\langle s_i, \mathcal{D}^* s_j\rangle_{\Gamma_{kl}}\,, \tag{5.24}$$

- for the surface-volume block

$$\left(\frac{\partial \mathbf{G_{sv}}}{\partial \sigma_p}\right)_{ij} = \frac{\partial}{\partial \sigma_p}\left(\frac{\sigma_k+\sigma_l}{2\sigma_s}\right)\langle s_i, \chi \hat{\boldsymbol{n}}\cdot\boldsymbol{v}_j\rangle_{\Gamma_{kl}} + \frac{\sigma_k+\sigma_l}{2\sigma_j}\langle s_i, \frac{\partial\chi}{\partial\sigma_p}\hat{\boldsymbol{n}}\cdot\boldsymbol{v}_j\rangle_{\Gamma_{kl}}\,, \tag{5.25}$$

$$\left(\frac{\partial \mathbf{D^*_{sv}}}{\partial \sigma_p}\right)_{ij} = \frac{\partial}{\partial \sigma_p}\left(\frac{\sigma_l-\sigma_k}{\sigma_s}\right)\langle s_i, \mathcal{D}_v^*\chi\boldsymbol{v}_j\rangle_{\Gamma_{kl}} + \frac{\sigma_l-\sigma_k}{\sigma_s}\langle s_i, \mathcal{D}_v^*\frac{\partial\chi}{\partial\sigma_p}\boldsymbol{v}_j\rangle_{\Gamma_{kl}}\,, \tag{5.26}$$

- for the volume-surface block

$$\left(\frac{\partial \mathbf{S_{vs}}}{\partial \sigma_p}\right)_{ij} = \frac{\partial}{\partial\sigma_p}\langle \boldsymbol{v}_i, \nabla\mathcal{S}s_j\rangle_{\Omega_s} = 0\,, \tag{5.27}$$

- and for the volume-volume block

$$\left(\frac{\partial \mathbf{G_{vv}}}{\partial \sigma_p}\right)_{ij} = \frac{\partial}{\partial \sigma_p}\left(\frac{1}{\sigma_{T_j^+}}\right)\langle \boldsymbol{v}_i, \boldsymbol{v}_j\rangle_{T_j^+} + \frac{\partial}{\partial \sigma_p}\left(\frac{1}{\sigma_{T_j^-}}\right)\langle \boldsymbol{v}_i, \boldsymbol{v}_j\rangle_{T_j^-}\,, \tag{5.28}$$

$$\left(\frac{\partial \mathbf{S_{vv}}}{\partial \sigma_p}\right)_{ij} = \frac{\partial}{\partial \sigma_p}\left(\frac{1}{\sigma_s}\right)\langle \boldsymbol{v}_i, \nabla\mathcal{S}_v\chi\boldsymbol{v}_j\rangle_{\Omega_s} + \frac{1}{\sigma_s}\langle \boldsymbol{v}_i, \nabla\mathcal{S}_v\frac{\partial\chi}{\partial\sigma_p}\boldsymbol{v}_j\rangle_{\Omega_s}\,. \tag{5.29}$$

The usual rules of differentiation are applied to the conductivity factors. For instance, in the tetrahedron T with conductivity σ_T, we have

$$\frac{\partial\chi}{\partial\sigma_p} = \frac{\partial}{\partial\sigma_p}\left(\frac{\sigma_s-\sigma_T}{\sigma_T}\right) = \begin{cases} \dfrac{1}{\sigma_T} & \text{if } \sigma_p = \sigma_s \\ -\dfrac{\sigma_s}{\sigma_T^2} & \text{if } \sigma_p = \sigma_T \\ 0 & \text{otherwise}\,. \end{cases} \tag{5.30}$$

Similarly for the $(N_e-2)\times N_{DoF}$ operator matrix $\mathbf{S}$, we have

$$\left(\frac{\partial \mathbf{S_{ms}}}{\partial \sigma_p}\right)_{ij} = \frac{\partial}{\partial\sigma_p}\int_\Gamma G(\boldsymbol{r}_i,\boldsymbol{r}')s_j(\boldsymbol{r}')\,\mathrm{d}S' = 0\,, \tag{5.31}$$

$$\begin{aligned}\left(\frac{\partial \mathbf{S_{mv}}}{\partial \sigma_p}\right)_{ij} &= \frac{\partial}{\partial\sigma_p}\left(\frac{1}{\sigma_j}\right)\int_\Omega G(\boldsymbol{r}_i,\boldsymbol{r}')\nabla'\cdot(\chi\boldsymbol{v}_j(\boldsymbol{r}'))\,\mathrm{d}V' \\ &\quad + \frac{1}{\sigma_j}\int_\Omega G(\boldsymbol{r}_i,\boldsymbol{r}')\frac{\partial\chi}{\partial\sigma_p}\nabla'\cdot\boldsymbol{v}_j(\boldsymbol{r}')\,\mathrm{d}V'\,.\end{aligned} \tag{5.32}$$

Once the Jacobian matrix $\mathbf{J}$ is computed using (5.23)–(5.32), the new conductivity is finally obtained according to (5.21) as

$$\boldsymbol{\sigma}^{(n+1)} = \boldsymbol{\sigma}^{(n)} - \left(\mathbf{J}^T\mathbf{J}\right)^{-1}\mathbf{J}^\mathsf{T}\boldsymbol{\rho}^{(n)}\,. \tag{5.33}$$

5.4 Fast Conductivity Updates

The inverse algorithm described in the previous section requires that a forward problem must be solved for a new conductivity guess at each EIT iteration. This appears computationally burdensome, especially for high resolution models that include fine geometrical details of the head. In such realistic cases, the high number of unknowns to solve for would make each EIT update slow and the overall pipeline impractical. It can be noted however that

- while the conductivity distribution varies with each update, the geometry of the head remains fixed;
- there are relatively few right-hand sides $\boldsymbol{b}$ to solve for in each EIT iteration.

These two observations suggest that a fast solver technique such as the one presented in Chapter 4 could prove highly advantageous in the EIT setting. In this section we leverage the special structure of the quadrature point-based Adaptive Cross Approximation (ACA) to derive an efficient EIT algorithm in which a minimal processing effort is needed per EIT update, thus allowing for fast conductivity estimation.

Using similar notation as introduced in Section 4.5, assume that an operator matrix $\mathbf{Z}$ ($\mathbf{Z} \in \left\{\mathbf{D}^*_{\mathbf{ss}}, \mathbf{D}^*_{\mathbf{sv}}, \mathbf{S}_{\mathbf{vs}}, \mathbf{S}_{\mathbf{vv}}\right\}$) of the system matrix $\mathbf{A}$ has been compressed into

$$\mathbf{Z} = \mathbf{Z}_{near} + \mathbf{\Theta}_L \mathbf{\Xi}_L \mathbf{K} \mathbf{\Xi}_R^T \mathbf{\Theta}_R^T . \tag{5.34}$$

The R (right) and L (left) subscripts stem from the fact that testing and source domains are not always the same. The point to cell transformation matrices are slightly modified to include testing and source conductivity-dependent scalings α_L and α_R:

$$(\mathbf{\Xi}_L)_{ij} = \begin{cases} \alpha_L a_{c_j} w_j f_i(\boldsymbol{r}_j) & \text{if } \boldsymbol{r}_j \text{ belongs to } c_i \\ 0 & \text{otherwise} . \end{cases} \tag{5.35}$$

$$(\mathbf{\Xi}_R)_{ij} = \begin{cases} \alpha_R a_{c_j} w_j f_i(\boldsymbol{r}_j) & \text{if } \boldsymbol{r}_j \text{ belongs to } c_i \\ 0 & \text{otherwise} . \end{cases} \tag{5.36}$$

The specific scaling values for each operator matrix are synthesized in Table 5.1. The remaining Gram matrices, as well as $\mathbf{S}$ and $\mathbf{Z}_{near}$ are not problematic since they contain only $\mathcal{O}(N_{DoF})$ elements. With this representation, differentiating $\mathbf{Z}$ with respect to σ_j for the computation of $\mathbf{J}$ yields

$$\begin{aligned} \frac{\partial \mathbf{Z}}{\partial \sigma_j} &= \frac{\partial}{\partial \sigma_j} \left(\mathbf{Z}_{near} + \mathbf{Z}_{far} \right) \\ &= \frac{\partial \mathbf{Z}_{near}}{\partial \sigma_j} + \mathbf{\Theta}_L \frac{\partial \mathbf{\Xi}_L}{\partial \sigma_j} \mathbf{K} \mathbf{\Xi}_R^T \mathbf{\Theta}_R^T + \mathbf{\Theta}_L \mathbf{\Xi}_L \mathbf{K} \frac{\partial \mathbf{\Xi}_R^T}{\partial \sigma_j} \mathbf{\Theta}_R^T , \end{aligned} \tag{5.37}$$

Algorithm 3: EIT inverse algorithm

Input : measurement vector $\boldsymbol{v}^{(m)}$, initial guess $\boldsymbol{\sigma}_{init}$, error tolerance ϵ, minimum step α, maximum iterations n_{max}
Output: conductivity distribution $\boldsymbol{\sigma}$

```
compress operator matrix kernels with Algorithm 2;
compute material-independent (unscaled) matrices and right-hand sides;
σ ← σ_init ;
for n ← 1 to n_max do
    update sparse scaling matrices;
    x ← A^{-1} b;
    ρ ← S x − v^(m);
    compute J via (5.22);
    Δσ ← −(J^T J)^{-1} J^T ρ;
    if Δσ ≤ α or ‖ρ‖^2 ≤ ε then
        break;
    end
    σ ← σ + Δσ;
end
```

which highlights the fact that the same compressed kernel matrix $\mathbf{K}$ is necessary for a matrix-vector multiplication independently of the conductivity distribution $\boldsymbol{\sigma}$. This appears logical considering that the non-separable part of the system matrix stems from the Green's function. This function depends only on relative distances as opposed to the material which is a local information, individually embedded within each element. Therefore, one needs to perform the matrix compression only once as a preprocessing step, and the EIT updates require the rescaling of some sparse transformation matrices only, which is quite inexpensive. Summarizing, the complete inverse EIT procedure is given in Algorithm 3. The inverse of the system matrix $\mathbf{A}$, required to compute $\boldsymbol{x}$ and $\mathbf{J}$, is never explicitly computed and the solution is instead obtained with a Krylov subspace method such as the Generalized Minimal Residual (GMRES) method [104].

Table 5.1: Conductivity scalings of the transformation matrices for each operator of the EIT formulation.

Scaling	$\mathbf{D}^*_{\mathbf{ss}}$	$\mathbf{D}^*_{\mathbf{sv}}$	$\mathbf{S}_{\mathbf{vs}}$	$\mathbf{S}_{\mathbf{vv}}$
α_L	$\sigma_k - \sigma_l$	$\sigma_k - \sigma_l$	1	1
α_R	1	χ/σ_s	1	χ/σ_s

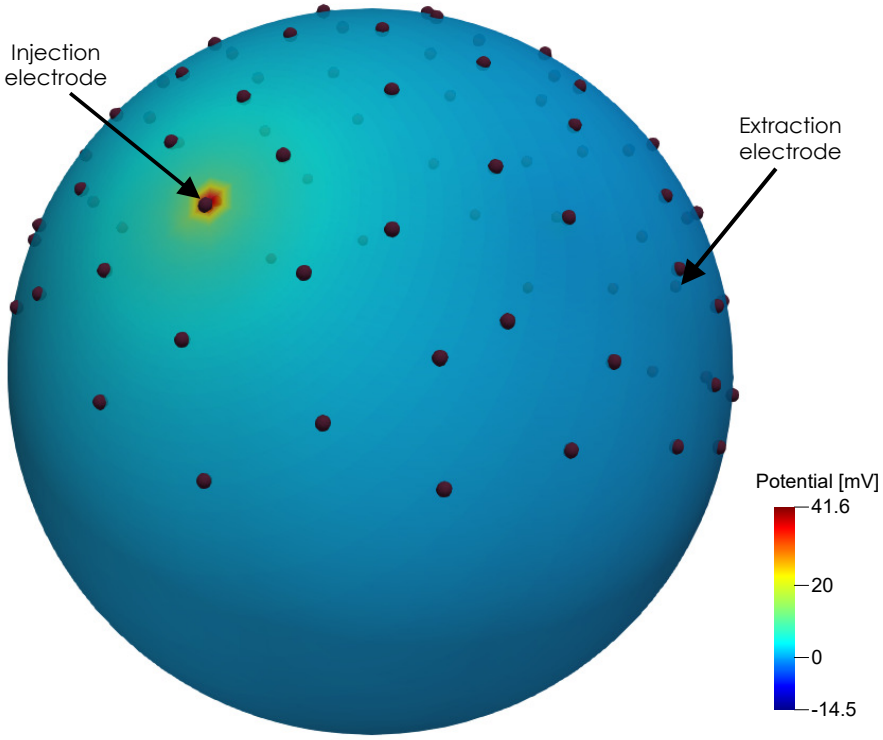

Figure 5.1: Electric potential on the surface of a 3-layer spherical geometry.

The convergence of iterative Gauss-Newton methods such as the proposed inverse EIT algorithm depends on the initialization of the vector $\boldsymbol{\sigma}_{init}$. Inappropriate initialization may result in low convergence speed or convergence to a wrong local minimum. Given that the head tissue conductivities are approximately known [73], empirical experiments have shown that it is best to initialize the conductivity with values slightly lower than those referenced in literature [43].

5.5 Numerical Results

We validate the proposed EIT algorithm through several numerical simulations involving both spherical and realistic head geometries. First, a forward head model with ground truth conductivity values is generated. This reference model is used to simulate EIT measurements on a set of scalp electrodes. The ground truth conductivity of the skull is then assumed to be unknown and we run the EIT algorithm to estimate it starting from different initial conductivity guesses.

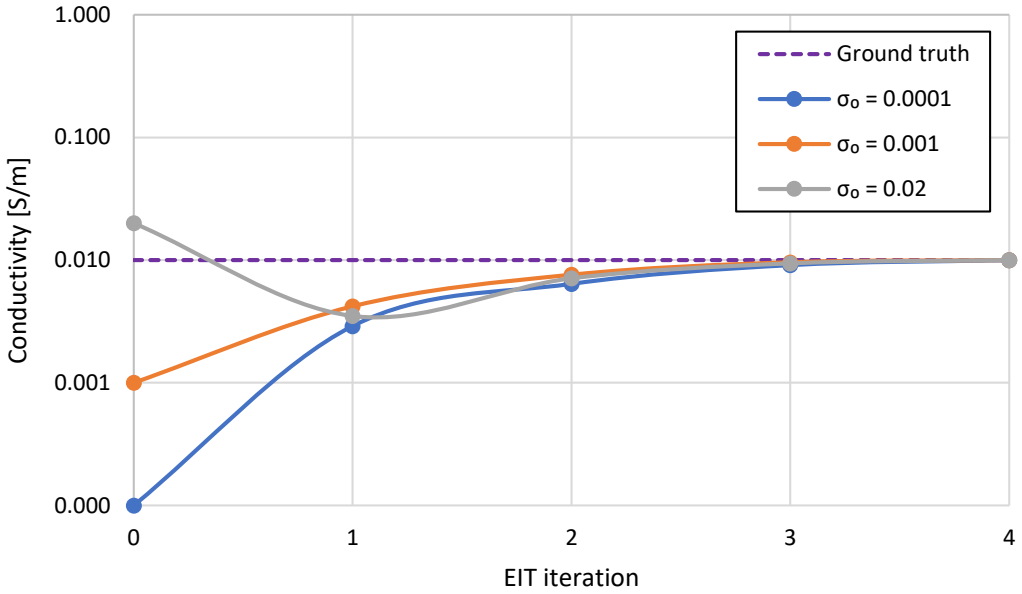

Figure 5.2: Convergence of the EIT algorithm for different initial conductivities.

5.5.1 Spherical Head Model

Similar to the numerical example of Section 3.7.1, the geometry is a canonical 3-layer spherical head model with normalized radii of 0.87, 0.92 and 1, and ground truth conductivities 0.33, 0.01 and 0.43 S/m, respectively. These compartments represent homogeneous brain, skull and scalp and the skull conductivity is assumed to be unknown. The discretized spheres result in a matrix system of 3218 unknowns. A set of 80 electrodes, which approximately samples the upper half surface of the external layer, is used in the EIT experiment. A current of normalized amplitude is injected on two electrodes which are approximately located on opposite sides of the sphere, as illustrated in Figure 5.1, while the reference electrode is placed on the top. This yields a synthetic EIT measurement vector $\boldsymbol{v}^m$ of size 77 that will be used as input for the EIT reconstruction algorithm.

Starting from different initial skull conductivity guesses, we run the EIT algorithm and the conductivity updates are displayed in Figure 5.2. Clearly, as long as the starting conductivity guess is not excessively higher than the actual value, the EIT algorithm converges within 4 iterations to the ground truth value. However, initializing the algorithm with a guess that is too high (e.g. $\sigma_0 = 0.03$ S/m, not displayed in the figure) results in a non-physical negative conductivity in the second iteration and therefore does not converge since the EIT forward problem cannot be solved anymore. This was also observed in [43] and confirms that it is better to set an initial guess that is on the lower end of the expected conductivity, as even a value that is a hundred times lower safely converges to the ground truth.

Table 5.2: Convergence and timing of the EIT inverse algorithm in an inhomogeneous MRI-derived head model.

	Setup	Iter. 1	Iter. 2	Iter. 3	Iter. 4	Iter. 5
Cumulative timing (s)	401	410	420	429	438	448
Relative error (%)	-	30.88	15.87	5.45	1.07	0.15
σ_{soft} (S/m)	-	0.005	0.030	0.071	0.096	0.104
σ_{hard} (S/m)	-	0.0005	0.0029	0.0068	0.0094	0.010

5.5.2 Realistic Head Model

We also tested the proposed EIT on a realistic head model obtained from MRI data. More specifically, we used the head model of Section 4.7.2 with 3 surfaces representing brain, skull, and scalp compartments. The skull is assumed inhomogeneous and thus its volume is discretized with tetrahedra. The thickness fraction of soft bone follows a linear function of the local skull thickness, and the conductivity in each tetrahedron is a function of soft and hard bone conductivities σ_{soft} and σ_{hard}, following (3.10). Therefore, in this setting, the inverse problem has two parameters. The discretized surface-volume system contains 33 278 unknowns. A ground truth EIT datasewt is generated with $\sigma_{soft} = 0.01$ S/m and $\sigma_{hard} = 0.001$ S/m, giving a synthetic data vector of size 73 electrode measurements. The scalp potential resulting from an EIT injection pair is illustrated in Figure 5.3.

The inhomogeneous skull conductivity is then assumed unknown and estimated with the EIT procedure from the EIT measurements. The starting values for σ_{soft} and σ_{hard} are 20 times lower than the actual values. The results are reported in Table 5.2.

The initial setup corresponds to mesh preprocessing, octree and block cluster tree building, and matrix filling which includes the compression of the far field blocks and the computation of the near field blocks. Following Algorithm 3, during each EIT iteration the sparse transformation matrices are updated and the forward system matrix is solved to get the new conductivity guess. The EIT procedure converges with less than 1% relative error to the ground truth values in 5 iterations. The performance of the fast solver acceleration becomes apparent in this numerical experiment. After the initial setup, the cumulative time for the 5 EIT iterations is less than a minute. Without a fast solver that factors the variable conductivity out of the compression, every single iteration would require nearly the full setup time, resulting in a much more time consuming EIT pipeline.

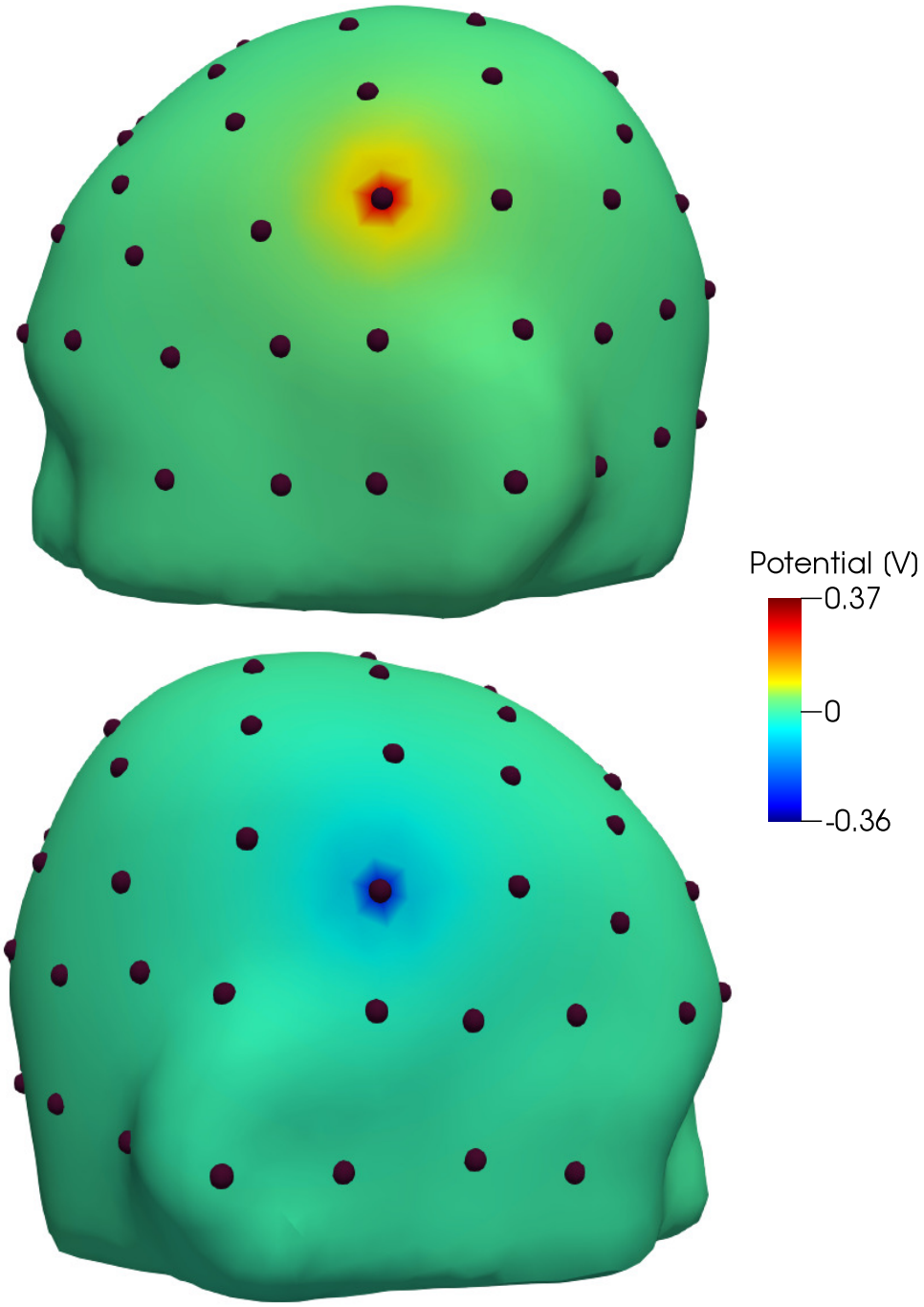

Figure 5.3: Electric potential on the surface of an MRI-derived head model and resulting from a current injection pair.

5.6 Conclusion

A new integral equation-based inverse technique was developed for the estimation of the head tissue conductivity in both homogeneous and inhomogeneous settings. This was achieved by adapting the derived hybrid integral equations to EIT scenarios. Synthetic examples showed that the optimization algorithm had good convergence and that the time consuming iterative process is significantly sped up with the use of a dedicated fast solver. The robustness of the pipeline under more challenging conditions (noisy measurements) and the integration of other priors will be the subject of further study.

Chapter 6

Conclusion and Perspectives

This thesis concludes several years of research in computational electromagnetics, with a focus in integral equation formulations for bioelectromagnetic brain modeling. The main axes were on one hand, the development of a formulation that enables the accurate representation of different head tissue inhomogeneities and anisotropies, and on the other hand, the development of a fast solver technique to improve both time and memory complexity of brain formulations. These advances are notably investigated for the inverse problem of conductivity imaging. More generally, this work should prove beneficial in clinical and research applications by enabling the practical use of more realistic and detailed models.

The work done during this thesis also paves the way for future research including:

- The study of a fully symmetric anisotropy-handling brain formulation. A symmetric system matrix has useful properties, e.g. only the upper triangular part needs to be stored, which could reduce the computation and solution time. The proposed hybrid method is asymmetric in the surface block (an adjoint double-layer operator) and in the volume and wire blocks since the contrast is not included in the testing functions.

- A conditioning analysis of the hybrid formulation. The proposed strategy introduces new discretized volume and wire operator matrices, with possibly different asymptotic behaviors (in high contrast or mesh refinement) than the standard surface operators. If such a case arises, the use of an appropriate preconditioner in the hybrid formulation would ensure that the system matrix remains well conditioned.

- The application of the presented techniques to other scenarios. Applications such as inverse source imaging for epilepsy planning, brain computer interfaces, and transcranial electric and magnetic stimulation all rely on the solution of a forward problem that could benefit from the proposed strategies.

- The extension of the ACA-based fast solver to H2 matrices. This would be achieved with the use of hierarchical bases, in which columns (or rows) in low level blocks are expressed as a linear combination of columns (or rows) in higher level blocks. This would remove the $\log N$ factor in the asymptotic complexity of the fast solver, thereby achieving a true linear complexity.

- The error analysis of the fast solver. Compressing the kernel function sampled on quadrature points introduces constraints on the accuracy of the integrals at the level of the basis function interactions. Therefore, we should ensure that the compression error remains controlled.

- The analysis of other optimization algorithms for inverse problems. For instance, conductivity imaging could be recast in the framework of Contrast Source Imaging (CSI) in which material inhomogeneity is also handled via a contrast function. An improved optimization could be achieved with the addition of the state equation error or suitable priors in the cost function. The inclusion of multimodal data such as combined MEG/EEG data could also positively impact the inverse procedure.

List of Symbols

Acronyms

ACA	Adaptive Cross Approximation
BCI	Brain Computer Interface
BEM	Boundary Element Method
CGS	Conjugate Gradient Square
CT	Computed Tomography
dMRI	Diffusion Magnetic Resonance Imaging
DTI	Diffusion Tensor Imaging
EEG	Electroencephalography
EIT	Electrical Impedance Tomography
FDM	Finite Difference Method
FEM	Finite Element Method
FMM	Fast Multipole Method
GMRES	Generalized Minimal Residual
MEG	Magnetoencephalography
MRI	Magnetic Resonance Imaging
SVD	Singular Value Decomposition
SWG	Schaubert-Wilton-Glisson

Physical and Mathematical Notation

$\boldsymbol{E}$	Electric field (V/m)

$\boldsymbol{H}$	Magnetic field (A/m)
$\boldsymbol{D}$	Electric flux density (C/m^2)
$\boldsymbol{B}$	Magnetic flux density (Wb/m^2)
$\boldsymbol{J}$	Electric current density (A/m^2)
$\boldsymbol{J}_p$	Primary electric current density (A/m^2)
ϕ	Electric potential (V)
σ	Conductivity (S/m)
ϵ	Electric permittivity (F/m)
μ	Magnetic permeability (H/m)
ρ	Electric charge density (C/m^3)
$\boldsymbol{q}$	Dipole moment (C.m)
$\hat{\boldsymbol{n}}$	Unit normal
χ	Conductivity contrast
G	Green's function
δ	Dirac delta function
$\|\boldsymbol{f}\|$	Euclidian norm of $\boldsymbol{f}$
$\langle a, b \rangle$	Inner product of a and b
$[f]$	Jump of f

Publications

[79] Maxime Y Monin, Lyes Rahmouni, and Francesco P Andriulli. "A Hybrid Integral Equation Approach to Solve the Anisotropic Forward Problem in Electroencephalography". In: *2018 IEEE International Symposium on Antennas and Propagation & USNC/URSI National Radio Science Meeting*. IEEE. 2018, pp. 2395–2396.

[80] Maxime Y Monin, Lyes Rahmouni, and Francesco P Andriulli. "Diffusion mri consistent wire models for efficient solutions of the anisotropic forward problem in electroencephalography". In: *2019 International Conference on Electromagnetics in Advanced Applications (ICEAA)*. IEEE. 2019, pp. 1251–1254.

[81] Maxime Y Monin et al. "A Hybrid Volume-Surface-Wire Integral Equation for the Anisotropic Forward Problem in Electroencephalography". In: *IEEE Journal of Electromagnetics, RF and Microwaves in Medicine and Biology* (2020).

Bibliography

[1] Juan-Felipe PJ Abascal et al. "Use of anisotropic modelling in electrical impedance tomography; description of method and preliminary assessment of utility in imaging brain function in the adult human head". In: *Neuroimage* 43.2 (2008), pp. 258–268.

[2] Massoud Akhtari et al. "Conductivities of three-layer live human skull". In: *Brain topography* 14.3 (2002), pp. 151–167.

[3] Brendan Z Allison, Elizabeth Winter Wolpaw, and Jonathan R Wolpaw. "Brain–computer interface systems: progress and prospects". In: *Expert review of medical devices* 4.4 (2007), pp. 463–474.

[4] Francesco P Andriulli and Giuseppe Vecchi. "A Helmholtz-stable fast solution of the electric field integral equation". In: *IEEE transactions on antennas and propagation* 60.5 (2012), pp. 2357–2366.

[5] Kassem A Awada et al. "Closed-Form Evaluation of Flux Integrals Appearing in a Finite Element Solution of the 3D Poisson Equation with Dipole Sources". In: *Electromagnetics* 20.3 (2000), pp. 167–185.

[6] Dale L Bailey et al. *Positron emission tomography*. Vol. 2. Springer, 2005.

[7] Sylvain Baillet, John C Mosher, and Richard M Leahy. "Electromagnetic brain mapping". In: *IEEE Signal processing magazine* 18.6 (2001), pp. 14–30.

[8] Adam P Baker et al. "Fast transient networks in spontaneous human brain activity". In: *Elife* 3 (2014), e01867.

[9] Tonio Ball et al. "Signal quality of simultaneously recorded invasive and non-invasive EEG". In: *Neuroimage* 46.3 (2009), pp. 708–716.

[10] David C Barber and Brian H Brown. "Applied potential tomography". In: *Journal of Physics E: Scientific Instruments* 17.9 (1984), p. 723.

[11] Gregory L Barkley and Christoph Baumgartner. "MEG and EEG in epilepsy". In: *Journal of clinical neurophysiology* 20.3 (2003), pp. 163–178.

[12] Peter J Basser et al. "In vivo fiber tractography using DT-MRI data". In: *Magnetic resonance in medicine* 44.4 (2000), pp. 625–632.

[13] Mario Bebendorf. "Approximation of boundary element matrices". In: *Numerische Mathematik* 86.4 (2000), pp. 565–589.

[14] Mario Bebendorf. *Hierarchical matrices*. Springer, 2008.

[15] Mario Bebendorf and Richard Grzhibovskis. "Accelerating Galerkin BEM for linear elasticity using adaptive cross approximation". In: *Mathematical Methods in the Applied Sciences* 29.14 (2006), pp. 1721–1747.

[16] Patrick Berg and Michael Scherg. "A fast method for forward computation of multiple-shell spherical head models". In: *Electroencephalography and clinical Neurophysiology* 90.1 (1994), pp. 58–64.

[17] E Bleszynski, M Bleszynski, and T Jaroszewicz. "AIM: Adaptive integral method for solving large-scale electromagnetic scattering and radiation problems". In: *Radio Science* 31.5 (1996), pp. 1225–1251.

[18] Marc Bonnet. *Equations intégrales et éléments de frontiere*. 1995.

[19] Achi Brandt. "Multilevel computations of integral transforms and particle interactions with oscillatory kernels". In: *Computer Physics Communications* 65.1-3 (1991), pp. 24–38.

[20] Romain Brette and Alain Destexhe. *Handbook of neural activity measurement*. Cambridge University Press, 2012.

[21] P Bruno et al. "A FDM anisotropic formulation for EEG simulation". In: *Engineering in Medicine and Biology Society, 2006. EMBS'06. 28th Annual International Conference of the IEEE*. IEEE. 2006, pp. 1121–1125.

[22] Peter Businger and Gene H Golub. "Linear least squares solutions by Householder transformations". In: *Numerische Mathematik* 7.3 (1965), pp. 269–276.

[23] György Buzsáki. *Rhythms of the Brain*. Oxford University Press, 2006.

[24] György Buzsáki, Costas A Anastassiou, and Christof Koch. "The origin of extracellular fields and currents—EEG, ECoG, LFP and spikes". In: *Nature reviews neuroscience* 13.6 (2012), pp. 407–420.

[25] Thorsten M Buzug. "Computed tomography". In: *Springer Handbook of Medical Technology*. Springer, 2011, pp. 311–342.

[26] Tony F Chan. "Deflated decomposition of solutions of nearly singular systems". In: *SIAM journal on numerical analysis* 21.4 (1984), pp. 738–754.

[27] Margaret Cheney, David Isaacson, and Jonathan C Newell. "Electrical impedance tomography". In: *SIAM review* 41.1 (1999), pp. 85–101.

[28] Weng Cho Chew, Mei Song Tong, and Bin Hu. "Integral equation methods for electromagnetic and elastic waves". In: *Synthesis Lectures on Computational Electromagnetics* 3.1 (2008), pp. 1–241.

[29] Weng Cho Chew et al. *Fast and efficient algorithms in computational electromagnetics*. Artech House, Inc., 2001.

[30] Maureen Clerc et al. "Boundary element formulation for electrical impedance tomography". In: *ESAIM: Proceedings*. Vol. 14. EDP Sciences. 2005, pp. 63–71.

[31] David Colton and Rainer Kress. *Integral equation methods in scattering theory*. SIAM, 2013.

[32] Juhani Dabek et al. "Determination of head conductivity frequency response in vivo with optimized EIT-EEG". In: *Neuroimage* 127 (2016), pp. 484–495.

[33] A. Daducci et al. "COMMIT: Convex optimization modeling for microstructure informed tractography". In: *IEEE Trans Med Imaging* 34.1 (Jan. 2015), pp. 246–257.

[34] Moritz Dannhauer et al. "Modeling of the human skull in EEG source analysis". In: *Human brain mapping* 32.9 (2011), pp. 1383–1399.

[35] Guy David and Jean-Lin Journé. "A boundedness criterion for generalized Calderón-Zygmund operators". In: *Annals of Mathematics* (1984), pp. 371–397.

[36] Marzia De Lucia et al. "Diffusion tensor MRI-based estimation of the influence of brain tissue anisotropy on the effects of transcranial magnetic stimulation". In: *Neuroimage* 36.4 (2007), pp. 1159–1170.

[37] JC De Munck. "The potential distribution in a layered anisotropic spheroidal volume conductor". In: *Journal of applied Physics* 64.2 (1988), pp. 464–470.

[38] Michael G Duffy. "Quadrature over a pyramid or cube of integrands with a singularity at a vertex". In: *SIAM journal on Numerical Analysis* 19.6 (1982), pp. 1260–1262.

[39] Gaute T Einevoll et al. "Modelling and analysis of local field potentials for studying the function of cortical circuits". In: *Nature Reviews Neuroscience* 14.11 (2013), pp. 770–785.

[40] Dennis van't Ent, Jan Casper de Munck, and Amanda L Kaas. "A fast method to derive realistic BEM models for E/MEG source reconstruction". In: *IEEE Transactions on Biomedical Engineering* 48.12 (2001), pp. 1434–1443.

[41] Shawna Farquharson et al. "White matter fiber tractography: why we need to move beyond DTI". In: *Journal of neurosurgery* 118.6 (2013), pp. 1367–1377.

[42] Mariano Fernández-Corazza et al. "Analysis of parametric estimation of head tissue conductivities using electrical impedance tomography". In: *Biomedical Signal Processing and Control* 8.6 (2013), pp. 830–837.

[43] Mariano Fernández-Corazza et al. “Skull modeling effects in conductivity estimates using parametric electrical impedance tomography”. In: *IEEE Transactions on Biomedical Engineering* 65.8 (2017), pp. 1785–1797.

[44] Thomas C Ferree, K Jeffrey Eriksen, and Don M Tucker. “Regional head tissue conductivity estimation for improved EEG analysis”. In: *IEEE Transactions on Biomedical Engineering* 47.12 (2000), pp. 1584–1592.

[45] Karl J Friston. “Modalities, modes, and models in functional neuroimaging”. In: *Science* 326.5951 (2009), pp. 399–403.

[46] Eleftherios Garyfallidis et al. “Dipy, a library for the analysis of diffusion MRI data”. In: *Frontiers in neuroinformatics* 8 (2014), p. 8.

[47] Eleftherios Garyfallidis et al. “Quickbundles, a method for tractography simplification”. In: *Frontiers in neuroscience* 6 (2012), p. 175.

[48] Matthew F Glasser et al. “The minimal preprocessing pipelines for the Human Connectome Project”. In: *Neuroimage* 80 (2013), pp. 105–124.

[49] Roberto D Graglia. “On the numerical integration of the linear shape functions times the 3-D Green’s function or its gradient on a plane triangle”. In: *IEEE Transactions on Antennas and Propagation* 41.10 (1993), pp. 1448–1455.

[50] Alexandre Gramfort et al. “OpenMEEG: opensource software for quasistatic bioelectromagnetics”. In: *Biomedical engineering online* 9.1 (2010), p. 45.

[51] Roberta Grech et al. “Review on solving the inverse problem in EEG source analysis”. In: *Journal of neuroengineering and rehabilitation* 5.1 (2008), p. 25.

[52] Daniel Güllmar, Jens Haueisen, and Jürgen R Reichenbach. “Influence of anisotropic electrical conductivity in white matter tissue on the EEG/MEG forward and inverse solution. A high-resolution whole head simulation study”. In: *Neuroimage* 51.1 (2010), pp. 145–163.

[53] Hans Hallez et al. “Review on solving the forward problem in EEG source analysis”. In: *Journal of neuroengineering and rehabilitation* 4.1 (2007), p. 46.

[54] Matti S Hämäläinen and Jukka Sarvas. “Realistic conductivity geometry model of the human head for interpretation of neuromagnetic data”. In: *IEEE transactions on biomedical engineering* 36.2 (1989), pp. 165–171.

[55] Matti S Hämäläinen et al. “Magnetoencephalography—theory, instrumentation, and applications to noninvasive studies of the working human brain”. In: *Reviews of modern Physics* 65.2 (1993), p. 413.

[56] Steven A Hillyard and Marta Kutas. “Electrophysiology of cognitive processing”. In: *Annual review of psychology* 34.1 (1983), pp. 33–61.

[57] David S Holder. *Electrical impedance tomography: methods, history and applications*. CRC Press, 2004.

[58] Roger A Horn and Charles R Johnson. *Matrix analysis*. Cambridge university press, 2012.

[59] Aung Thu Htet et al. "Comparative performance of the finite element method and the boundary element fast multipole method for problems mimicking transcranial magnetic stimulation (TMS)". In: *Journal of neural engineering* (2019).

[60] Yu Huang et al. "Measurements and models of electric fields in the in vivo human brain during transcranial electric stimulation". In: *Elife* 6 (2017), e18834.

[61] Scott A Huettel, Allen W Song, Gregory McCarthy, et al. *Functional magnetic resonance imaging*. Vol. 1. Sinauer Associates Sunderland, MA, 2004.

[62] Seppo Järvenpää, Matti Taskinen, and Pasi Ylä-Oijala. "Singularity extraction technique for integral equation methods with higher order basis functions on plane triangles and tetrahedra". In: *International journal for numerical methods in engineering* 58.8 (2003), pp. 1149–1165.

[63] Prasanna Jayakar et al. "Diagnostic utility of invasive EEG for epilepsy surgery: indications, modalities, and techniques". In: *Epilepsia* 57.11 (2016), pp. 1735–1747.

[64] Jian-Ming Jin. *Theory and computation of electromagnetic fields*. John Wiley & Sons, 2011.

[65] Robert C Knowlton. "The role of FDG-PET, ictal SPECT, and MEG in the epilepsy surgery evaluation". In: *Epilepsy & Behavior* 8.1 (2006), pp. 91–101.

[66] Jan Kybic et al. "A common formalism for the integral formulations of the forward EEG problem". In: *IEEE transactions on medical imaging* 24.1 (2005), pp. 12–28.

[67] Jan Kybic et al. "Fast multipole acceleration of the MEG/EEG boundary element method". In: *Physics in Medicine & Biology* 50.19 (2005), p. 4695.

[68] Helmut Laufs et al. "Electroencephalographic signatures of attentional and cognitive default modes in spontaneous brain activity fluctuations at rest". In: *Proceedings of the national academy of sciences* 100.19 (2003), pp. 11053–11058.

[69] Denis Le Bihan and Heidi Johansen-Berg. "Diffusion MRI at 25: exploring brain tissue structure and function". In: *Neuroimage* 61.2 (2012), pp. 324–341.

[70] Seok Lew et al. "Accuracy and run-time comparison for different potential approaches and iterative solvers in finite element method based EEG source analysis". In: *Applied Numerical Mathematics* 59.8 (2009), pp. 1970–1988.

[71] Zhi-Pei Liang and Paul C Lauterbur. *Principles of magnetic resonance imaging: a signal processing perspective*. SPIE Optical Engineering Press, 2000.

[72] Yijun Liu. *Fast multipole boundary element method: theory and applications in engineering*. Cambridge university press, 2009.

[73] A.M. Lozano and M. Hallett. *Brain Stimulation*. Handbook of Clinical Neurology. Elsevier Science, 2013. ISBN: 9780444534989.

[74] K. H. Maier-Hein et al. "The challenge of mapping the human connectome based on diffusion tractography". In: *Nat Commun* 8.1 (Nov. 2017), p. 1349.

[75] Sergey N Makarov, Alvaro Pascual-Leone, and Aapo Nummenmaa. "Modeling fiber-like conductivity structures via the boundary element method using thin-wire approximation. I Construction of basis functions". In: *2016 38th Annual International Conference of the IEEE Engineering in Medicine and Biology Society (EMBC)*. IEEE. 2016, pp. 6473–6476.

[76] Hannah McCann, Giampaolo Pisano, and Leandro Beltrachini. "Variation in reported human head tissue electrical conductivity values". In: *Brain topography* 32.5 (2019), pp. 825–858.

[77] Christoph M Michel et al. "EEG source imaging". In: *Clinical neurophysiology* 115.10 (2004), pp. 2195–2222.

[78] Eric Michielssen and Amir Boag. "A multilevel matrix decomposition algorithm for analyzing scattering from large structures". In: *IEEE Transactions on Antennas and Propagation* 44.8 (1996), pp. 1086–1093.

[79] Maxime Y Monin, Lyes Rahmouni, and Francesco P Andriulli. "A Hybrid Integral Equation Approach to Solve the Anisotropic Forward Problem in Electroencephalography". In: *2018 IEEE International Symposium on Antennas and Propagation & USNC/URSI National Radio Science Meeting*. IEEE. 2018, pp. 2395–2396.

[80] Maxime Y Monin, Lyes Rahmouni, and Francesco P Andriulli. "Diffusion mri consistent wire models for efficient solutions of the anisotropic forward problem in electroencephalography". In: *2019 International Conference on Electromagnetics in Advanced Applications (ICEAA)*. IEEE. 2019, pp. 1251–1254.

[81] Maxime Y Monin et al. "A Hybrid Volume-Surface-Wire Integral Equation for the Anisotropic Forward Problem in Electroencephalography". In: *IEEE Journal of Electromagnetics, RF and Microwaves in Medicine and Biology* (2020).

[82] Victoria Montes-Restrepo et al. "Influence of skull modeling approaches on EEG source localization". In: *Brain topography* 27.1 (2014), pp. 95–111.

[83] John C Mosher, Richard M Leahy, and Paul S Lewis. "EEG and MEG: forward solutions for inverse methods". In: *IEEE Transactions on Biomedical Engineering* 46.3 (1999), pp. 245–259.

[84] Jean-Claude Nédélec. *Acoustic and electromagnetic equations: integral representations for harmonic problems*. Springer Science & Business Media, 2001.

[85] Paul W. Nicholson. "Specific impedance of cerebral white matter". In: *Experimental Neurology* 13.4 (1965), pp. 386–401. ISSN: 0014-4886.

[86] Ernst Niedermeyer and FH Lopes da Silva. *Electroencephalography: basic principles, clinical applications, and related fields*. Lippincott Williams & Wilkins, 2005.

[87] Aapo Nummenmaa et al. "Targeting of white matter tracts with transcranial magnetic stimulation". In: *Brain stimulation* 7.1 (2014), pp. 80–84.

[88] Paul L Nunez, Ramesh Srinivasan, et al. *Electric fields of the brain: the neurophysics of EEG*. Oxford University Press, USA, 2006.

[89] Emmanuel Olivi, Théodore Papadopoulo, and Maureen Clerc. "Handling white-matter anisotropy in BEM for the EEG forward problem". In: *Proceedings of the 8th IEEE International Symposium on Biomedical Imaging: From Nano to Macro, ISBI 2011*. IEEE. 2011, pp. 799–802.

[90] Robert Oostenveld et al. "FieldTrip: open source software for advanced analysis of MEG, EEG, and invasive electrophysiological data". In: *Computational intelligence and neuroscience* 2011 (2011), p. 1.

[91] H Oouchi et al. "Diffusion anisotropy measurement of brain white matter is affected by voxel size: underestimation occurs in areas with crossing fibers". In: *American Journal of Neuroradiology* 28.6 (2007), pp. 1102–1106.

[92] Alexander Opitz et al. "How the brain tissue shapes the electric field induced by transcranial magnetic stimulation". In: *Neuroimage* 58.3 (2011), pp. 849–859.

[93] Jörg Ostrowski et al. "Fast BEM-solution of Laplace problems with H-matrices and ACA". In: *IEEE Transactions on Magnetics* 42.4 (2006), pp. 627–630.

[94] Mahboubeh Parastarfeizabadi and Abbas Z Kouzani. "Advances in closed-loop deep brain stimulation devices". In: *Journal of neuroengineering and rehabilitation* 14.1 (2017), p. 79.

[95] Roberto Domingo Pascual-Marqui. "Review of methods for solving the EEG inverse problem". In: *International journal of bioelectromagnetism* 1.1 (1999), pp. 75–86.

[96] Gert Pfurtscheller and FH Lopes Da Silva. "Event-related EEG/MEG synchronization and desynchronization: basic principles". In: *Clinical neurophysiology* 110.11 (1999), pp. 1842–1857.

[97] Joel R Phillips and Jacob K White. "A precorrected-FFT method for electrostatic analysis of complicated 3-D structures". In: *IEEE Transactions on Computer-Aided Design of Integrated Circuits and Systems* 16.10 (1997), pp. 1059–1072.

[98] Axelle Pillain. "Line, Surface, and Volume Integral Equations for the Electromagnetic Modelling of the Electroencephalography Forward Problem". PhD thesis. Ecole Nationale Supérieure des Télécommunications de Bretagne-ENSTB, 2016.

[99] Walter S Pritchard. "The brain in fractal time: 1/f-like power spectrum scaling of the human electroencephalogram". In: *International Journal of Neuroscience* 66.1-2 (1992), pp. 119–129.

[100] Lyes Rahmouni, Rajendra Mitharwal, and Francesco P Andriulli. "Two volume integral equations for the inhomogeneous and anisotropic forward problem in electroencephalography". In: *Journal of Computational Physics* 348 (2017), pp. 732–743.

[101] Lyes Rahmouni et al. "Conforming discretizations of boundary element solutions to the electroencephalography forward problem". In: *Comptes Rendus Physique* 19.1-2 (2018), pp. 7–25.

[102] Lyes Rahmouni et al. "On the Boundary Element Modeling of Brain Fibers in the EEG Forward Problem via a New Family of Wire Integral Equations". In: *arXiv preprint arXiv:1903.08414* (2019).

[103] Michael Rullmann et al. "EEG source analysis of epileptiform activity using a 1 mm anisotropic hexahedra finite element head model". In: *NeuroImage* 44.2 (2009), pp. 399–410.

[104] Youcef Saad and Martin H Schultz. "GMRES: A generalized minimal residual algorithm for solving nonsymmetric linear systems". In: *SIAM Journal on scientific and statistical computing* 7.3 (1986), pp. 856–869.

[105] Sepideh Sadaghiani et al. "The relation of ongoing brain activity, evoked neural responses, and cognition". In: *Frontiers in systems neuroscience* 4 (2010), p. 20.

[106] Jukka Sarvas. "Basic mathematical and electromagnetic concepts of the biomagnetic inverse problem". In: *Physics in Medicine & Biology* 32.1 (1987), p. 11.

[107] D Schaubert, D Wilton, and A Glisson. "A tetrahedral modeling method for electromagnetic scattering by arbitrarily shaped inhomogeneous dielectric bodies". In: *IEEE Transactions on Antennas and Propagation* 32.1 (1984), pp. 77–85.

[108] Salman Shahid, Peng Wen, and Tony Ahfock. "Numerical investigation of white matter anisotropic conductivity in defining current distribution under tDCS". In: *Computer methods and programs in biomedicine* 109.1 (2013), pp. 48–64.

[109] Simon Shorvon. *Handbook of epilepsy treatment*. John Wiley & Sons, 2010.

[110] Heinz W Siesler et al. *Near-infrared spectroscopy: principles, instruments, applications*. John Wiley & Sons, 2008.

[111] R. E. Smith et al. "SIFT2: Enabling dense quantitative assessment of brain white matter connectivity using streamlines tractography". In: *Neuroimage* 119 (Oct. 2015), pp. 338–351.

[112] R. E. Smith et al. "The effects of SIFT on the reproducibility and biological accuracy of the structural connectome". In: *Neuroimage* 104 (Jan. 2015), pp. 253–265.

[113] Jiming Song, Cai-Cheng Lu, and Weng Cho Chew. "Multilevel fast multipole algorithm for electromagnetic scattering by large complex objects". In: *IEEE Transactions on Antennas and Propagation* 45.10 (1997), pp. 1488–1493.

[114] Peter Sonneveld. "CGS, a fast Lanczos-type solver for nonsymmetric linear systems". In: *SIAM journal on scientific and statistical computing* 10.1 (1989), pp. 36–52.

[115] Olaf Steinbach. *Numerical approximation methods for elliptic boundary value problems: finite and boundary elements*. Springer Science & Business Media, 2007.

[116] Axel Thielscher, Andre Antunes, and Guilherme B Saturnino. "Field modeling for transcranial magnetic stimulation: a useful tool to understand the physiological effects of TMS?" In: *2015 37th annual international conference of the IEEE engineering in medicine and biology society (EMBC)*. IEEE. 2015, pp. 222–225.

[117] J-Donald Tournier, Fernando Calamante, and Alan Connelly. "MRtrix: diffusion tractography in crossing fiber regions". In: *International Journal of Imaging Systems and Technology* 22.1 (2012), pp. 53–66.

[118] David S Tuch et al. "Conductivity mapping of biological tissue using diffusion MRI". In: *Annals of the New York Academy of Sciences* 888.1 (1999), pp. 314–316.

[119] Sergei I Turovets et al. "Conductivity analysis for high-resolution EEG". In: *2008 International Conference on BioMedical Engineering and Informatics*. Vol. 2. IEEE. 2008, pp. 386–393.

[120] Anja G Van der Kolk et al. "Clinical applications of 7 T MRI in the brain". In: *European journal of radiology* 82.5 (2013), pp. 708–718.

[121] David C Van Essen et al. "The WU-Minn human connectome project: an overview". In: *Neuroimage* 80 (2013), pp. 62–79.

[122] Francesca Vipiana and Donald R Wilton. "Numerical evaluation via singularity cancellation schemes of near-singular integrals involving the gradient of Helmholtz-type potentials". In: *IEEE transactions on antennas and propagation* 61.3 (2012), pp. 1255–1265.

[123] Curtis R Vogel. *Computational methods for inverse problems*. SIAM, 2002.

[124] Johannes Vorwerk et al. "A guideline for head volume conductor modeling in EEG and MEG". In: *NeuroImage* 100 (2014), pp. 590–607.

[125] Brian A Wandell. "Clarifying human white matter". In: *Annual review of neuroscience* 39 (2016), pp. 103–128.

[126] Miles N Wernick and John N Aarsvold. *Emission tomography: the fundamentals of PET and SPECT*. Elsevier, 2004.

[127] Donald R Wilton and Nathan J Champagne. "Evaluation and integration of the thin wire kernel". In: *IEEE transactions on antennas and propagation* 54.4 (2006), pp. 1200–1206.

[128] DRSM Wilton et al. "Potential integrals for uniform and linear source distributions on polygonal and polyhedral domains". In: *IEEE Transactions on Antennas and Propagation* 32.3 (1984), pp. 276–281.

[129] Jonathan R Wolpaw et al. "Brain-computer interface technology: a review of the first international meeting". In: *IEEE transactions on rehabilitation engineering* 8.2 (2000), pp. 164–173.

[130] Carsten Hermann Wolters. "Influence of tissue conductivity inhomogeneity and anisotropy on EEG/MEG based source localization in the human brain". PhD thesis. Max Planck Institute of Cognitive Neuroscience Leipzig, 2003.

[131] Carsten Hermann Wolters et al. "Influence of tissue conductivity anisotropy on EEG/MEG field and return current computation in a realistic head model: a simulation and visualization study using high-resolution finite element modeling". In: *NeuroImage* 30.3 (2006), pp. 813–826.

[132] Kei Yamada et al. "MR tractography: a review of its clinical applications." In: *Magnetic resonance in medical sciences : MRMS : an official journal of Japan Society of Magnetic Resonance in Medicine* 8 4 (2009), pp. 165–74.

[133] Dezhong Yao. "Electric potential produced by a dipole in a homogeneous conducting sphere". In: *IEEE transactions on biomedical engineering* 47.7 (2000), pp. 964–966.

[134] Kechen Zhang and Terrence J Sejnowski. "A universal scaling law between gray matter and white matter of cerebral cortex". In: *Proceedings of the National Academy of Sciences* 97.10 (2000), pp. 5621–5626.

[135] Zhi Zhang. "A fast method to compute surface potentials generated by dipoles within multilayer anisotropic spheres". In: *Physics in medicine & biology* 40.3 (1995), p. 335.